POLITECNICO DI MILANO

Facoltà di Ingegneria Industriale
Corso di Laurea Magistrale in Ingegneria Meccanica

DEVELOPMENT AND VALIDATION OF A CFD MODEL FOR COMBUSTION SIMULATIONS IN DIRECT INJECTION DIESEL ENGINES BASED ON DETAILED CHEMISTRY AND THE UNSTEADY DIFFUSION FLAMELET ASSUMPTION

Relatore: Ing. Tommaso LUCCHINI

Tesi di laurea di
Paolo COLOMBI matr. 765412

Anno Accademico 2011-2012

Alla mia famiglia

Contents

List of Figures

List of Tables

List of abbreviations

ALMR	Adaptive Local Mesh Refinement
ASI	After Start of Injection
CFD	Computational Fluid Dynamics
CTC	Characteristic Time Combustion model
DAC	Dynamic Adaptive Chemistry
DI	Direct Injection
DIC	Diagonal Incomplete Cholesky
DILU	Diagonal Incomplete LU
DNS	Direct Numerical Simulation
EGR	Exhaust-gas recirculation
EPFM	Eulerian Particle Flamelet Model
FWHM	Full Width Half Maximum
IEPFM	Interactive Eulerian Particle Flamelet Model
ISAT	*in situ* Adaptive Tabulation
LII	Laser Induced Incandescence
ODE	Ordinary Differential Equation
PAH	Polycyclic Aromatic Hydrocarbon
PAHs	Polycyclic Aromatic Hydrocarbons
PBiCG	Pre-conditioned bi-Conjugate Gradient

PCCI	Premixed Charge Compression Ignition
PCG	Pre-conditioned Conjugate Gradient
PDF	Probability Density Function
PISO	Pressure Implicit with Splitting Operators
PLIF	Planar Laser Induced Fluorescence
RANS	Reynolds Averaged Navier Stokes
RIF	Representative Interactive Flamelet model
SDR	Scalar Dissipation Rate
SIMPLE	Semi-Implicit Method for Pressure-Linked Equations
SNL	Sandia National Laboratories
SOI	Start Of Injection
TDAC	Tabulation of Dynamic Adaptive Chemistry
TVD	Total Variation Diminishing

Abstract

In this work a CFD solver for combustion simulation in direct injection Diesel engines has been implemented in Lib-ICE, an OpenFOAM library for internal combustion engine simulations developed by the ICE group of Politecnico di Milano. The solver is based on the flamelet assumption, with a set of unsteady diffusion flames representing the Diesel combustion process according to the Representative Interactive Flamelet approach. Also different variants of this model were tested, namely the Eulerian Particle Flamelet model and the Interactive Eulerian Particle Flamelet model. Validation was carried out with data from the Sandia combustion vessel, by comparing computed and experimental data of pressure rise, heat release, lift-off length, flame structure and acetylene and formaldehyde distributions, in order to investigate the capability of the models to predict soot precursors. The simulations carried out using a single flamelet show that the RIF model cannot reproduce lift-off, predicting a flame which is attached to the injector tip. The most encouraging results have been obtained using the Eulerian Particle Flamelet model with flamelets created according to the injection time. These simulations are able to reproduce the flame propagation and a flame structure in rather good agreement with the real one. For this model the influence of ambient conditions on the results has been investigated in terms of initial vessel temperature, density and oxygen concentration.

Key-words: CFD, flamelet, RIF, combustion, Diesel.

Presentazione

Nel presente lavoro di tesi è stato implementato un solutore adatto alla simulazione del processo di combustione in motori Diesel a iniezione diretta. L'applicazione è stata integrata nella libreria OpenFOAM per la simulazione di motori a combustione interna Lib-ICE, sviluppata dal gruppo ICE del Politecnico di Milano. Il modello di combustione oggetto di studio si basa sulla cosiddetta *flamelet assumption*, in cui il processo di combustione Diesel è rappresentato tramite l'ausilio di una o più fiamme diffusive instazionarie. Oltre all'appena citato modello, denominato *Representative Interactive Flamelet model*, sono state incluse nel solutore anche delle ulteriori versioni alternative nate come evoluzioni di quest'ultimo, ovvero lo *Eulerian Particle Flamelet model* e lo *Interactive Eulerian Particle Flamelet model*. La validazione dell'applicazione è stata effettuata paragonando i valori di pressione, rilascio di energia, struttura di fiamma e precursori del particolato calcolati tramite le simulazioni, con quelli provenienti dalla camera di combustione a volume costante dei Sandia National Laboratories. Mentre il modello RIF non è stato in grado di riprodurre la struttura di fiamma tipica della combustione Diesel, che vede la zona ad alta temperatura ad una ben determinata distanza dall'iniettore, lo *Eulerian Particle Flamelet model* ha fornito i risultati più promettenti nel caso di assegnazione a ciascuna fiamma diffusiva della stessa quantità di massa iniettata, mostrando una struttura di fiamma in discreto accordo con i risultati sperimentali. Per questo modello in particolare, viste le sue interessanti potenzialità, è stata studiata anche la previsione della risposta alle variazioni di condizioni ambiente, in termini di pressione, temperatura e concentrazione di ossigeno della camera di combustione all'inizio della simulazione.

Introduction

Nowadays road transport plays a fundamental role in everyday life, not only for what concerns transportation of goods but also for transportation of people. Unfortunately the steep increasing of vehicles circulating everyday on the road network, which has taken place during the last decades, has accelerated the production of greenhouse gases and pollutants like soot, NO_x, unburned hydrocarbons and carbon monoxide.

The automotive industry can effectively contribute to protect the environment, by improving the efficiency of the combustion process and reducing pollutant formation. Diesel engines for passenger cars and trucks represent a possible solution for a better energy consumption thanks to their high efficiency, excellent durability and reliability, high driving comfort and performance. Since the most serious drawback of Diesel engines is the production of noxious substances like soot and NO_x, an advanced investigation of the physical and chemical processes occurring during the combustion cycle is fundamental.

Within this context, computational fluid dynamics modelling can significantly reduce research and development time, providing informations not easily available through experiments and essential to understand the chemical and physical mechanisms responsible for energy release and pollutant formation.

Different approaches are available to simulate combustion in Diesel engines and, among them, the most promising are based on the *flamelet* concept, where the unsteady flame is assumed to be locally one-dimensional. In particular the Representative Interactive Flamelet model, where the chemical time scales and the fluid dynamics time scales are decoupled, allows the application of detailed chemistry, which is able to describe all the physical processes taking place during the combustion cycle, namely autoignition, partially premixed burning, diffusive combustion and pollutant formation. This model has been used by many authors to simulate several combustion environments, providing encouraging results [2, 3, 13, 32, 38].

In this work the RIF model and its evolutions (the Eulerian Particle

Flamelet model and the Interactive Eulerian Particle Flamelet model) have been implemented in Lib-ICE, the library for internal combustion engine simulations developed by the ICE group of Politecnico di Milano and based on the open-source CFD code OpenFOAM.

The solver was validated with combustion simulations in the Sandia constant volume vessel. Computed and experimental values of ignition delay and flame lift-off were compared for a wide range of operating conditions, including variations of ambient temperature, density and oxygen concentration. Furthermore, the capability of the model to predict the flame structure in terms of formaldehyde and soot precursors was also evaluated.

This work is organised in six chapters. In chapter (1), a conceptual model for direct injection Diesel combustion is presented, then some alternative approaches for modelling Diesel combustion are briefly described and finally the conservation equations governing the turbulent flow field are explained. In chapter (2), the Representative Interactive Flamelet model is presented, also focusing on the flamelet concept. In chapter (3), some improvements to the RIF model are discussed, namely a model for the source terms of variance of the mixture fraction due to spray evaporation, the RIF model with multiple flamelets and the models accounting for flamelet interaction. In chapter (4), the CFD solver developed in this study is deeply described. Chapter (5) presents the experimental test realized in the Sandia National Laboratories used for validation and the CFD simulations set-up. Finally, in chapter (6) the results achieved from the simulations are discussed, emphasizing the features of each model studied in this work.

Chapter 1

Modelling Diesel engine combustion

Diesel engines for passenger cars have become more and more popular over the last few years due to the low fuel consumption, excellent durability and reliability, high driving comfort and performance.

In 1997, through the Kyoto Protocol, the industrial nations officially started the battle against climate change, imposing themselves to reduce their emissions of greenhouse gases mainly through severe legislative emission regulations. Because of a consistent part of CO_2 emissions and other greenhouse gases derives from road transport, the automotive industry must spend a lot of its resources in order to reduce pollutant formation, without loosing efficiency of the combustion process and even gaining improved performances.

Since efficient energy consumption is the key to reduce the impact of pollution on the environment, an advanced investigation of the physical and chemical processes which occur during the combustion cycle, namely compression, injection, ignition, combustion and pollutant formation, is compulsory.

Nowadays experiments play a fundamental role in developing new engine technologies but, since optical access to reciprocating engines is very limited, they take a lot of effort and they are expensive. Besides this fact, there are several other drawbacks of experimental studies: for example studying influence of little geometry variations over combustion requires a lot of time and there are several significant processes happening in time and length scales or in places not available through experimental techniques.

Nowadays computational fluid dynamics[1] modelling has gained a lot of

[1]Hereafter abbreviated as 'CFD'.

importance in combustion science since it can significantly reduce research and development time, providing fundamental informations about the processes studied, often not available from the experiments or at least more detailed and repeatable. However, CFD simulations must be reliable over a wide range of engine operating conditions, in order to be employed as effective design tool for internal combustion engines.

In CFD simulations lots of models are used, since turbulent combustion involves several orders of magnitude of length and time scales, making direct numerical simulations of this phenomenon impossible with the computational resources now available.

1.1 Phenomenological description of direct injection Diesel combustion

Diesel combustion consists of an ensemble of complex and turbulent processes difficult to investigate before the recent development of advanced laser-based diagnostics. In fact earlier direct measurements available on a reacting Diesel fuel jet were high-speed backlight, Schlieren, natural-flame-emission cinematography and sampling probe data. These techniques have some drawbacks when applied to such kind of combustion, namely having limited spatial resolution, being not species specific and not quantitative in the case of high-speed cinematography data or being perturbing, with poor temporal resolution and giving informations about one point per measurement, in the case of sampling probes data. The limited informations available allowed only to attempt to study Diesel combustion and led to a description of the phenomenon similar to the steady spray combustion in furnaces and gas turbines [9]. Only the recent development of advanced laser-based diagnostics has made detailed, *in situ*, species specific measurements available with high spatial and temporal resolutions. These techniques have been successfully applied on several optically accessible engines and combustion vessels, providing semi-quantitative and even fully quantitative data related to Diesel combustion.

Before starting to describe the computational techniques useful to model Diesel Engine combustion, a conceptual model of direct injection Diesel combustion is presented.

This model was proposed by Dec [9] in 1997 and was derived from laser-sheet imaging. An optical-access Diesel engine was equipped with several Nd:YAG lasers, used for Laser Induced Incandescence (LII) and elastic scatter imaging, and two CCD video cameras, used to acquire imaging data.

This phenomenological description proposes a new vision of how a reacting Diesel fuel jet evolves from the start of fuel injection up through the first part of the mixing-controlled burn.

The combustion process is described through a series of schematics given with the crank angle degree after the start of injection (ASI) at which they occur[2] and depicted in figure (1.1). In figure (1.2) the apparent heat release

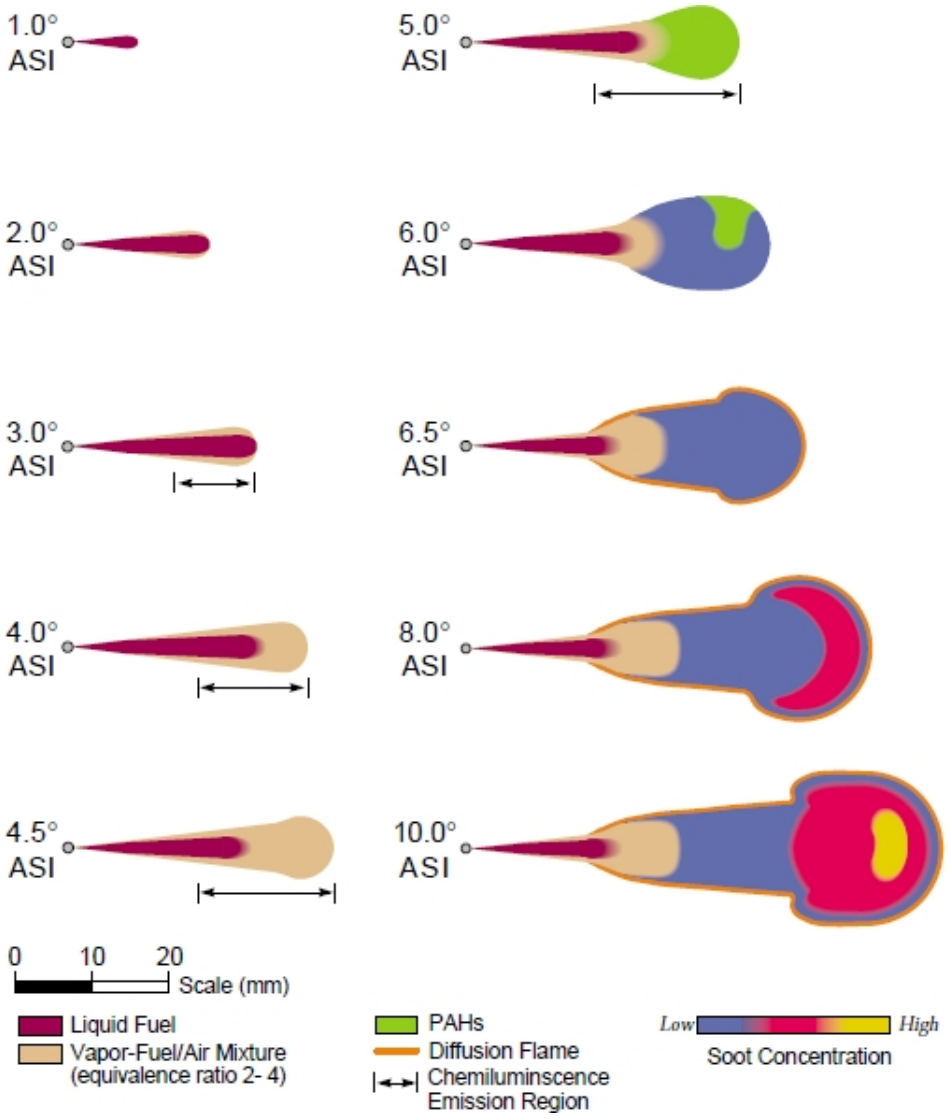

Figure 1.1: evolution of the DI Diesel combustion from the SOI to the first part of the mixing controlled burn reproduced from [9].

[2]A degree ASI is equal to 139 μs.

rate, the cylinder pressure and the injector needle lift are reproduced from [9] for the case of study.

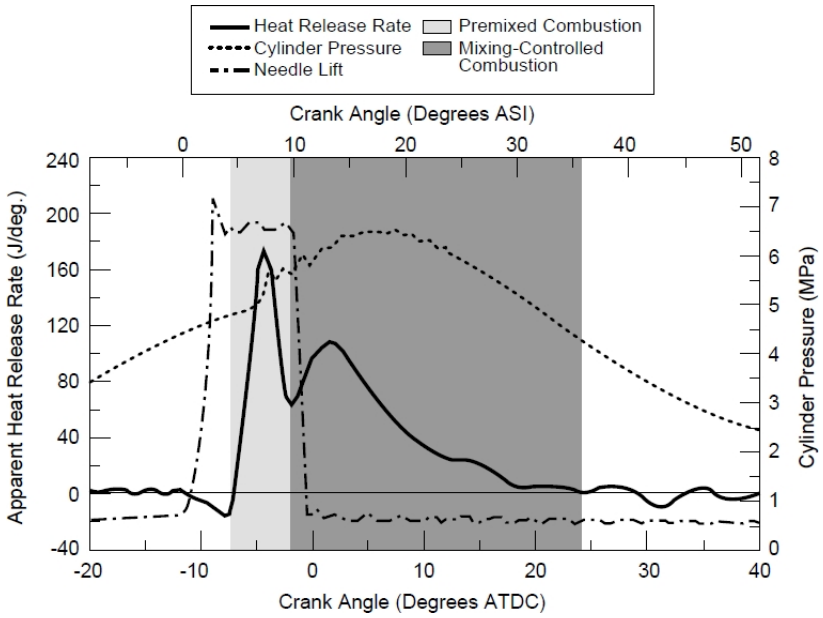

Figure 1.2: apparent heat release rate, cylinder pressure and injector needle lift reproduced from [9].

As soon as it gets into the combustion chamber, the spray is completely liquid, but, after few degrees of crank angle, a vapour-fuel region begins to develop along the sides of the jet. The width of this vapour region increases faster than the liquid one and soon the hot air entrained by the jet causes the complete vaporization of the liquid fuel, which can no longer penetrate.

The gas phase continues to penetrate across the chamber, developing a typical head vortex which contains a rich fuel-air mixture with equivalence ratio ranging from 2 to 4.

Autoignition starts from the vapour along the sides of the jet and then propagates to its leading portion. As soon as fuel decreases and large polycyclic aromatic hydrocarbons (PAHs) appear, the apparent heat release rate suddenly rises and premixed burn takes place volumetrically in the fuel-rich region of the jet.

This fuel-rich premixed burn causes the formation of small soot particles and products containing a significant quantity of unconsumed fuel, which generate a thin diffusion flame with the surrounding air at the jet periphery. This diffusion flame extends back towards the injector and large soot particles appear.

As premixed burn proceeds, soot concentration increases and the larger soot particles produced by the diffusive flame propagate inward, probably pushed by turbulent mixing.

The passage from premixed burn to mixing-controlled burn happens gradually with the consuming of the last premixed air, in fact this combustion transition shows only moderate changes in the jet appearence.

In the head vortex soot concentration increases and the soot particles become the largest of the jet, even more than the ones produced by the diffusion flame. In the central part of the jet the soot particles remain small.

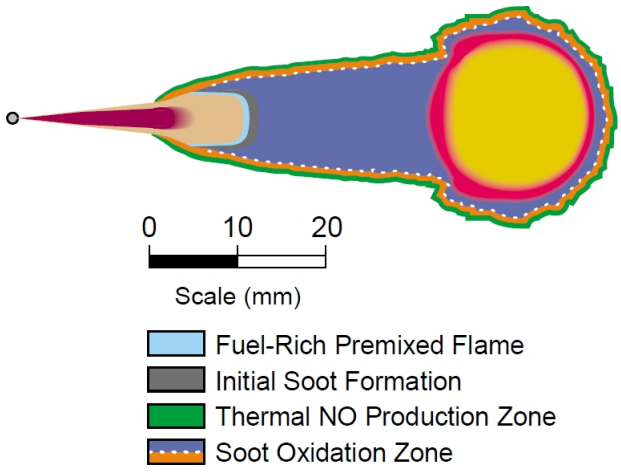

Figure 1.3: conceptual model for mixing-controlled combustion reproduced from [9].

In figure (1.3) a conceptual model of DI Diesel combustion during the mixing-controlled burn is proposed.

Going from the injector down the jet, just downstream of where all the fuel is vaporized, a standing fuel-rich premixed flame appears. This reaction zone is supported by a nearly uniform, fuel-rich mixture with an equivalence ratio of 3 to 5, which generates very small soot particles similar to those produced by the initial premixed burn.

The soot particles grow going down the jet and then they accumulate in the recirculating head vortex where they become very large. Some of them reach the periphery of the jet where they are oxidized by the OH radicals of the diffusion flame.

According to this model, the diffusion-flame combustion occurs between the products of a fuel-rich premixed combustion and the air surrounding the jet, both in the premixed phase and in the mixing-controlled phase.

Further informations of how these considerations have been derived and further explanations of the model itself can be found in [9].

1.2 Different approaches for modelling Diesel engine combustion

According to [45], there are three main approaches now available for modelling Diesel engine combustion: the Characteristic Time-Scale Combustion CFD (CTC), Well-Mixed model with detailed chemistry and the Representative Interactive Flamelet model (RIF).

Since the RIF model will be described in the following chapters, further informations about the CTC model and the direct integration model will be provided.

1.2.1 Characteristic Time-Scale Combustion model

The CTC model consists of two parts: the first one is based on the Shell model and describes low-temperature fuel oxidation and ignition, while the second one occurs at higher temperatures and calculates the species conversion rates using the equilibrium concentration of each species and a characteristic time scale.

The Shell model [12], used only to predict ignition, is based on a simplified reaction mechanism consisting of five generic species and eight generic reactions which aim to describe initiation, propagation, branching and termination steps of the process.

These five generic species include fuel, oxygen, radicals, intermediate species and branching agents. The hydrocarbon auto-ignition process is controlled by the degenerative branching phenomenon, which is described through a chain propagation cycle, together with an initiation and two termination reactions.

After ignition the CTC model [22] calculates the equilibrium concentration of each species and the corresponding laminar and turbulent characteristic times to determine species conversion rates.

The time variation of the species m can be computed as

$$\frac{dY_m}{dt} = -\frac{Y_m - Y_m^*}{\tau_c} \tag{1.1}$$

where Y_m^* is the local instantaneous equilibrium concentration and τ_c is the characteristic time.

The characteristic time τ_c is seen as the sum of a kinetic laminar time scale τ_l and a turbulent mixing time scale τ_t, weighted by a coefficient f which describes the influence of turbulence mixing on the combustion. This coefficient can be considered as a progress variable since it rises from 0 to 1 as the combustion takes place: in fact it is computed as the ratio between the instantaneous combustion products and the combustion products present when the process is concluded.

The laminar time scale is modelled involving the Arrhenius equation and considering a one-step combustion reaction between O_2 and fuel:

$$\tau_l = A^{-1}[C_n H_{2n+2}]^{0.75} \exp\left(\frac{E}{R_u T}\right) \tag{1.2}$$

where A is equal to 5.0×10^{-5}, E is the activation energy, R_u is the universal gas constant and T is the local gas temperature.

The turbulent mixing time scale is related to the integral turbulence time scale, so it can be calculated as

$$\tau_t = C_{m_2} \frac{k}{\varepsilon} \tag{1.3}$$

where C_{m_2} is a constant which must be tuned, k is the turbulent kinetic energy and ε is its dissipation rate.

As can be read above, the CTC model is very simple. This fact ensures low computational costs and acceptable accuracy for conventional Diesel combustion conditions, which make this model so popular.

This model has been compared with the RIF approach and the direct integration approach in [45], by simulating a heavy-duty direct injection Diesel engine.

Despite its low computational costs, the experimental observations lead to conclude that the CTC model under-predicts the ignition delay, over-predicts the rate of heat release and is very sensitive to the choice of model constants. For this reason, the model can be successful in a relatively narrow range of operating conditions and involving simple rate of injection profiles.

1.2.2 Well-mixed model with direct integration of chemistry

In this model the reactive mixture in each computational cell is treated as a closed system in which the rate of change of mass fraction of the single species k is calculated as

$$\frac{dY_k}{dt} = \frac{\dot{\omega}_k W_k}{\rho} \tag{1.4}$$

where Y_k is the mass fraction of the species k, ρ is the mixture density, $\dot{\omega}_k$ is the volumetric production rate of the species k and W_k is its molecular weight. Detailed chemistry is described through a skeletal reaction mechanism, which is solved for each computational cell starting from the current species and thermodynamic conditions.

The model needs an energy equation, which can be written, assuming constant volume conditions and an ideal gas mixture, as

$$c_v \frac{dT}{dt} + \frac{1}{\rho} \sum_{k=1}^{K} e_k \dot{\omega}_k W_k = 0 \tag{1.5}$$

where c_v is the mean specific heat of the mixture, T is the cell temperature and e_k is the internal energy of the species k, while the species mass fractions follow this balance equation:

$$\frac{\partial \rho Y_k}{\partial t} + \frac{\partial \left(\rho u_i Y_k + F_{k,i} \right)}{\partial x_i} = 0 \tag{1.6}$$

The CFD time step is used as integration time during the chemistry solution, where a DVODE solver (double precision variable coefficient ordinary differential equation) provides the new species concentrations to the CFD code, which calculates the change in specific internal energy of each computational cell.

In [45] it can be found that the direct integration model provides the best results under the low temperature combustion conditions with long ignition delays.

1.3 Conservation equations for reacting flows

In fluid mechanics any physical system can be completely described with three conservation equations:

- *continuity equation*: which ensures the conservation of mass;
- *momentum equation*: which ensures the conservation of momentum[3];
- *energy equation*: which guarantees the conservation of energy[4].

Besides these equations, a further equation of state is needed to determine the state of the fluid.

[3] Also known as 'Newton's law'.

[4] The energy equation is the first principle of thermodynamics.

Conservation equations are often written in a differential form and become of the kind of convection-diffusion if both convective flux and diffusive flux are considered.

The convective flux represents the amount of the physical variable which is transported by the fluid flow. This flux is proportional to the velocity of the flow and appears as a first order partial derivative term in the equation.

The diffusive flux, instead, takes account of the amount of the variable transported by the presence of its gradient. This phenomenon is described through the Laplace operator, which is a second order partial derivative term.

The convection-diffusion conservation equation for a general scalar quantity ϕ can be written as

$$\frac{\partial \phi}{\partial t} + \overrightarrow{\nabla} \cdot \phi \overrightarrow{u} = \overrightarrow{\nabla} \cdot \left(k\rho \overrightarrow{\nabla} \phi \right) + Q_v + \overrightarrow{\nabla} \cdot \overrightarrow{Q_s} \tag{1.7}$$

where Q_v is a volume source term and $\overrightarrow{Q_s}$ is a surface source term.

1.3.1 Continuity equation

The continuity equation is referred to the conservation of the scalar ρ, which is the gas phase density.

In this equation the Laplacian term disappears, due to the fact that mass does not diffuse but it is only transported by the flow. The continuity equation is

$$\frac{\partial \rho}{\partial t} + \frac{\partial \left(\rho u_i \right)}{\partial x_i} = \rho \dot{S} \tag{1.8}$$

where i is a generic spatial direction and $\dot{S}$ is a source term due to the presence of the liquid phase. The latter term is positive, because of the evaporation of the Diesel spray injected in the control volume.

1.3.2 Momentum equation

The momentum equation refers to the conservation of the product $\rho \overrightarrow{u}$, which is not affected by the diffusive flux, but only by the convective one.

In this equation several source terms appear: a stress tensor, describing the fluid deformation due to internal forces, $\rho \overrightarrow{g}$ due to the gravity acceleration and a source term due to the interaction between the liquid phase and the gas phase.

These considerations lead to

$$\frac{\partial \rho u_j}{\partial t} + \frac{\partial \rho u_i u_j}{\partial x_i} = -\frac{\partial p}{\partial x_j} + \frac{\partial \tau_{ij}}{\partial x_i} + \rho g_j + f_j^s \tag{1.9}$$

where p is the isotropic pressure, τ_{ij} is the symmetric stress tensor and f_j^s is the rate of momentum gain due to the interaction of the liquid spray with the gas phase.

Assuming a Newtonian fluid, τ_{ij} results

$$\tau_{ij} = \mu \left[\left(\frac{\partial u_j}{\partial x_i} + \frac{\partial u_i}{\partial x_j} \right) - \frac{2}{3} \left(\overrightarrow{\nabla} \cdot \overrightarrow{u} \right) \delta_{ij} \right] \tag{1.10}$$

where μ is the dynamic viscosity and δ_{ij} is the Kronecker delta.

1.3.3 Energy equation

According to [39], several forms of the energy conservation equation exist. The one adopted in this study is written for the enthalpy h, defined as

$$h = \sum_{k=1}^{n_s} Y_k \left(\Delta h_{f,k}^0 + \int_{T_0}^{T} c_{p_k} dT \right) \tag{1.11}$$

where n_s is the total number of species, k is the generic chemical species, Y_k is its mass fraction, c_{p_k} is its specific heat at constant pressure, T_0 is a reference temperature and $\Delta h_{f,k}^0$ is the heat of formation of k at the reference temperature.

Considering that energy can be transported by its gradient and by the flow leads to

$$\frac{\partial \rho h}{\partial t} + \frac{\partial \rho u_i h}{\partial x_i} = \frac{Dp}{Dt} - \frac{\partial j_i^q}{\partial x_i} + \dot{q}_s - \dot{q}_r \tag{1.12}$$

where the diffusive transport is accounted in the term j_i^q. As proposed in [13], this term results

$$j_i^q = -\lambda \frac{\partial T}{\partial x_i} + \sum_{k=1}^{ns} j_{i,k} h_k \tag{1.13}$$

where j_i^q consists of two parts: the first one accounts for the thermal diffusivity of the fluid and the second one is related to the enthalpy transport due to species diffusion.

The other two source terms respectively describe the heat transfer due to the presence of the liquid spray and the radiative heat loss, which is assumed to be negligible in this work.

1.3.4 Averaging the equations

As described in [39], in computational fluid dynamics there are three main approaches available to describe turbulent combustion processes: the *Reynolds*

Averaged Navier Stokes one, the *Large Eddy Simulations* one and the *Direct Numerical Simulations* one.

In the present study a Reynolds Averaged Navier Stokes (often abbreviated as RANS) approach is developed. This computation technique solves for the mean values of all quantities, which are obtained by averaging the instantaneous balance equations. This causes a lack of informations which can be gained from the simulation, but allows to strongly reduce the computational costs.

Unfortunately, several unclosed terms appear during averaging and so some closure models are needed: a turbulence model deals with the flow dynamics and a turbulent combustion model describes the species conversion and heat release phenomena.

There are two methods to average the balance equations: the Reynolds averaging, available for constant density flows, and the Favre averaging, useful for variable density flows.

The Reynolds averaging consists in splitting the generical quantity f into a mean and a fluctuating component, which leads to

$$f = \overline{f} + f' \tag{1.14}$$

where $\overline{f'} = 0$.

In variable density flows, like the ones studied in this work, several source terms due to the correlation between density and quantity fluctuations appear and so a mass-weighted average is preferred. This procedure is called 'Favre averaging', in which the generical quantity f results

$$f = \widetilde{f} + f'' \tag{1.15}$$

where

$$\widetilde{f} = \frac{\overline{\rho f}}{\overline{\rho}} \tag{1.16}$$

and $\widetilde{f''} = 0$.

Applying the latter averaging procedure to the instantaneous balance equations yields the Reynolds Averaged Navier Stokes equations, which are reported below.

$$\frac{\partial \overline{\rho}}{\partial t} + \frac{\partial \left(\overline{\rho}\widetilde{u_i}\right)}{\partial x_i} = \overline{\rho}\widetilde{\dot{S}} \tag{1.17}$$

$$\frac{\partial \overline{\rho}\widetilde{u_j}}{\partial t} + \frac{\partial \overline{\rho}\widetilde{u_i}\widetilde{u_j}}{\partial x_i} = -\frac{\partial \overline{p}}{\partial x_j} + \frac{\partial \overline{\tau_{ij}}}{\partial x_i} - \frac{\partial \widetilde{\overline{\rho}u_j''u_i''}}{\partial x_i} + \overline{\rho}g_j + \widetilde{f_j^s} \tag{1.18}$$

$$\frac{\partial \overline{\rho}\widetilde{h}}{\partial t} + \frac{\partial \overline{\rho}\widetilde{u_i}\widetilde{h}}{\partial x_i} = \frac{\overline{Dp}}{Dt} - \frac{\partial \overline{j_i^q}}{\partial x_i} - \frac{\partial \widetilde{\overline{\rho}u_i''h''}}{\partial x_i} + \widetilde{\dot{q}_s} - \widetilde{\dot{q}_r} \tag{1.19}$$

Equations (1.17), (1.18) and (1.19) are, respectively, the RANS continuity equation, the RANS momentum equation and the RANS energy equation.

Despite no additional terms occur in the continuity equation, several unclosed terms appear in the other ones.

The source term $\widetilde{u_j'' u_i''}$ is called 'Reynolds stress' and is closed by a turbulence model. This term is generally described like the viscous tensor τ_{ij} adopted for Newtonian fluids:

$$\overline{\rho}\widetilde{u_j'' u_i''} = -\mu_t \left(\frac{\partial \widetilde{u_j}}{\partial x_i} + \frac{\partial \widetilde{u_i}}{\partial x_j} - \frac{2}{3}\delta_{ji}\frac{\partial \widetilde{u_k}}{\partial x_k} \right) + \frac{2}{3}\overline{\rho}k \tag{1.20}$$

where $k = \sum_{k=1}^{3} \frac{1}{2}\widetilde{u_k'' u_k''}$ is the turbulent kinetic energy, δ_{ji} is the Kronecker delta and μ_t is a turbulent dynamic viscosity, which must be evaluated.

In this work μ_t is calculated through the two-equations model proposed by Jones and Launder[5], very popular because of its simplicity and its cost effectiveness.

The turbulent viscosity μ_t is estimated as

$$\mu_t = \overline{\rho} C_\mu \frac{k^2}{\varepsilon} \tag{1.21}$$

where k and ε are calculated through the solution of a two-equations system:

$$\frac{\partial \overline{\rho}k}{\partial t} + \frac{\partial \overline{\rho}\widetilde{u_i}k}{\partial x_i} = \frac{\partial}{\partial x_i}\left[\left(\mu + \frac{\mu_t}{\sigma_k} \right) \frac{\partial k}{\partial x_i} \right] - \overline{\rho}\widetilde{u_j'' u_i''}\frac{\partial \widetilde{u_i}}{\partial x_j} - \overline{\rho}\varepsilon \tag{1.22}$$

$$\frac{\partial \overline{\rho}\varepsilon}{\partial t} + \frac{\partial \overline{\rho}\widetilde{u_i}\varepsilon}{\partial x_i} = \frac{\partial}{\partial x_i}\left[\left(\mu + \frac{\mu_t}{\sigma_\varepsilon} \right) \frac{\partial \varepsilon}{\partial x_i} \right] - C_{\varepsilon 1}\frac{\varepsilon}{k}\overline{\rho}\widetilde{u_j'' u_i''}\frac{\partial \widetilde{u_i}}{\partial x_j} - C_{\varepsilon 2}\overline{\rho}\frac{\varepsilon^2}{k} \tag{1.23}$$

This model uses some constants which usually require to be tuned. The values used in the simulations present in this study are listed in table (1.1).

C_μ	σ_k	σ_ε	$C_{\varepsilon 1}$	$C_{\varepsilon 2}$
0.09	1.00	1.30	1.44	1.92

Table 1.1: constants for the $k - \varepsilon$ model.

Further informations about using this model in computational fluid dynamics can be found in [39].

[5] This model is known as '$k - \varepsilon$' model. Further informations can be found in [20].

The term $\widetilde{u_i''h''}$, which is present in equation (1.19), represents the convective enthalpy transport by turbulent fluctuations and can be calculated as

$$\widetilde{\overline{\rho}u_i''h''} = -\frac{\mu_t}{Pr_t}\frac{\partial\widetilde{h}}{\partial x_i} \tag{1.24}$$

where Pr_t is the turbulent Prandtl number, defined as

$$Pr_t = \frac{\mu_t C_p}{\lambda} \tag{1.25}$$

assumed to be equal to 0.85. The turbulent dynamic viscosity μ_t is estimated through the turbulence model, C_p is the specific heat at constant pressure of the mixture and λ is the thermal conductivity of the fluid.

Chapter 2

The Representative Interactive Flamelet model

In this chapter some theoretical tools useful to study diffusive flames are discussed: the flamelet concept, the mixture fraction and the scalar dissipation rate. After that, the Representative Interactive Flamelet model is explained, showing how the interaction with the physical domain takes place through the evaluation of particular flamelet parameters.

2.1 The Flamelet concept

Flames generated by Diesel combustions can be mostly classified as diffusive. For such kind of flames two boundary states must be considered: fuel and oxidizer, that are initially separated, diffuse towards the reaction zone where they burn and generate heat.

A diffusion flame usually lies along the points where mixing produces a stoichiometric (or nearly stoichiometric) mixture [39], in fact, far away from this zone, the mixture is either too rich or too lean to burn. This causes the flame to be unable to propagate, making diffusion flames more sensitive to velocity perturbations and turbulence than the premixed ones.

Compared to premixed flames, diffusion flames show less burning efficiency, due to the mixing process, which limits the speed of the species conversion phenomena.

In order to carry out a successful analysis, some theoretical tools are introduced in the following sections: the *mixture fraction* and the *flamelet* concept.

2.1.1 Mixture fraction

A simple derivation of the mixture fraction scalar is described in [39]. Before starting to explain the procedure, some assumptions are introduced:

- thermodynamic pressure is costant and Mach numbers are small;
- all the species have the same diffusion coefficient D;
- the heat capacities are the same for every species and constant: $C_{p,k} = C_p$.

Considering that the reaction involves only fuel (indicated with the 'F' subscript) and oxidizer (indicated with the 'O' subscript), leads to

$$\nu_F F + \nu_O O \longleftrightarrow \nu_P P \tag{2.1}$$

where P stands for the products. Mass fractions and temperature follow three balance equations given by

$$\frac{\partial \rho Y_F}{\partial t} + \frac{\partial \rho u_i Y_F}{\partial x_i} = \frac{\partial}{\partial x_i}\left(\rho D \frac{\partial Y_F}{\partial x_i}\right) + \dot{\omega_F} \tag{2.2}$$

$$\frac{\partial \rho Y_O}{\partial t} + \frac{\partial \rho u_i Y_O}{\partial x_i} = \frac{\partial}{\partial x_i}\left(\rho D \frac{\partial Y_O}{\partial x_i}\right) + s\dot{\omega_F} \tag{2.3}$$

$$\frac{\partial \rho T}{\partial t} + \frac{\partial \rho u_i T}{\partial x_i} = \frac{\partial}{\partial x_i}\left(\frac{\lambda}{C_p} \frac{\partial Y_F}{\partial x_i}\right) - \frac{Q}{C_p}\dot{\omega_F} \tag{2.4}$$

where $\dot{\omega_F}$ is the fuel reaction rate, s is the mass stoichiometric ratio and Q is the heat release per unit mass of the reaction. Lewis numbers, defined as

$$Le = \frac{\lambda}{\rho C_p D} \tag{2.5}$$

are assumed to be 1 in this work: this means that the thermal diffusivity is equal to the diffusion coefficient for each species.

Equations (2.2), (2.3) and (2.4) show that three particular passive scalars z_1, z_2 and z_3, defined as

$$z_1 = sY_F - Y_O \tag{2.6}$$

$$z_2 = \frac{C_p T}{Q} + Y_F \tag{2.7}$$

$$z_3 = s\frac{C_p T}{Q} + Y_O \tag{2.8}$$

follow the same balance equation:

$$\frac{\partial \rho z_j}{\partial t} + \frac{\partial \rho u_i z_j}{\partial x_i} = \frac{\partial}{\partial x_i}\left(\rho D \frac{\partial z_j}{\partial x_i}\right) \tag{2.9}$$

with $j = 1, 2, 3$. These passive scalars have different boundary conditions and they can be normalized in order to become 1 in the fuel stream and 0 in the oxidizer stream:

$$Z = \frac{z_1 - z_1^O}{z_1^F - z_1^O} = \frac{z_2 - z_2^O}{z_2^F - z_2^O} = \frac{z_3 - z_3^O}{z_3^F - z_3^O} \tag{2.10}$$

These normalized scalars can be considered equal since they follow the same convection-diffusion equation and have the same boundary conditions. The scalar Z is called *mixture fraction* and in this study follows this balance equation:

$$\frac{\partial \rho Z}{\partial t} + \frac{\partial \rho u_i Z}{\partial x_i} = \frac{\partial}{\partial x_i}\left(\rho D_Z \frac{\partial Z}{\partial x_i}\right) + \rho \dot{S} \tag{2.11}$$

where $\rho \dot{S}$ is a source term due to the liquid spray evaporation, which makes Z a non-conserved scalar.

Averaging equation (2.11) yields

$$\frac{\partial \overline{\rho} \widetilde{Z}}{\partial t} + \frac{\partial \overline{\rho} \widetilde{u_i} \widetilde{Z}}{\partial x_i} = -\frac{\partial \overline{\rho} \widetilde{u_i'' Z''}}{\partial x_i} + \overline{\rho} \widetilde{\dot{S}} \tag{2.12}$$

which involves the derivation of an additional equation for the variance of the mixture fraction $\widetilde{Z''^2}$.

$$\begin{aligned} \frac{\partial \overline{\rho} \widetilde{Z''^2}}{\partial t} + \frac{\partial \overline{\rho} \widetilde{u_i} \widetilde{Z''^2}}{\partial x_i} \;=\; & -\frac{\partial \overline{\rho} \widetilde{u_i'' Z''^2}}{\partial x_i} - 2\left(\overline{\rho} \widetilde{u_i'' Z''}\right) \frac{\partial \widetilde{Z}}{\partial x_i} - \underbrace{2\overline{\rho} D \widetilde{\left(\frac{\partial Z''}{\partial x_i}\right)^2}}_{\text{scalar dissipation rate term}} + \\ & + \underbrace{2\left(1 - \widetilde{Z}\right) \overline{\rho} \widetilde{Z'' \dot{S}} - \overline{\rho} \widetilde{Z''^2 \dot{S}}}_{\text{evaporation source terms}} \end{aligned} \tag{2.13}$$

In the last two equations several unclosed terms appear: while the modelling of the evaporation terms and the scalar dissipation rate terms will be discussed later, the final closure of the turbulent transport term derived in [13] is presented:

$$\frac{\partial \overline{\rho} \widetilde{Z}}{\partial t} + \frac{\partial \overline{\rho} \widetilde{u_i} \widetilde{Z}}{\partial x_i} = \frac{\partial}{\partial x_i}\left(\frac{\mu_t}{Sc_{t,Z}} \frac{\partial \widetilde{Z}}{\partial x_i}\right) + \overline{\rho} \widetilde{\dot{S}} \tag{2.14}$$

$$\frac{\partial \overline{\rho}\widetilde{Z''^2}}{\partial t} + \frac{\partial \overline{\rho}\widetilde{u}_i\widetilde{Z''^2}}{\partial x_i} = \frac{\partial}{\partial x_i}\left(\frac{\mu_t}{Sc_{t,Z''^2}}\frac{\partial \widetilde{Z''^2}}{\partial x_i}\right) + 2\frac{\mu_t}{Sc_{t,Z}}\left(\frac{\partial \widetilde{Z}}{\partial x_i}\right)^2 - \overline{\rho}\widetilde{\chi} + \underbrace{2\left(1-\widetilde{Z}\right)\widetilde{\overline{\rho}Z''\dot{S}} - \widetilde{\overline{\rho}Z''^2\dot{S}}}_{\text{evaporation source terms}} \tag{2.15}$$

where Sc_t is the turbulent Schmidt number[1], and $\widetilde{\chi}$ is the scalar dissipation rate, defined as

$$\widetilde{\chi} = 2D\widetilde{\left(\frac{\partial Z''}{\partial x_i}\right)^2} \tag{2.16}$$

which will be described later.

2.1.2 Flame structure in the Z-space

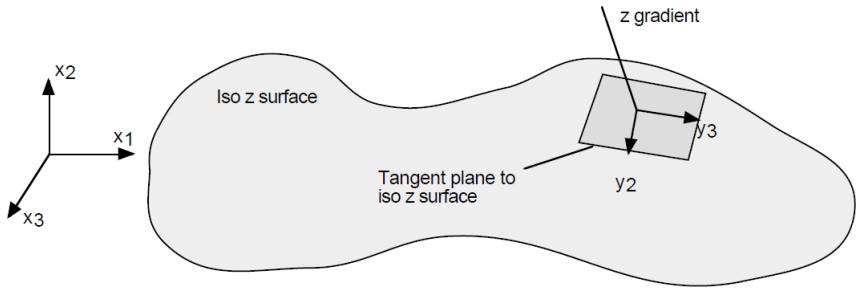

Figure 2.1: variable change from the physical space to the Z-space [39].

The introduction of the mixture fraction Z gives the possibility to reduce the number of variables. This is consistent only if an additional assumption is made: the flame structure depends only on mixture fraction Z and on time t. This assumption can be summarized as

$$T = T\left(Z, t\right) \tag{2.17}$$

$$Y_k = Y_k\left(Z, t\right) \tag{2.18}$$

and justified by changing the variables in the species and temperature equations from (x_1, x_2, x_3, t) to (Z, y_2, y_3, t) like explained in figure (2.1).

If the flame is thin, compared to the flow and wrinkling scales, gradients along y_2 and y_3 are negligible (against the one along the Z direction, which

[1] The Schmidt number is defined as $Sc = \frac{\mu}{\rho D}$ and represents the ratio between momentum diffusivity and mass diffusivity. In this situation it is used to describe turbulence and it is assumed to be equal to 0.9.

is normal to the flame). This fact makes the flame structure locally one-dimensional and only function of time and Z. This leads the flame front to be viewed as an ensemble of small laminar flames also called *flamelets*.

In [13], Hasse shows the two methods proposed by Peters for the derivation of the first-order flamelet equations for the species mass fraction, which are reported below[2]:

$$\rho\frac{\partial Y_i}{\partial t} - \rho\frac{\chi}{2}\frac{\partial^2 Y_i}{\partial Z^2} = \dot{m}_i \tag{2.19}$$

$$\begin{aligned}\rho\frac{\partial T}{\partial t} - \rho\frac{\chi}{2}\frac{\partial^2 T}{\partial Z^2} \quad &- \quad \rho\frac{\chi}{2c_p}\left[\sum_{i=1}^{ns} c_{p_i}\frac{\partial Y_i}{\partial Z} + \frac{\partial c_p}{\partial Z}\right]\frac{\partial T}{\partial Z} = \\ &= \quad \frac{1}{c_p}\left(\frac{\partial p}{\partial t} - \sum_{i=1}^{ns}\dot{m}_i h_i\right)\end{aligned} \tag{2.20}$$

where $\dot{m}_i$ is the chemical reaction rate for the generical species i. The temperature equation (2.20), along with equation (2.19), completely defines the flame structure in the Z-space.

2.1.3 Scalar dissipation rate

The scalar dissipation rate has been defined in (2.16) but needs further investigation.

This term has the dimensions of an inverse time and is the only space-depending term present in the flamelet equations, which are, in this way, coupled with the flow field.

Peters [37] studied a closure for χ showing its dependence from the mixture fraction Z in the particular case of a laminar, stationary counterflow diffusion flame with constant density and diffusion coefficients:

$$\chi(Z) = \frac{a_s}{\pi}e^{\left\{-2\left[\mathrm{erfc}^{-1}(2Z)\right]^2\right\}} \tag{2.21}$$

where a_s is the strain rate and erfc^{-1} is the inverse of the complementary error function.

In [21], a closure form for the scalar dissipation rate present in the $\widetilde{Z''^2}$ equation is proposed, by defining a special integral time scale:

$$\tau_Z = \frac{\widetilde{Z''^2}}{\widetilde{\chi}} \tag{2.22}$$

[2]These equations are written assuming unity Lewis numbers and negligible radiative heat losses.

which is assumed to be proportional to the turbulent eddy turnover time:

$$\frac{\tau}{\tau_Z} = c_\chi \tag{2.23}$$

where $\tau = \frac{k}{\varepsilon}$ and c_χ is a constant usually equal to 2. The scalar dissipation rate can be calculated as

$$\widetilde{\chi} = c_\chi \frac{\widetilde{\varepsilon}}{\widetilde{k}} \widetilde{Z''^2} \tag{2.24}$$

allowing equation (2.15) to be solved.

2.2 The RIF model

The Representative Interactive Flamelet (RIF) model represents a method available to couple the solution of the flamelet equations to the solution of the RANS equations.

The interaction between the physical space and the Z-space is shown schematically in figure (2.2).

In the CFD code the equations for the flow, turbulence, enthalpy, mixture fraction and its variance are solved. After that a particular flamelet parameter, the domain averaged scalar dissipation rate conditioned on stoichiometric mixture, is passed to the flamelet code, which solves the unsteady flamelet equations with time steps that can be much smaller than the CFD ones. In this way the time scales of fluid dynamics and chemistry are decoupled [4].

Once the flamelet equations are solved, the turbulent mean mass fractions $\widetilde{Y}_i(\overrightarrow{x}, t)$ are computed by integrating the flamelet solutions $Y_i(Z, t)$ with a particular probability density function of the mixture fraction.

Finally the physical temperature field is obtained combining iteratively the enthalpy field and the species mass fraction fields.

2.2.1 Evaluating the flamelet parameters

In order to solve the flamelet equations for the species mass fraction, a particular value of the scalar dissipation rate is needed: the domain averaged scalar dissipation rate conditioned on stoichiometric mixture. This value is provided by the CFD code.

The Z-dependence of the scalar dissipation rate has been given in equation (2.21). Since the strain rate a_s is unknown, this function is parametrized such that the complete distribution of χ is obtained by knowing its value at stoichiometric mixture fraction:

$$\chi(Z) = \chi(Z_{st}) \frac{f(Z)}{f(Z_{st})} \tag{2.25}$$

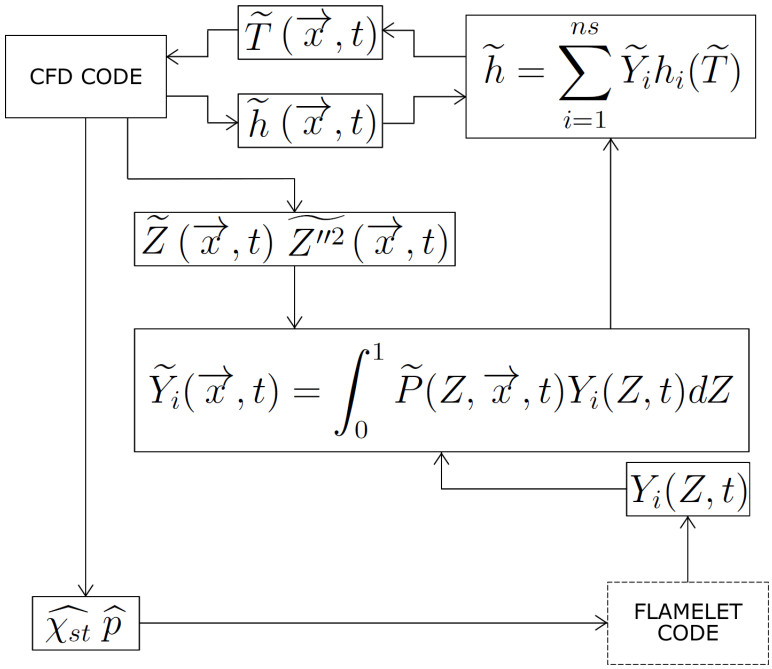

Figure 2.2: interaction between the physical space and the mixture fraction space in the Representative Interactive Flamelet model [13].

where $f(Z)$ is the Z-profile proposed by Peters and described before:

$$f(Z) = e^{\{-2\left[\mathrm{erfc}^{-1}(2Z)\right]^2\}} \tag{2.26}$$

A mean value of the conditional scalar dissipation rate at stoichiometric mixture is calculated as

$$\widetilde{\chi_{st}}(\overrightarrow{x},t) = \frac{\widetilde{\chi}}{\int_0^1 \frac{f(Z)}{f(Z_{st})}\widetilde{P}(Z)dZ} \tag{2.27}$$

where $\widetilde{\chi}$ is the scalar dissipation rate computed from the turbulent mixing field as described in equation (2.24) and $\widetilde{P}(Z)$ is the probability density function of the mixture fraction, which will be discussed later.

A surface averaged scalar dissipation rate conditioned on stoichiometric mixture is computed following Pitsch et al. [38] by converting surface integrals into volume integrals:

$$\widehat{\chi_{st}} = \frac{\int_V \widetilde{\chi_{st}}^{3/2}\overline{\rho}\widetilde{P}(Z_{st})dV'}{\int_V \widetilde{\chi_{st}}^{1/2}\overline{\rho}\widetilde{P}(Z_{st})dV'} \tag{2.28}$$

where V is the volume of the CFD domain. This value is given to the flamelet code allowing the flamelet equations to be solved.

The probability density function of the mixture fraction $\widetilde{P}(Z)$ is obtained by using the popular β-PDF approximation, which depends on the mean and the variance of Z. The PDF is calculated as

$$\widetilde{P}(Z) = \frac{Z^{\beta_1-1}(1-Z)^{\beta_2-1}}{\int_0^1 Z^{\beta_1-1}(1-Z)^{\beta_2-1}dZ} \tag{2.29}$$

where β_1 and β_2 are defined as

$$\beta_1 = \widetilde{Z}\left(\frac{\widetilde{Z}(1-\widetilde{Z})}{\widetilde{Z''^2}} - 1\right) \tag{2.30}$$

$$\beta_2 = (1-\widetilde{Z})\left(\frac{\widetilde{Z}(1-\widetilde{Z})}{\widetilde{Z''^2}} - 1\right) \tag{2.31}$$

showing that the β-PDF varies along the CFD domain. According to [8], the equation (2.29) can be rewritten using the so called 'gamma functions' as

$$\widetilde{P}(Z) = \frac{\Gamma(\beta_1+\beta_2)}{\Gamma(\beta_1)\Gamma(\beta_2)} Z^{\beta_1-1}(1-Z)^{\beta_2-1} \tag{2.32}$$

where $\Gamma(\beta)$ is defined as

$$\Gamma(\beta) = \int_0^\infty x^{\beta-1}e^{-x}dx \tag{2.33}$$

The numerical technique for the integration of the β-PDF used in this work will be discussed in section (4.3.2).

In order to solve the flamelet equation for temperature, the volume average pressure $\widehat{p}$ is needed

$$\widehat{p} = \frac{\int_V \overline{p}dV'}{\int_V dV'} \tag{2.34}$$

and provided by the CFD code.

2.2.2 Integrating species mass fractions and temperature

Integrating the flamelet solutions with the β-PDF yields

$$\widetilde{Y}_i(\overrightarrow{x},t) = \int_0^1 \widetilde{P}(Z,\overrightarrow{x},t)Y_i(Z,t)dZ \tag{2.35}$$

allowing to compute the turbulent mean mass fractions without solving any differential equation in the CFD code.

Finally, the mean temperature field is iteratively calculated combining the enthalpy field $\widetilde{h}$ and the species mass fractions

$$\widetilde{h} = \sum_{i=1}^{ns} \widetilde{Y}_i h_i(\widetilde{T}) \tag{2.36}$$

where $h_i(\widetilde{T})$ are the species enthalpies estimated using the NASA polynomials and assuming them as ideal gases.

Chapter 3

Upgrading the Representative Interactive Flamelet model

In this chapter some improvements to the original Representative Interactive Flamelet model are presented. In the first part, a closure for the source terms in the mixture fraction variance equation due to evaporation of the liquid spray is discussed. In the second part, a method which involves multiple flamelets is explained, with particular attention to the subdivision of the domain in several flamelet regions. Finally, the interaction among flamelets is studied.

3.1 Source term for $\widetilde{Z''^2}$ due to evaporation

In this section a closure for the source terms of $\widetilde{Z''^2}$ due to evaporation is presented. This method has been derived by Réveillon and Vervisch in [43] through a direct numerical simulation of droplets evaporating in a turbulent flow. Hasse, in [13], introduced this feature into the RIF model, by expanding the source terms around their mean values.

According to [43], when both gas phase and liquid phase are present and vaporization occurs, the main characteristics of micro-mixing are modified: for instance the mixture fraction spectrum and the scalar dissipation rate are sensitive to the local sources of fuel, leading to an influence of the vaporization time on the characteristic mixing time.

In equation (2.15) two unclosed terms due to evaporation appear:

$$\overline{\rho}\widetilde{S^+} = 2\left(1-\widetilde{Z}\right)\overline{\rho}\widetilde{Z''\dot{S}} \tag{3.1}$$

$$\overline{\rho}\widetilde{S^-} = -\overline{\rho}\widetilde{Z''^2\dot{S}} \tag{3.2}$$

where $\widetilde{Z''\dot{S}}$ and $\widetilde{Z''^2\dot{S}}$ are the correlation between the source of fuel $\dot{S}$ due to presence of the liquid spray and the fluctuations of mixture fraction and the variance of the mixture fraction, respectively.

While $\overline{\rho}\widetilde{S^-}$ is a small and often negligible sink term, $\overline{\rho}\widetilde{S^+}$ is a production term of the same order of the sink term $-\overline{\rho}\widetilde{\chi}$. This leads mixture fraction fluctuations to be generated by vaporization of the liquid phase and to be reduced by turbulent mixing through the scalar dissipation rate.

According to [43] also the scalar dissipation rate is increased by the vaporization phenomenon.

3.1.1 Single Droplet Model for turbulent spray

In [43], Réveillon and Vervisch introduced the conditional mean value of the vaporization source of fuel $\overline{(\dot{S} \mid Z)}$ showing through DNS results that it can be approximated as a monotonic function of Z

$$\overline{(\dot{S} \mid Z)} = \alpha_{B_Y} Z^{\xi} \tag{3.3}$$

where α_{B_Y} and ξ depend on local spray properties.

The closure for $\overline{(\dot{S} \mid Z)}$ is derived from a single droplet vaporizing in a given volume, and its control parameters are obtained from the Lagrangian spray solver.

The function α_{B_Y} is estimated considering the spray locally homogeneous and replacing the collection of droplets present in a volume $\overline{d}^{-1}$ with a unique drop of initial diameter $\overline{\Theta}_0$, which becomes of diameter $\overline{\Theta}$ once it has released fuel as vapour. These considerations yield

$$\alpha_{B_Y}(\overline{\Theta}_0, \overline{\Theta}, \overline{\rho}, \overline{d}) = \frac{2\pi\mu}{ReSc}\frac{\overline{d}}{\overline{\rho}}\frac{\ln(1+B_Y)\overline{\Theta}}{\left[\frac{\rho_l}{\overline{\rho}}\frac{\pi}{6}(\overline{\Theta}_0^3 - \overline{\Theta}^3)\overline{d}\right]^{\xi}} \tag{3.4}$$

where μ is the spray viscosity, Re is the spray Reynolds number, Sc is the spray Schmidt number, $\overline{\rho}$ is the gas density, ρ_l is the spray density, $\overline{d}$ is the local dilution factor and B_Y is the Spalding number, which is defined as

$$B_Y = \frac{(Y_F^s - Y_F^\infty)}{(1 - Y_F^s)} \tag{3.5}$$

where Y_F^s is the fuel mass fraction at the droplet surface and Y_F^∞ is the fuel mass fraction in the gas flow.

The exponent ξ accounts for the influence of turbulence on spray and can be estimated with a bisection method through the constraint

$$\overline{\rho}\widetilde{\dot{S}} = \overline{\rho}\int_Z \overline{(\dot{S} \mid Z^*)}\widetilde{P}(Z^*)dZ^* \tag{3.6}$$

where $\overline{\rho}\widetilde{\dot{S}}$ is provided by the Lagrangian solver of the spray.

According to [43], the mean vaporization sources $\overline{\rho}\widetilde{S^+}$ and $\overline{\rho}\widetilde{S^-}$ can be calculated as

$$\overline{\rho}\widetilde{S^+} = 2\overline{\rho}(1-\widetilde{Z})\int_0^{\widetilde{Z^s}} (Z^*-\widetilde{Z})\overline{(\dot{S} \mid Z^*)}\widetilde{P}(Z^*)dZ^* \tag{3.7}$$

$$\overline{\rho}\widetilde{S^-} = -\widetilde{\rho}\int_0^{\widetilde{Z^s}} (Z^*-\widetilde{Z})^2\overline{(\dot{S} \mid Z^*)}\widetilde{P}(Z^*)dZ^* \tag{3.8}$$

where $\widetilde{Z^s}$ is the mixture fraction value at the droplet surface.

By expanding the source term expression reported in (3.3) around its mean value, Hasse [13] derived a closed equation for the mixture fraction variance $\widetilde{Z''^2}$

$$\begin{aligned}\frac{\partial\overline{\rho}\widetilde{Z''^2}}{\partial t} + \frac{\partial\overline{\rho}\widetilde{u}_i\widetilde{Z''^2}}{\partial x_i} &= \frac{\partial}{\partial x_i}\left(\frac{\mu_t}{Sc_{t,Z''^2}}\frac{\partial\widetilde{Z''^2}}{\partial x_i}\right) + 2\frac{\mu_t}{Sc_{t,Z}}\left(\frac{\partial\widetilde{Z}}{\partial x_i}\right)^2 - \\ &\quad - \frac{3c_\chi C\tau}{1-e^{-3C\tau}}\frac{\widetilde{\varepsilon}}{\widetilde{k}}\widetilde{Z''^2} + \\ &\quad + \alpha_{B_Y}\left(2\left[\xi\widetilde{Z}^{\xi-1} - (\xi+1)\widetilde{Z}^\xi\right]\widetilde{Z''^2}\right)\end{aligned} \tag{3.9}$$

where $\tau = \frac{\widetilde{k}}{\widetilde{\varepsilon}}$, and C is calculated as

$$C = \alpha_{B_Y}\left[\xi\widetilde{Z}^{\xi-1} - (\xi+1)\widetilde{Z}^\xi\right] \tag{3.10}$$

Due to the high computational cost of the evaluation of these source terms, the exponent ξ is assumed to be known and equal to 2, as suggested by Réveillon and Vervisch in their DNS. In this way the function α_{B_Y} can be extracted from the costraint

$$\overline{\rho}\widetilde{\dot{S}} = \overline{\rho}\int_Z \overline{(\dot{S} \mid Z^*)}\widetilde{P}(Z^*)dZ^* = \overline{\rho}\int_Z \alpha_{B_Y}(Z^*)^\xi\widetilde{P}(Z^*)dZ^* \tag{3.11}$$

leading equation (3.9) to be closed with minimal computational cost.

3.2 The Eulerian Particle Flamelet model

In a Diesel engine the turbulent flow field and the mixture fraction distribution are non-homogeneous, so the scalar dissipation rate varies with space and time. Since the scalar dissipation rate spatial distribution determines the flamelet solutions, different flamelet histories must be calculated if this parameter varies too much in the physical domain [4].

Barths et al. [3] developed a multiple RIF model and used it to simulate combustion in a direct injection Diesel engine.

In this model several marker particles are introduced, each one representing the history of a flamelet which depends on the path that the particle takes through the turbulent flow field.

Due to the presence of these marker particles, integrating the flamelet solutions with the β-PDF leads to an equation different from the one reported in (2.35):

$$\widetilde{Y}_i(\overrightarrow{x},t) = \int_{\overrightarrow{x_0}}^{\overrightarrow{x}} \left(\int_0^1 \widetilde{P}(Z, \overrightarrow{x_0^+}, \overrightarrow{x}, t) Y_i(Z, \overrightarrow{x_0^+}, t) dZ \right) d\overrightarrow{x_0^+}$$

where $\overrightarrow{x_0}$ is the origin of a particle and $\overrightarrow{x}$ its current location.

According to [3], the latter equation can be written as

$$\widetilde{Y}_i(\overrightarrow{x},t) = \sum_{l=1}^{n_f} \widetilde{I}_l(\overrightarrow{x},t) \int_0^1 \widetilde{P}(Z,\overrightarrow{x},t) Y_{i,l}(Z,t) dZ \tag{3.12}$$

where n_f is the number of flamelets, $Y_{i,l}(Z,t)$ is the solution of the flamelet l equation for the species i and $\widetilde{I}_l(\overrightarrow{x},t)$ is the probability of finding the particle l at location $\overrightarrow{x}$ and time t.

For each flamelet, an Eulerian transport equation for the probability $\widetilde{I}_l$ has to be solved

$$\frac{\partial \overline{\rho} \widetilde{I}_l}{\partial t} + \overrightarrow{\nabla} \cdot (\overline{\rho}\,\overrightarrow{u}\,\widetilde{I}_l) = \overrightarrow{\nabla} \cdot \left(\frac{\mu_t}{Sc_t} \overrightarrow{\nabla} \widetilde{I}_l \right) \tag{3.13}$$

where Sc_t is the turbulent Schmidt number. Because of the presence of these equations this model is called *Eulerian Particle Flamelet model* (EPFM).

The surface averaged value for the scalar dissipation rate at stoichiometric mixture is computed for each flamelet l by weighting it with the probability of finding its marker particle:

$$\widehat{\chi_{st,l}} = \frac{\int_V \widetilde{I}_l(\overrightarrow{x}) \widetilde{\chi_{st}}^{3/2} \overline{\rho} \widetilde{P}(Z_{st}) dV'}{\int_V \widetilde{I}_l(\overrightarrow{x}) \widetilde{\chi_{st}}^{1/2} \overline{\rho} \widetilde{P}(Z_{st}) dV'} \tag{3.14}$$

3.2.1 Subdivision into different flamelet regions

In this work two different criteria to subdivide the CFD domain into different flamelet regions are studied: the one proposed by Barths et al. in [3], based on the variance of the scalar dissipation rate, and the one described by Vogel in [46] and Lehtiniemi et al. in [24], which defines flamelets according to the injection time.

Variation of the scalar dissipation rate

The computation starts with only one flamelet representing the whole computational domain, therefore the probability $\widetilde{I}_1$ of finding flamelet 1 is one everywhere and equation (3.13) does not need to be solved.

The scalar dissipation rate increases very fast as the injection starts, due to turbulence induced by the spray penetration, then begins to vary spatially with the evolution of the mixture field. Flamelet 1 is subdivided when the variation exceeds a certain limit and some constraints are satisfied:

- no subdivision is allowed if the mean scalar dissipation rate is still increasing;
- the standard deviation of the scalar dissipation rate must be higher than 15 per cent;
- the flamelet cannot be subdivided if it contains less mass than $0.5/n_{f,max}$ times the total mass in the domain;
- the portion of stoichiometric mixture within the flamelet being subdivided must be larger than $0.5/n_{f,r}$,

where $n_{f,max}$ is the maximum number of flamelets used for the computation and $n_{f,r}$ is the number of flamelets present in the domain.

When all the previous constraints are satisfied, flamelet 1 is subdivided and all the regions where the scalar dissipation rate is larger than the mean value are attributed to the new flamelet, by setting the probability of finding the new flamelet $\widetilde{I}_2$ equal to the one of the former flamelet $\widetilde{I}_1$, and then setting $\widetilde{I}_1 = 0$ in the same regions. After that, new mean scalar dissipation rates are computed for both flamelets.

Due to the turbulent mixing process the variance of the scalar dissipation rate continues increasing and, when all the constraints are satisfied, flamelet 1 is split again.

Injection time

In this approach every flamelet owns its portion of injected fuel. Only one flamelet is present when injection begins and all the injected mass is attributed to flamelet 1. As soon as the portion of injected mass owned by flamelet 1 reaches the value $1/n_{f,max}$, a new flamelet is created becoming the owner of the new injected fuel. The latter constraint can be summarized as

$$\frac{\int_V \overline{\rho}\widetilde{Z}_l dV'}{m_{inj}} = \frac{1}{n_{f,max}} \tag{3.15}$$

where m_{inj} is the total injected fuel and $\widetilde{Z}_l$ is the portion of mixture fraction field related to flamelet l.

The injected fuel is marked with the quantity $\widetilde{Z}_l$ and traced through a convection-diffusion equation

$$\frac{\partial \overline{\rho}\widetilde{Z}_l}{\partial t} + \frac{\partial \overline{\rho}\widetilde{u}_i\widetilde{Z}_l}{\partial x_i} = \frac{\partial}{\partial x_i}\left(\frac{\mu_t}{Sc_{t,Z}}\frac{\partial \widetilde{Z}_l}{\partial x_i}\right) + v_l\overline{\rho}\widetilde{\dot{S}} \tag{3.16}$$

where v_l is equal to 1 only if $l = n_{f,r}$ and equal to 0 if $l < n_{f,r}$. In this way evaporation of the liquid spray is accounted only in the youngest flamelet.

According to [46] the probability of finding flamelet l at location $\overrightarrow{x}$ and time t becomes

$$\widetilde{I}_l(\overrightarrow{x}, t) = \frac{\widetilde{Z}_l}{\widetilde{Z}} \tag{3.17}$$

making equation (3.13) unnecessary.

3.2.2 The Interactive Eulerian Particle Flamelet model

In the *Interactive Eulerian Particle Flamelet model*, multiple flamelets are supposed to interact each other by exchanging both heat and mass, due to mixing effects on the small scales in areas where flamelets are overlapping. The interaction process is due to the fact that the probability of finding a certain flamelet in a defined location $\widetilde{I}_l(\overrightarrow{x}, t)$ is mostly smaller than unity, leading several flamelets to be in the same location at the same time. This means that flamelets with small amounts of certain species mass fractions gain mass from the ones with big amounts, and the same is also valid for enthalpy. In this way ignition of new flamelets is caused by the already ignited ones through the interaction process.

According to [32], the flamelet interaction process is independent from the integration of the flamelet equations and can be modelled as an arbitrary

function $\Psi_{i,l}$, which can be defined as

$$Y^*_{i,l}(Z, t_{end}) = \Psi_{i,l}(Y_{i,l}(Z, t_{start}), \overrightarrow{\theta}(t_{start})) \tag{3.18}$$

where t_{start} and t_{end} are the time when interaction starts and the time when interaction finishes, $Y^*_{i,l}$ is the mass fraction of species i of flamelet l and $\overrightarrow{\theta}$ is a vector of model parameters.

In order to ensure mass conservation, the function $\Psi_{i,l}$ must satisfy the following constraint

$$\sum_{i=1}^{n_s} \Psi_{i,l} = 1 \tag{3.19}$$

where n_s is the total number of chemical species.

In his work, Mayer [32] proposed two different interaction models: the *Attack interaction* model and the *Pdf-weighted interaction* model.

Attack interaction model

The Attack interaction model is a linear model, since the species mass fraction of flamelet l after the interaction is a linear interpolation between the species mass fraction of flamelet l and the other flamelets k before interaction.

The species mass fraction i of flamelet l after interaction is calculated as

$$\begin{aligned} Y^*_{i,l}(Z) &= Y_{i,l}(Z, t_{start}) + \\ &+ \sum_{k=1}^{n_{f,r}} \frac{Q_{l,k}(t_{start})}{\tau_{l,k}(t_{start})} \left[Y_{i,k}(Z, t_{start}) - Y_{i,l}(Z, t_{start})\right](t_{end} - t_{start}) \end{aligned} \tag{3.20}$$

where $Q_{l,k}$ is called 'attack factor' and $1/\tau_{l,k}$ is called 'mixing rate'.

The coefficient $Q_{l,k}$ represents the attack of flamelet k on flamelet l and ranges from 0 to 1. All these factors are grouped in a square matrix: the 'attack tensor' $\mathbf{Q}$, which is calculated as

$$Q_{l,k}(t) = \frac{\int_V \Phi_l(\overrightarrow{x}, t)\Phi_k(\overrightarrow{x}, t)\overline{\rho}(\overrightarrow{x}, t)\widetilde{Z}_l(\overrightarrow{x}, t)dV'}{\int_V \Phi_l(\overrightarrow{x}, t)\overline{\rho}(\overrightarrow{x}, t)\widetilde{Z}_l(\overrightarrow{x}, t)dV'} \tag{3.21}$$

where $\Phi_l(\overrightarrow{x}, t)$ is a binary function defined as

$$\Phi_l(\overrightarrow{x}, t) = \begin{cases} 1 & \text{if } \widetilde{Z}_l(\overrightarrow{x}, t) > 0 \\ 0 & \text{otherwise} \end{cases} \tag{3.22}$$

The denominator of the attack factor represents the mean fuel mass enclosed by flamelet l, while the numerator is equal to the mass of flamelet l present in the overlapping area.

The mixing rate $1/\tau_{l,k}$ is a measure for the mixing intensity in the overlapping area and can be computed as

$$\frac{1}{\tau_{l,k}(t)} = \frac{\int_V \Phi_l(\overrightarrow{x},t)\Phi_k(\overrightarrow{x},t)\overline{\rho}(\overrightarrow{x},t)\frac{\widetilde{\varepsilon}(\overrightarrow{x},t)}{\widetilde{k}(\overrightarrow{x},t)}dV'}{\int_V \Phi_l(\overrightarrow{x},t)\overline{\rho}(\overrightarrow{x},t)dV'} \tag{3.23}$$

where $\widetilde{\varepsilon}$ is the dissipation rate of turbulent kinetic energy $\widetilde{k}$. Like the attack factors, all the mixing rates are grouped in the so called 'mixing rate tensor'.

The mixing rate tensor is a symmetric matrix and its components stand for a mass-weighted mean mixing rate in the overlapping area. The mixing rate is calculated assuming that in regions with high turbulent kinetic energy and low turbulent dissipation the interaction among flamelets is intense, since the exchange of mass and enthalpy is enhanced by velocity fluctuations and turbulence, which increases along with turbulent kinetic energy. Besides this fact, since the life duration of turbulent eddies is controlled by the turbulent dissipation rate, low turbulent dissipation means that it takes a longer time to the eddies to disappear, ensuring better mixing [39].

Pdf-weighted interaction model

In this approach the mass transport among flamelets is taken into account. The mean fuel mass captured by flamelet l can be calculated as

$$\widehat{m_l}(t) = \int_V \overline{\rho}(\overrightarrow{x},t)\widetilde{Z}_l(\overrightarrow{x},t)dV' \tag{3.24}$$

and can be evaluated in the Z-space through the β-PDF $\widetilde{P}(Z,\overrightarrow{x},t)$

$$\widehat{m_l}(Z_1,Z_2,t) = \int_V \int_{Z_1}^{Z_2} \overline{\rho}(\overrightarrow{x},t)\widetilde{Z}_l(\overrightarrow{x},t)\widetilde{P}(Z,\overrightarrow{x},t)dZdV' \tag{3.25}$$

where $\Delta Z = Z_2 - Z_1$ is an arbitrary interval of mixture fraction. By assuming $\widetilde{P}(Z,\overrightarrow{x},t)$ constant in a sufficiently narrow interval ΔZ, equation (3.25) can be rewritten as

$$\widehat{m_l}(Z,t) = \int_V \overline{\rho}(\overrightarrow{x},t)\widetilde{Z}_l(\overrightarrow{x},t)\widetilde{P}(Z,\overrightarrow{x},t)\Delta Z dV' \tag{3.26}$$

Introducing the β-PDF in the interaction process allows to account for the age of flamelets in the mass transfer: in fact the PDF is different in case of a young flamelet, where there are two peaks near $Z = 0$ (pure oxidizer) and $Z = 1$ (pure fuel), rather than an old one, where there is a single peak near the stoichiometric mixture fraction Z_{st}.

According to [32], the mass captured by flamelet l after interaction can be calculated as

$$\begin{aligned} \widehat{m_l}(Z,t_{end}) &= \widehat{m_l}(Z,t_{start}) + \\ &+ \sum_{k=1}^{n_{f,r}} \frac{Q^\star_{l,k}(t_{start})}{\tau^\star_{l,k}(t_{start})} \left[\widehat{m_k}(Z,t_{start}) - \widehat{m_l}(Z,t_{start})\right](t_{end}-t_{start}) \end{aligned} \tag{3.27}$$

where $Q^\star_{l,k}$ is called 'overlapping factor' and $1/\tau^\star_{l,k}$ is the 'mixing rate'.

The same equation can be written for the mean mass of the species i captured by the flamelet l

$$\begin{aligned} \widehat{m_l}(Z,t_{end})Y_{i,l}(Z,t_{end}) &= \widehat{m_l}(Z,t_{start})Y_{i,l}(Z,t_{start}) + \\ &+ \sum_{k=1}^{n_{f,r}} \frac{Q^\star_{l,k}(t_{start})}{\tau^\star_{l,k}(t_{start})} \left[\widehat{m_k}(Z,t_{start})Y_{i,k}(Z,t_{start}) - \right. \\ &+ \left. \widehat{m_l}(Z,t_{start})Y_{i,l}(Z,t_{start})\right](t_{end}-t_{start}) \end{aligned} \tag{3.28}$$

which leads to the final interaction model

$$\begin{aligned} Y^*_{i,l}(Z) = &\frac{\widehat{m_l}(Z,t_{start})Y_{i,l}(Z,t_{start})}{\widehat{m_l}(Z,t_{start}) + \sum_{k=1}^{n_{f,r}} \frac{Q^\star_{l,k}(t_{start})}{\tau^\star_{l,k}(t_{start})} \left[\widehat{m_k}(Z,t_{start}) - \widehat{m_l}(Z,t_{start})\right]\Delta t} + \\ &+ \frac{\sum_{k=1}^{n_{f,r}} \frac{Q^\star_{l,k}(t_{start})}{\tau^\star_{l,k}(t_{start})} \left[\widehat{m_k}(Z,t_{start})Y_{i,k}(Z,t_{start}) + \widehat{m_l}(Z,t_{start})Y_{i,l}(Z,t_{start})\right]\Delta t}{\widehat{m_l}(Z,t_{start}) + \sum_{k=1}^{n_{f,r}} \frac{Q^\star_{l,k}(t_{start})}{\tau^\star_{l,k}(t_{start})} \left[\widehat{m_k}(Z,t_{start}) - \widehat{m_l}(Z,t_{start})\right]\Delta t} \end{aligned} \tag{3.29}$$

where $\Delta t = t_{start} - t_{end}$ and $Y^*_{i,l}(Z)$ is the mass fraction of species i of flamelet l after interaction.

The generic term $Q^\star_{l,k}$ of the overlapping tensor $\mathbf{Q}^\star$, called 'overlapping factor', is a measure for the relative overlapping mass of two flamelets l and k. $Q^\star_{l,k}$ is defined as the ratio of the mass captured by both flamelets l and k to their total mass

$$Q^\star_{l,k}(t) = \frac{2\int_V \widetilde{Z}_l(\overrightarrow{x},t)\widetilde{Z_k}(\overrightarrow{x},t)\overline{\rho}(\overrightarrow{x},t)dV'}{\int_V \left[\widetilde{Z}_l(\overrightarrow{x},t)^2 + \widetilde{Z_k}(\overrightarrow{x},t)^2\right]\overline{\rho}(\overrightarrow{x},t)dV'} \tag{3.30}$$

where $Q^\star_{l,k} = Q^\star_{k,l}$, which makes $\mathbf{Q}^\star$ a symmetric matrix.

The mixing rate $\tau^\star_{l,k}$ accounts for the turbulence effect on the transport of mass among flamelets. Like in the attack interaction model, it is related

to the inverse of the turbulent integral time scale and it is defined as

$$\frac{1}{\tau^{\star}_{l,k}(t)} = \frac{\int_V \widetilde{Z}_l(\overrightarrow{x},t)\widetilde{Z_k}(\overrightarrow{x},t)\frac{\widetilde{\varepsilon}(\overrightarrow{x},t)}{\widetilde{k}(\overrightarrow{x},t)}\overline{\rho}(\overrightarrow{x},t)dV'}{\int_V \left[\widetilde{Z}_l(\overrightarrow{x},t)^2 + \widetilde{Z_k}(\overrightarrow{x},t)^2\right]\overline{\rho}(\overrightarrow{x},t)dV'} \tag{3.31}$$

where $\widetilde{\varepsilon}$ is the dissipation rate of turbulent kinetic energy $\widetilde{k}$.

In this study a different definition of the mixing rate is proposed

$$\frac{1}{\tau^{\star}_{l,k}(t)} = \frac{\int_V \widetilde{Z}_l(\overrightarrow{x},t)\widetilde{Z_k}(\overrightarrow{x},t)\sqrt{\frac{\widetilde{\varepsilon}(\overrightarrow{x},t)}{\nu(\overrightarrow{x},t)}}\overline{\rho}(\overrightarrow{x},t)dV'}{\int_V \left[\widetilde{Z}_l(\overrightarrow{x},t)^2 + \widetilde{Z_k}(\overrightarrow{x},t)^2\right]\overline{\rho}(\overrightarrow{x},t)dV'} \tag{3.32}$$

where ν is the flow kinematic viscosity. According to [39], $\sqrt{\frac{\nu}{\widetilde{\varepsilon}}}$ is the Kolmogorov time scale, which is the smallest of the flow. Since the definition of the mixing rate is not fully justified in [32], in this work the integral time scale has been replaced by the Kolmogorov one, providing better simulation results.

3.2.3 Flamelet libraries

In computational models based on flamelet libraries the mean species mass fractions are usually precomputed and tabulated according to the mean mixture fraction, variance of the mixture fraction and scalar dissipation rate.

Different fuels and different combinations of inlet temperatures, pressures and compositions of the mixture require separate flamelet libraries, leading to a substantial computational effort depending on the size of the chemical mechanism employed.

A comparison between a particular implementation of the Interactive Eulerian Particle Flamelet model, where flamelet equations and chemistry are solved online, and the Transient Flamelet Progress Variable model, based on flamelet libraries, has been performed by Lehtiniemi et al. [24] on a medium-duty Diesel engine operating in PCCI (Premixed Charge Compression Ignition) mode, showing reasonable agreement with the experiments for both the models.

In this work the flamelet library approach is avoided since it requires huge memory resources and considerable computational skills, in order to achieve efficient data retrieval techniques. Solving the flamelet equations for each time step, instead of using precomputed results, makes the model more flexible with respect to the fuel composition and chemical mechanism used, allowing an efficient investigation of the influence of severely different initial conditions.

Chapter 4

Application of the RIF model to CFD simulations

In this chapter, the CFD solver developed in this work, `RIFdieselFoam`, is deeply described. Since the latter application is based on OpenFOAM and the Lib-ICE library for internal combustion engine simulations, the first part of this chapter briefly presents these powerful tools for scientific research and industry.

4.1 OpenFOAM: the open source CFD toolbox

The name 'OpenFOAM' is the abbreviation for 'Open source Field Operation and Manipulation' and, as reported in [47], represents

> "...a C++ toolbox for the development of customized numerical solvers, and pre-/post-processing utilities for the solution of continuum mechanics problems, including computational fluid dynamics (CFD)."

OpenFOAM was first developed in the late 1980s at Imperial College, London, and was released as open source in 2004.

OpenFOAM can be classified as a C++ library working on Unix based operating systems and useful to solve specific problems in continuum mechanics. Its distribution contains much applications which are executables that can solve specific problems (known as *solvers*), like turbulent flow or stress analysis, or manipulate data (classified as *utilities*), like pre-processing and post-processing environments.

The open source nature characterizing OpenFOAM consists of allowing users to create new solvers and utilities with a relatively easy syntax that

closely resembles the partial differential equations being solved: this feature is achieved through object oriented programming.

In figure (4.1) the OpenFOAM structure is represented, showing its interaction with `RIFdieselFoam`, the application developed in this study, and Lib-ICE, the C++ library by ICE group of Politecnico di Milano.

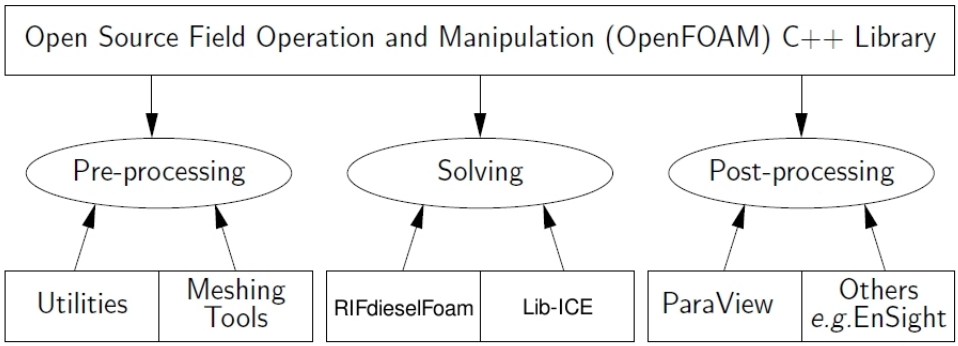

Figure 4.1: overview of OpenFOAM structure, adapted from [35].

4.2 Lib-ICE: applications and libraries for IC engine simulations

Lib-ICE is a set of applications and libraries for internal combustion engine simulations developed by the ICE group of Politecnico di Milano.

This library is based on the OpenFOAM technology and allows to model the theoretical and fluid dynamic processes taking place in internal combustion engines, providing applications and tools useful for different research topics. Specific libraries and solvers were implemented to model physical and chemical phenomena, like liquid spray dynamics and evolution, combustion processes and exhaust gases after treatment.

The code structure, depicted in figure (4.2), is very similar to the one of OpenFOAM. The 'src' directory contains several components for in-cylinder flow modeling, like a Lagrangian spray solver or different chemistry solvers, many tools for mesh handling, able to manage grid motion and topological changes, several semi-empirical models to predict soot emissions, a liquid film model and other features. The 'applications' directory is made up of three different solver categories: cold flow solvers, Diesel combustion solvers and spark-ignition combustion solvers. Finally, the 'utilities' directory groups some tools useful for the case set-up, mesh generation and post-processing.

It is important to note that Lib-ICE is continuously improved by the ICE group of Politecnico di Milano, leading to a powerful and always up-to-date research and industrial tool for internal combustion engine simulations.

The application developed in this study, `RIFdieselFoam`, deeply interacts with different libraries and solvers present in Lib-ICE, as will be explained in the following section.

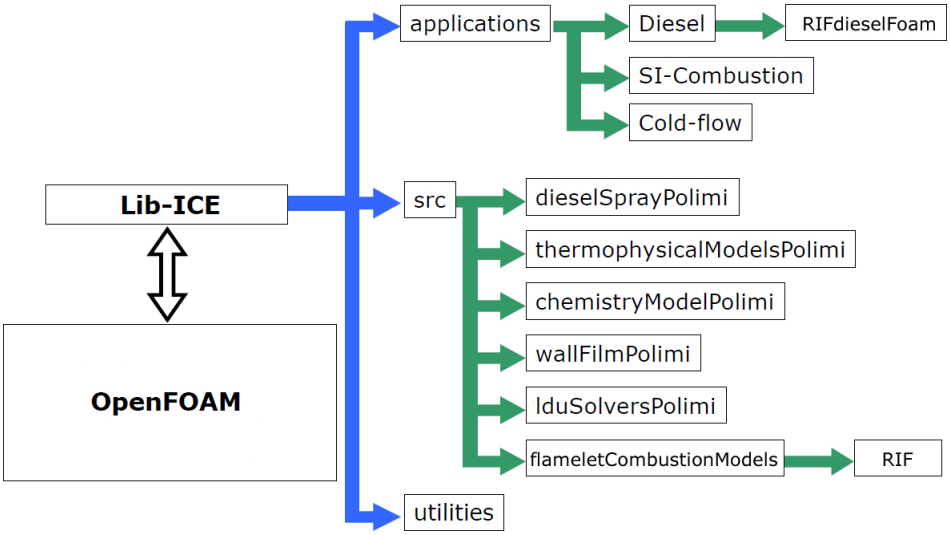

Figure 4.2: code structure of Lib-ICE, adapted from [30].

4.3 Implementing the RIF model in Lib-ICE: `RIFdieselFoam`

In this section the application `RIFdieselFoam` is described, explaining its code structure and its strong interaction with Lib-ICE. The final part of this section presents the robust and accurate algorithm of the β-PDF integration proposed by Liu et al. [27], used in the following simulations.

4.3.1 Code structure of RIFdieselFoam

`RIFdieselFoam` is an OpenFOAM application that uses the RIF model and its improved alternative versions, discussed in the previous chapters, to predict the evolution of a direct injection Diesel flame in a constant volume vessel.

To this end this application needs to use several libraries belonging to Lib-ICE, like it is depicted in figure (4.3).

The time loop begins by calling the Lagrangian spray solver owned by Lib-ICE `dieselSprayPolimi`, in which the spray is assumed to be an ensemble of droplets interacting with the Eulerian flow. The spray evolution is divided into several processes, each one described through a particular model[1]: motion of particles, injection, spray breakup, droplets collision and droplets evaporation. The Lagrangian solver provides the source terms due to evaporation present in the so called 'Z-equations' (2.14) and (3.9).

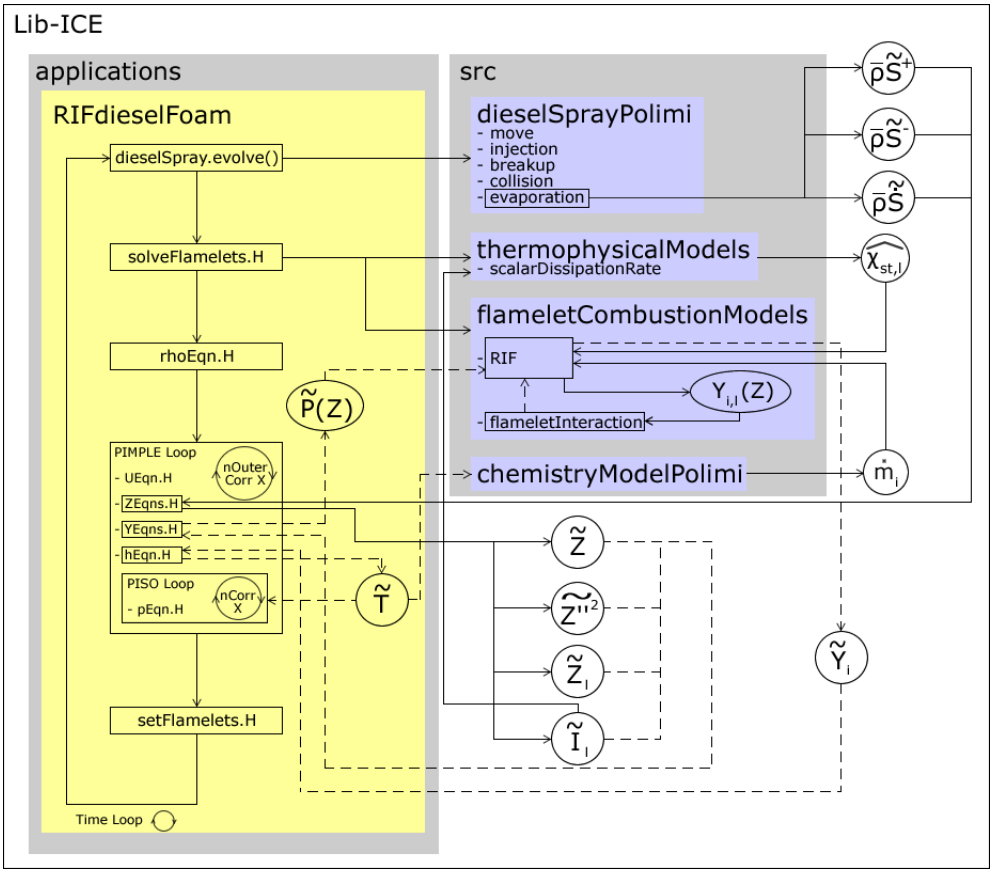

Figure 4.3: code structure of RIFdieselFoam: dashed line means a second passage through the RIF library.

Once the spray evolution for the current time step is over, the routine `solveFlamelets.H` begins. Firstly, the `scalarDissipationRate` library included in `thermophysicalModels` computes the surface averaged value for the scalar dissipation rate at stoichiometric mixture defined in equation (3.14), then the `RIF` library is called for the first time.

[1]Further informations about the models used in this study are reported in the following chapter.

`RIF` computes the species mass fractions $Y_{i,l}(Z)$ by solving the flamelet equations, closed with $\widehat{\chi_{st,l}}$ and $\dot{m}_i$ provided by `scalarDissipationRate` and `chemistryModelPolimi`[2], respectively. The species mass fractions are then passed to the `flameletInteracton` library, that calculates $Y^*_{i,l}(Z)$ using one of the interaction models discussed in the previous chapter.

The continuity equation (1.17) is solved in `rhoEqn.H`, followed by the so called 'PIMPLE loop'. The PIMPLE algorithm for pressure-velocity coupling consists of an halfway between the SIMPLE algorithm [36] (Semi-Implicit Method for Pressure-Linked Equations) and the PISO algorithm [18] (Pressure Implicit with Splitting Operators).

At the beginning of the PIMPLE loop, the momentum equation (1.18) is solved using the available pressure field, then the PISO loop takes place. As the PISO loop starts, the pressure field is solved with the predicted velocity, then the velocity field is corrected with an explicit equation of momentum and finally, with the corrected velocity, the updated pressure field is computed. The velocity field is re-evaluated using the updated pressure field and solving the explicit momentum equation again.

Once the PISO loop has finished, the solver turns back and performs an additional integration using as initial values the final values obtained after the previous loop, if necessary involving an under-relaxed value of pressure.

During the PIMPLE loop other equations are solved. Firstly, the routine `ZEqns.H` is called, solving the equations for $\widetilde{Z}$ (2.14) and for $\widetilde{Z''^2}$ (3.9). After that, the $\widetilde{I}_l$ fields and the $\widetilde{Z}_l$ fields are computed, by solving equation (3.13) or (3.16), depending on the subdivision method chosen. Only one set of equations has to be solved, because both fields are linked to each other through equation (3.17).

In `YEqns.H` the species mass fraction fields $\widetilde{Y}_i$ are computed using the `RIF` library and combining $\widetilde{I}_l$, $Y^*_{i,l}(Z)$ and the β-PDF in equation (3.12). The $\widetilde{Z}$ and $\widetilde{Z''^2}$ fields are necessary to calculate the presumed PDF according to equation (2.29).

The updated enthalpy field is computed according to equation (1.19) in `hEqn.H` and used to estimate the temperature field with the turbulent mean mass fractions $\widetilde{Y}_i$ provided by the `RIF` library through equation (2.36).

The current time step terminates with the `setFlamelets.H` routine: if the constraints necessary to subdivide the domain are satisfied (according to the subdivision criterion chosen), a new flamelet is created.

[2]Several chemistry solvers are included in this library: the one chosen for the simulations will be discussed in the following chapter.

4.3.2 Numerical integration of the β-PDF

In section (2.2) a presumed PDF for the mixture fraction Z is used to calculate the turbulent mean species mass fractions. This PDF is the popular so called β-PDF, widely used in many turbulent mixing and turbulent non-premixed combustion models, like the RIF one.

As discussed in [27], the numerical integration of the β-PDF implies several difficulties due to the possible presence of singularities either at the oxidizer side, where $Z = 0$, or at the fuel side, where $Z = 1$, rather than overflow problems when its parameters become relatively large.

In this work, numerical integration of the β-PDF is performed according to Liu et al. [27], who proposed an algorithm able to overcome both the singularity problem and the overflow problem, showing how much it is robust, efficient and accurate in a flamelet combustion model.

The above mentioned algorithm has been implemented in the RIF library and interacts with `RIFdieselFoam` like depicted in figure (4.3).

As discussed in [27], the values of the β-PDF parameters β_1 and β_2, calculated in equations (2.30) and (2.30), vary of several orders of magnitude depending on $\widetilde{Z}$ and $\widetilde{Z''^2}$, like shown in figure (4.4).

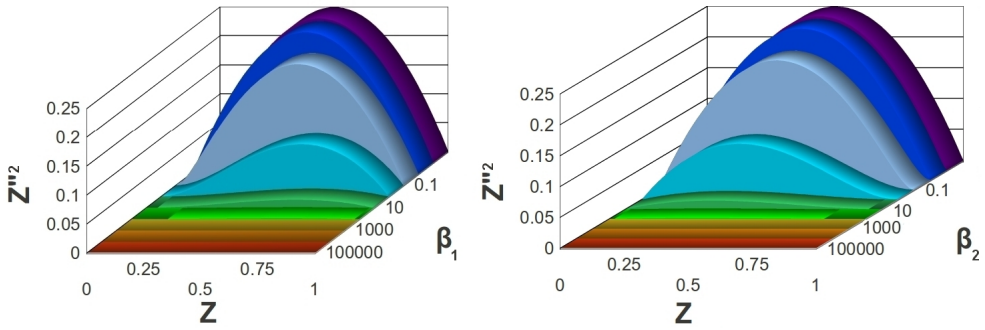

Figure 4.4: variation of parameters β_1 and β_2 as functions of $\widetilde{Z}$ and $\widetilde{Z''^2}$.

Depending on the parameters β_1 and β_2, four different PDF shapes are possible, as shown in figure (4.5). The shape indicated as 'Region I', corresponding to both β_1 and β_2 smaller than unity, has two singularities and is typical of a young flamelet, where strong fluctuations of mixture fraction occur, due to the lack of vapour and the liquid spray separated from the oxidizer.

The shapes classified as 'II' and 'IV' have only one singularity, either at the oxidizer side, in case of relatively large variances and relatively low mixture fractions, or vice versa at the fuel side.

Finally, an old flamelet has a shape similar to the one indicated as 'Region III', without singularities and with a peak around the stoichiometric mixture fraction. This situation comes out when vapour and oxidizer are well mixed and with relatively low variance of the mixture fraction.

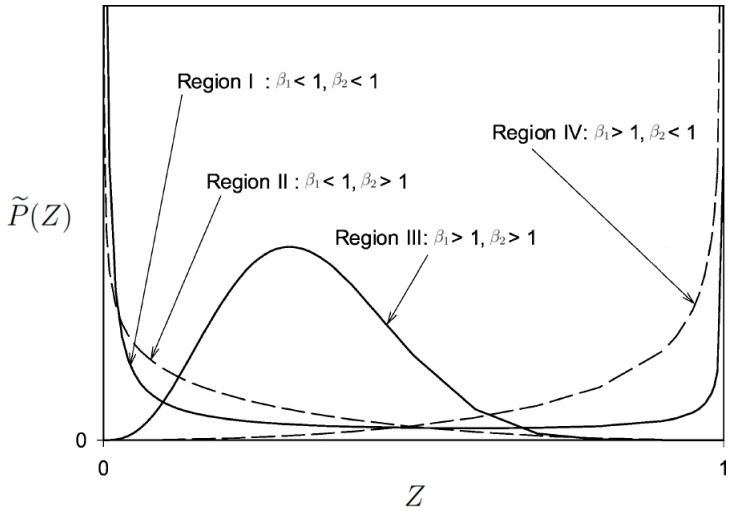

Figure 4.5: qualitative variation of the β-PDF shape with parameters β_1 and β_2, adapted from [27].

As discussed in section (2.2), the β-PDF can be rewritten through particular 'gamma functions' and, according to [8], it can be approximated by a polynomial expression.

In his work, Lentini [25] proposed a semi analytical approach, based on the properties between the beta and gamma functions, useful to integrate a density β-PDF.

Unfortunately [27], this approach cannot be used for calculation of the mean species concentrations since they cannot be fit by a polynomial expression due to their orders of magnitude variation across the reaction zone.

The numerator and the denominator of the β-PDF are subject to singularity problems at $Z = 0$, if $\beta_1 < 1$, and at $Z = 1$, if $\beta_2 < 1$. In order to overcome these difficulties, Liu et al. [27] proposed to divide the denominator

of equation (2.29) into three parts:

$$\begin{aligned}\int_0^1 Z^{\beta_1-1}(1-Z)^{\beta_2-1}dZ &= \int_0^{\varepsilon} Z^{\beta_1-1}(1-Z)^{\beta_2-1}dZ + \\ &+ \int_{\varepsilon}^{1-\varepsilon} Z^{\beta_1-1}(1-Z)^{\beta_2-1}dZ + \\ &+ \int_{1-\varepsilon}^{1} Z^{\beta_1-1}(1-Z)^{\beta_2-1}dZ\end{aligned} \tag{4.1}$$

where ε is a small parameter, assumed to be equal to 10^{-6} in this study. Assuming that

- $(1-Z)^{\beta_2-1} \approx 1$ where $Z = 0$;
- $Z^{\beta_1-1} \approx 1$ where $Z = 1$,

leads to

$$\int_0^1 Z^{\beta_1-1}(1-Z)^{\beta_2-1}dZ \approx \frac{\varepsilon^{\beta_1}}{\beta_1} + \int_{\varepsilon}^{1-\varepsilon} Z^{\beta_1-1}(1-Z)^{\beta_2-1}dZ + \frac{\varepsilon^{\beta_2}}{\beta_2} \tag{4.2}$$

allowing to solve the singularity problem in the β-PDF integration.

The central part of the domain of integration is divided into eleven intervals, whose width varies exponentially, except the range $[0.1, 0.9]$. Therefore, the integration over the interval $[\varepsilon, 1-\varepsilon]$ can be computed as

$$\int_{\varepsilon}^{1-\varepsilon} Z^{\beta_1-1}(1-Z)^{\beta_2-1}dZ = \sum_{i=1}^{11} \int_{f_i}^{f_{i+1}} Z^{\beta_1-1}(1-Z)^{\beta_2-1}dZ \tag{4.3}$$

where f_i are the extremes of integration listed in table (4.1).

f_1	f_2	f_3	f_4	f_5	f_6
ε	10^{-5}	10^{-4}	10^{-3}	10^{-2}	0.1

f_7	f_8	f_9	f_{10}	f_{11}	f_{12}
0.9	$1-10^{-2}$	$1-10^{-3}$	$1-10^{-4}$	$1-10^{-5}$	$1-\varepsilon$

Table 4.1: extremes of integration for the β-PDF approximation.

Each range is integrated by dividing it into N even segments (except the biggest interval $[0.1, 0.9]$ which is divided into M even segments) and by assuming the function to be equal to its value at the centre of the interval:

$$\int_{f_i}^{f_{i+1}} Z^{\beta_1-1}(1-Z)^{\beta_2-1}dZ \approx$$

$$\approx \sum_{k=1}^{(N \text{or} M)} \left(\frac{f_{i,k+1}+f_{i,k}}{2}\right)^{\beta_1-1} \left(1-\frac{f_{i,k+1}+f_{i,k}}{2}\right)^{\beta_2-1} (f_{i,k+1}-f_{i,k}) \quad (4.4)$$

where $N = 20$, $M = 200$, $f_{i,1} = f_i$, $f_{i,(N \text{or} M)} = f_{i+1}$ and $f_{i,k+1} = f_i + k\frac{f_{i+1}-f_i}{(N \text{or} M)}$.

When both β_1 and β_2 are greater than unity, the numerator of equation (2.29) is no more singular and has a maximum at

$$f_{max} = \frac{1}{1+\frac{\beta_2-1}{\beta_1-1}} \quad (4.5)$$

When β_1 or β_2 becomes too large, overflow may occur. Liu et al. [27] proposed to reset the value of these parameters keeping the same value of f_{max}:

- if $\beta_1 > 500$ then $\beta_1 = 500$ and $\beta_2 = \frac{\beta_1-1-f_{max}(\beta_1-2}{f_{max}}$;
- if $\beta_2 > 500$ then $\beta_2 = 500$ and $\beta_1 = \frac{1+f_{max}(\beta_2-2)}{1-f_{max}}$,

where 500 is assumed to be a reasonable limit for the parameters, sufficiently far from overflow.

It can be seen that both β_1 and β_2 remain greater than unity after the reset, allowing to keep the PDF shape similar to the original one.

Chapter 5

Validation of RIF model on the Sandia combustion vessel

The previous chapter presented an OpenFOAM application to simulate direct injection Diesel combustion in a constant volume vessel.

The aim of this work is to validate the RIF model and its evolutions on several operating conditions, in order to discover both their potentialities and their drawbacks.

The validation is carried out simulating the direct injection Diesel combustion taking place in the Sandia vessel. The choice is due to the wide range of ambient conditions which can be reproduced and the large amount of experimental data publicly available [33].

This chapter describes the experimental test realized in the Sandia National Laboratories used for validation and the CFD simulation set-up. Results and discussions will be provided in the following chapter.

5.1 The Sandia National Laboratories experiment

In this section the experiment carried out in the Sandia National Laboratories is briefly described. Detailed information can be retrieved in [33].

The SNL vessel is a constant volume vessel with full optical access, able to reproduce very different ambient conditions at the time of fuel injection:

- ambient gas temperatures ranging from 450 K to 1300 K;
- ambient gas densities ranging from 3 kg/m^3 to 60 kg/m^3;
- ambient gas oxygen concentrations ranging from 0% to 21%.

Multiple fuels can be injected in the vessel, like Diesel, n-heptane, cetane and oxygenated fuels. The injection system uses the common-rail technology and can be equipped with different nozzles, whose diameters range from 0.05 mm to 0.5 mm. The injection pressure can be adjusted from 40 MPa to 200 MPa above ambient pressure.

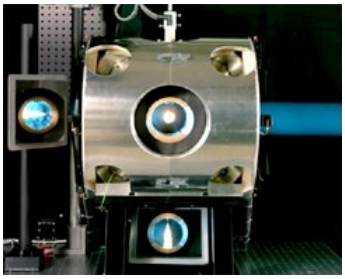

Figure 5.1: optically accessible high-temperature, high-pressure spray chamber, reproduced from [33].

5.1.1 Combustion vessel geometry

The vessel has a cubical-shaped combustion chamber with circular walls with a diameter of 105 mm, which can be seen in figure (5.2).

The fuel injector is located in one side wall and two spark plugs and a mixing fan are mounted in the top wall of the chamber.

Optical access is provided by four sapphire windows with clear apertures of 102 mm located in the other four walls.

The vessel and the inserts on which the injector, the spark plugs and the fan are mounted, are made of AISI 4340 steel[1].

Two spark plugs are used in the preliminary part of the experiment, in order to obtain the desired ambient conditions at the time of injection, by generating a premixed combustion in a high-density, fuel-lean environment. The ambient conditions are maintained uniform by the mixing fan, which rotates at 8000 rpm.

Intake and exhaust valves, pressure transducers and thermocouple inputs are inserted into the rounded corners of the cubical-shaped combustion chamber.

Further informations about the dimensions of the chamber and its features are provided in [33].

[1] AISI 4340 steel is also known as 817M40, EN24 or 1.6565, depending on the standard adopted.

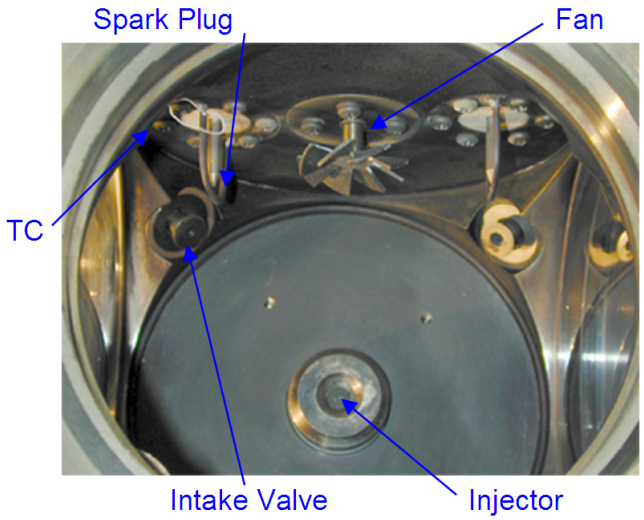

Figure 5.2: inside picture of the SNL vessel, reproduced from [33].

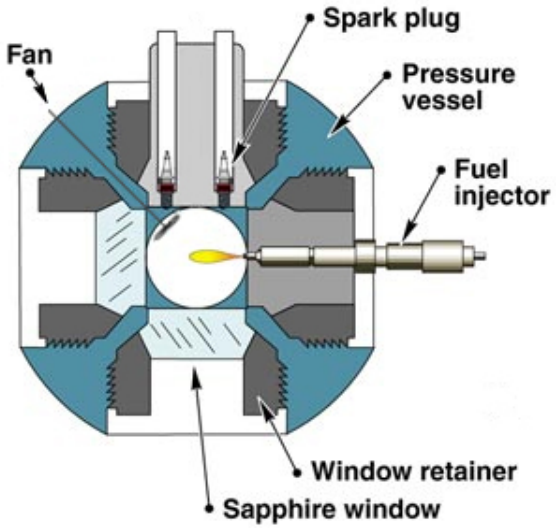

Figure 5.3: schematic cross-section of the SNL vessel, reproduced from [33].

5.1.2 The SNL experiment

In order to achieve the desired ambient conditions for the direct injection Diesel combustion, the simulation begins with a premixed spark-ignition combustion.

The vessel is initially heated at 458 K, then it is filled with a premixed combustible gas mixture. The mixing fan runs during the entire process, ensuring uniform temperature and mixture distribution up to the injection. The motion of the flow induced by the fan does not affect the Diesel combustion, since the gas velocities are negligible compared to the high velocity of the spray.

The two spark plugs mounted in the top wall of the chamber ignite the mixture, generating a premixed combustion, then the pressure slowly decreases due to the cooling of the products. The temperature field during the cooling process is measured with a fine wire platinum/platinum-rhodium (type-R) thermocouple.

The initial mass and composition of the premixed gas, along with the instant pressure of the vessel, determines the ambient gas temperature, density and composition at the time of injection.

Changing the reactant concentrations at the beginning of the simulation allows to obtain several combustion environments.

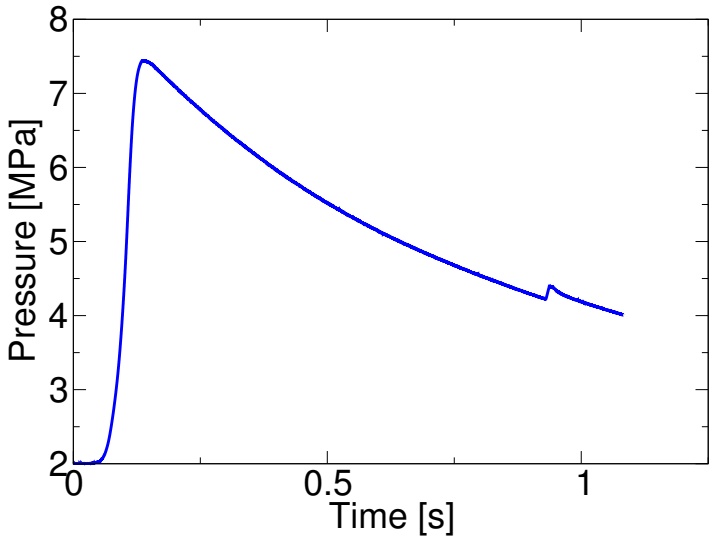

Figure 5.4: combustion vessel pressure history during the SNL experiment, reproduced from [33]. Ambient conditions at the time of injection: ambient temperature $T_a = 1000\,\mathrm{K}$, ambient density $\rho_a = 14.8\,\mathrm{kg/m^3}$, oxygen mole fraction 21% O_2.

For example, the normalized reaction which produces 100 moles of product with 21% of O_2 is

$$3.053\,C_2H_2 + 0.509\,H_2 + 28.888\,O_2 + 69.33\,N_2 \longleftrightarrow$$

$$\longleftrightarrow 21.00\,O_2 + 69.33\,N_2 + 6.11\,CO_2 + 3.56\,H_2O \tag{5.1}$$

assuming complete combustion.

When the desired experimental conditions are reached, the Diesel fuel injector opens and autoignition and combustion processes take place, generating a second pressure rise visible in figure (5.4) at about 930 ms. This pressure rise is typically small if compared to the premixed burn one. This is due to the small amount of fuel injected compared to the large mass of ambient gas already present in the vessel.

The experiments on which the RIF model is validated in this study use a hydrocarbon fuel, n-heptane, whose chemical properties are very similar to those of the conventional Diesel fuel in terms of cetane number (abbreviated as 'CN' in table (5.1)). As a consequence, it is assumed that C_7H_{16} properly represents the entire compression-ignition combustion process for what concerns flame structure and ignition delay.

ρ_f	T_f	Y_{O_2}	CN	LHV	$\alpha_{m,st}$
[kg/m^3]	[K]	[%]	[−]	[MJ/kg]	[−]
613	373	0	56	44.6	15.4

Table 5.1: characteristics of n-heptane at the injector orifice.

The fuel is injected at the pressure of 150 MPa above ambient by a Bosch, Generation 2 common rail fuel injector equipped with a single-hole minisac type axial nozzle. The nozzle has a convergent, hydroground orifice (KS1.5/86 specification by Bosch) with a diameter of 0.100 mm and a sac volume of 0.2 mm^3. The discharge coefficient C_d and the area contraction coefficient C_a for the present injector are

$$C_d = \frac{\dot{m}_f}{\rho_f A_f U_B} = 0.80 \tag{5.2}$$

$$C_a = \frac{C_d}{C_v} = 0.86 \tag{5.3}$$

where $\dot{m}_f$ is the mass flow rate, A_f is the orifice exit area, U_B is the fuel ideal velocity at the orifice exit and C_v is the velocity coefficient, which is defined

as

$$C_v = \frac{\dot{M}_f}{\dot{m}_f U_B} \tag{5.4}$$

where $\dot{M}_f$ is the momentum flow rate. The measured rate of injection is shown in figure (5.5).

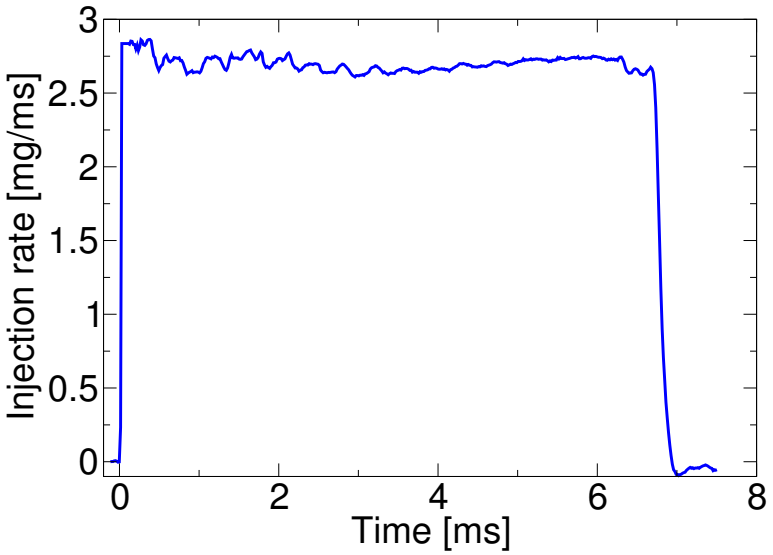

Figure 5.5: measured rate of injection, reproduced from [33]. Ambient conditions at the time of injection: ambient temperature $T_a = 1000\,\mathrm{K}$, ambient density $\rho_a = 14.8\,\mathrm{kg/m^3}$, oxygen mole fraction 21% O_2.

5.1.3 Experimental diagnostics

Thanks to the full optical access of the combustion vessel and the instruments mounted into it, several experimental diagnostics are available in [33] for the combustion tests studied in this work:

- chemiluminescence imaging provides high speed movies of the reacting spray and an estimated lift-off length;
- the pressure history allows to measure the ignition delay time.

The techniques useful to carry out these experimental data are deeply discussed in [33] and briefly described in this section.

Pressure-based ignition delay

The pressure history during the experiment is provided by a piezoelectric pressure transducer mounted into a lower corner of the vessel opposite the injector.

Pressure is measured versus time after start of injection (ASI). The time at which injection starts is detected by measurement of a HeNe laser beam, positioned at 7 mm in front of the injector tip, which is attenuated during injection.

In figure (5.4) it is shown that pressure slowly decreases after the initial premixed burn. In order to estimate the pressure rise due to the Diesel combustion, a curve fit of the cooling trend is calculated and subtracted from the original pressure history. This pressure rise causes large pressure oscillations, due to the coincidence between the frequency of these oscillations and the resonant frequency of the combustion vessel. The latter oscillations can be smoothed through Fourier-filtering, using different parameters before and after ignition. The smoothed pressure rise is shown in figure (5.6) after subtraction of the cool-down fit, showing that it takes 0.63 ms to the spray to auto-ignite.

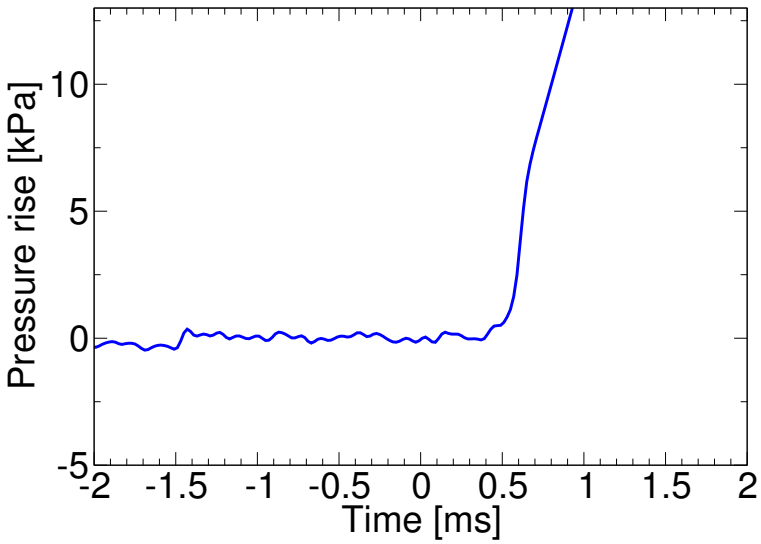

Figure 5.6: pressure history cool-down corrected, reproduced from [33]. Ambient conditions at the time of injection: ambient temperature $T_a = 1000\,\mathrm{K}$, ambient density $\rho_a = 14.8\,\mathrm{kg/m^3}$, oxygen mole fraction 21% O_2.

Chemiluminescence imaging

Chemiluminescence imaging of the injection and combustion are recorded using a high-speed CMOS camera with 'f/1.2' lens[2], 0.02 ms exposure duration and without filters.

Such a configuration allows to record the high-temperature combustion but, unfortunately, low-level cool-flame chemiluminescence is too weak to be detected with such a short exposition.

The luminosity coming from the soot incandescence is too bright to be recorded and obscures the one generated by chemiluminescence. Therefore, chemiluminescence imaging is applied to regions of the jet without soot or during transients, where soot is not present yet.

Lift-off length

The lift-off length[3] can be estimated through chemiluminescence coming from excited-state OH (OH^*). In the SNL experiment, this is achieved with time-averaged images acquired by a CCD camera.

A band-pass filter allows only the light emitted at 310 nm to pass[4], in order to capture only the OH^* chemiluminescence coming from chemical reactions in near-stoichiometric, high-heat-release regions. Also soot luminosity is present at 310 nm wavelength but it is negligible in the lift-off length region because soot is not present yet.

OH^* chemiluminescence is visible at a well-defined distance from the injector orifice, showing that the lifted reaction zone remains relatively stationary from autoignition until the end of injection.

Since two lobes of intense chemiluminescence are usually present around the spray centerline, the lift-off length is defined as the average of the distances between the injector and the locations where the chemiluminescence intensity is greater than approximately 50% of a levelling-off value.

The lift-off length is affected by changing ambient conditions: in fact the pressure rise which begins with autoignition and continues throughout fuel injection compresses the unmixed ambient gas causing the lift-length to decrease.

[2] 'f/1.2' is the so called 'F-number' also known as 'focal ratio': it is the ratio of the aperture (diameter) of the lens to its focal length.

[3] The flame generated by direct injection Diesel combustion is an example of lifted flame. The distance between the orifice (where the fuel goes into the vessel) and the flame is called 'lift-off length'.

[4] 10 nm FWHM: Full Width Half Maximum. The boundaries of the band-pass are those with an amplitude which is the 50% of the maximum one.

5.2 Getting ready for the simulations: case set-up

In this section detailed informations about the base case set-up are provided.

Firstly, numerical schemes for the terms present in the equations and the techniques used to solve the numerical differential equations are described.

Then, the Lagrangian solver for the spray present in Lib-ICE and an 'Adaptive Mesh Refinement' technique are described.

Finally, a method for solving combustion in engine simulations that reduces the computational resources required is presented, also focusing on the simplified chemical mechanism used in the simulations of this study.

5.2.1 Numerical set-up

OpenFOAM uses the 'Finite Volume' method to discretise continuum mechanics problems. According to [34], there are three main things that have to be discretised: space, time and differential equations.

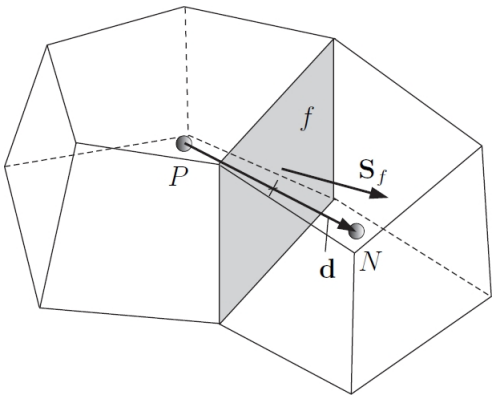

Figure 5.7: parameters in finite volume discretisation, reproduced from [34].

In the finite volume method, spatial discretisation is obtained by dividing the solution domain into a defined, but often not fixed, number of control volumes, also called cells. These cells are strictly contiguous and the ensemble of spatial locations of their vertices makes up the so called 'mesh'.

The cells are bounded by an arbitrary set of flat faces, which can be oriented as desired, without any restriction on their alignment.

Each cell owns a reference point P which is its centroid, where dependent variables, like the properties of the flow, are mostly defined. However they can be stored also on faces or vertices.

Further informations about the computational meshes used in this study (the one of the CFD domain and the one of the flamelet domain) are provided in section (5.2.3).

Time is discretised dividing the time domain into a finite number of time intervals, whose duration can vary during the simulation. In this work the time step duration is fixed and equal to 5×10^{-7} s: this value ensures a better convergence of the spray solver.

Equation discretisation consists of generating a system of algebraic equations based on the partial differential equations, which describe the physical problem, and related to discrete quantities defined at specific locations in the domain (mainly the centroids of the cells).

Each category of mathematical terms which makes up a partial differential equation can be discretised with several methods. The discretisation techniques used in this work are now presented according to [34].

The Laplacian term is integrated over a control volume (cell) and, through the Gauss theorem (which allows to switch from volume integrals to surface integrals and vice versa), is discretised as

$$\int_V \vec{\nabla} \cdot (\Gamma \vec{\nabla} \phi) dV = \int_S \vec{dS} \cdot (\Gamma \vec{\nabla} \phi) = \sum_f \Gamma_f \vec{S_f} \cdot (\vec{\nabla} \phi)_f \tag{5.5}$$

where Γ_f is the Laplacian coefficient calculated interpolating (through central differencing) the values at the centroids of the two neighbouring cells P and N

$$\Gamma_f = \frac{\overline{fN}}{\overline{PN}} \Gamma_P + \left(1 - \frac{\overline{fN}}{\overline{PN}}\right) \Gamma_N \tag{5.6}$$

and

$$\vec{S_f} \cdot (\vec{\nabla} \phi)_f = |\vec{S_f}| \frac{\phi_N - \phi_P}{|\vec{d}|} \tag{5.7}$$

Since the above discretisation is valid only on orthogonal meshes, a non-orthogonal corrector is used in this study, leading to an additional explicit term. The above approximation leads to a second order discretisation error.

Divergence terms are discretised as

$$\int_V \vec{\nabla} \cdot (\rho \phi \vec{u}) dV = \int_S \vec{dS} \cdot (\rho \phi \vec{u}) = \sum_f \vec{S_f} \cdot (\rho \vec{u})_f \phi_f \tag{5.8}$$

where ϕ_f is calculated through linear interpolation (again through central differencing) as

$$\phi_f = \frac{\overline{fN}}{\overline{PN}} \phi_P + \left(1 - \frac{\overline{fN}}{\overline{PN}}\right) \phi_N \tag{5.9}$$

The numerical scheme used in this study is a bounded TVD scheme (Total Variation Diminishing). This property, along with the numerical scheme boundedness, ensures better convergence without introducing non-physical oscillations. Further informations about TVD schemes can be found in [19] and in [11]. The above approximation leads to a first order discretisation error.

Discretisation of first order temporal derivatives is achieved following an Euler implicit scheme, which leads to

$$\frac{\partial}{\partial t}\int_V \rho\phi dV = \frac{(\rho_P\phi_P V)_n - (\rho_P\phi_P V)_o}{\Delta t} \tag{5.10}$$

where the n subscript indicates the new unknown values while the o subscript the old ones. This discretisation is first order accurate in time.

Once discretised, the partial differential equations are integrated in time over the time step Δt, following an Euler implicit scheme:

$$\int_t^{t+\Delta t}\left[\frac{\partial}{\partial t}\int_V \rho\phi dV\right]dt = \frac{(\rho_P\phi_P V)_n - (\rho_P\phi_P V)_o}{\Delta t}\Delta t \tag{5.11}$$

$$\int_t^{t+\Delta t}\left[\int_V \mathbf{A}^*\phi dV\right]dt = \mathbf{A}^*\phi_n\Delta t \tag{5.12}$$

where $\mathbf{A}^*$ is the spatial discretisation of the several spatial operators described before and ϕ_n is the new value of the generic quantity being calculated. The Euler implicit scheme is bounded, first order accurate in time and unconditionally stable.

Several solvers are available in OpenFOAM to solve the sets of linear equations discretised before. Due to the huge dimensions of the matrices involved in the computation, an iterative solver must be chosen.

In this study a solver based on the 'Conjugate Gradient' algorithm, proposed by Hestenes and Stiefel [14] in 1952, is used. In order to achieve fast convergence, the solving process is preceded by pre-conditioning.

The Pre-conditioned Conjugate Gradient solver (PCG) works only on symmetric matrices, therefore it is used only to solve the continuity equation (1.17), the flamelet equations (2.19) and (2.20), and the pressure equation in the PISO loop. The pre-conditioner for this solver is based on the Diagonal Incomplete Cholesky algorithm (DIC).

Since divergence terms generate asymmetric matrices, the momentum equation (1.18), the energy equation (1.19) and the $k-\varepsilon$ equations (1.22) and (1.23) cannot be solved with the PCG algorithm. Pre-conditioned bi-Conjugate Gradient (PBiCG), an evolution of the Conjugate Gradient algorithm which can manage asymmetric matrices, is used along with a Diagonal Incomplete LU (DILU) pre-conditioner.

Exhaustive explanations of the solvers and the pre-conditioners used in this work can be found in [11].

5.2.2 Spray set-up

In order to calculate the spray dynamics in the combustion vessel, the application developed in this study uses the Lagrangian solver implemented by Lucchini et al. in the Lib-ICE library, extensively validated and described in [31].

This solver is based on an Eulerian-Lagrangian approach, which assumes the spray to be made up by an arbitrary number of parcels, each one representing an ensemble of droplets with the same physical properties. The right number of parcels consists of a compromise between computational accuracy and costs and depends on the injected mass and the injection duration: in this study 250000 parcels are assumed to be a reasonable value.

These Lagrangian parcels evolve into the computational domain, which follows the Eulerian convection-diffusion equations already described in chapter (1). In this equations several source terms, which account for mass, momentum and energy exchange between the liquid and gas phases, appear and are provided by the spray solver.

Each parcel belonging to the spray follows different Lagrangian equations, which determine its physical properties, like position, velocity, temperature, etcetera. The latter equations are briefly reported here:

$$m_d \frac{d\overrightarrow{u_d}}{dt} = -\frac{\pi D^2}{8} \rho C_d |\overrightarrow{u_d} - \overrightarrow{u}| (\overrightarrow{u_d} - \overrightarrow{u}) + m_d \overrightarrow{g} \tag{5.13}$$

$$\frac{dm_d}{dt} = -\frac{m_d}{\tau_e} \quad \text{or} \quad \frac{dD}{dt} = -\frac{D}{3\tau_e} \tag{5.14}$$

$$\frac{dm_d}{dt} = -\frac{m_d}{\tau_b} \quad \text{or} \quad \frac{dD}{dt} = -\frac{D}{3\tau_b} \tag{5.15}$$

$$m_d \frac{dh_d}{dt} = \dot{m}_d h_v(T_d) + \pi D \kappa N u (T - T_d) f \tag{5.16}$$

which are, respectively, the droplet momentum equation, the droplet mass equation during standard evaporation, the droplet mass equation during boiling conditions and the droplet energy equation. Further details about the references of the above equations can be found in [31].

The Lagrangian solver provided by Lib-ICE uses several phenomenological models to describe processes occurring in the sub-grid length scales.

The liquid spray is introduced in the vessel through large and spherical drops, with a diameter similar to the injector nozzle and a velocity resulting from the mass flow rate profile. These large particles are affected only by the atomization process, modelled according to [15]. During penetration these particles become smaller, according to the equation

$$\frac{dD}{dt} = -C_5 \frac{L_A}{\tau_A} \tag{5.17}$$

and lose some mass, equal to

$$\Delta m_{stripped} = \rho_l \frac{1}{6} \pi N_d (D_{new}^3 - D_{old}^3) \tag{5.18}$$

per each time step. Further details about the latter equations are reported in [31].

As soon as the mass lost by a large particle reaches a certain limit (in this study assumed to be equal to 0.05 times the parent particle mass), a new particle is created, with a smaller diameter taken from a Rosin–Rammler distribution whose mean value is a function of the nozzle flow Reynolds number (see [31] for details).

As the atomization process goes on, particles become smaller and smaller, reducing their Weber number[5]. When the Weber number reaches a fixed lower limit (assumed to be 80 in this study) the particle starts following the secondary breakup model, taken from [42]. In this way, the atomization model takes into account the effects of turbulent and aerodynamic instabilities on the liquid jet surface and produces smaller droplets on which the secondary breakup model operates according to the Kelvin-Helmoltz and Rayleigth-Taylor instabilities [31].

Other sub-models are included in the Lib-ICE Lagrangian spray solver, like the evaporation model [6], the heat transfer model [41] and the model accounting for drag force on droplets [23]. According to [31], the collision phenomenon between droplets has no relevants effects on the evolution of an evaporating spray, therefore it is assumed to be negligible in this work.

The Lagrangian particles and the Eulerian domain interact each other. The first ones are characterised by the gas properties at parcel locations, which are computed from the Eulerian nodes either through interpolation

[5]The Weber number represents the ratio of the inertial force to the surface tension force and is defined as

$$We = \frac{\rho_l u^2 D}{\sigma_l}$$

where ρ_l is the liquid density, u is the liquid velocity, D is the droplet diameter and σ_l is the liquid surface tension.

(gas velocity at parcel locations is estimated along with its values at cell centers, face centers and mesh points [31]) or assuming them equal to the values of the cell centers in which the particle is. The Eulerian domain governing equations are affected by several source terms due to the liquid particles presence, which are calculated identifying the cells crossed by each parcel during the time step.

5.2.3 Mesh set-up

Two different meshes are used for the simulations carried out in this work: the one discretising the physical domain and the ones discretising the flamelet domains.

The physical domain mesh is depicted in figure (5.8). This mesh reproduces the SNL combustion vessel, which is modelled as a cube of size 108 mm × 108 mm × 108 mm. Initially, the physical computational domain consists of 14 cubical cells along each dimension, leading to 2744 cells in the entire domain.

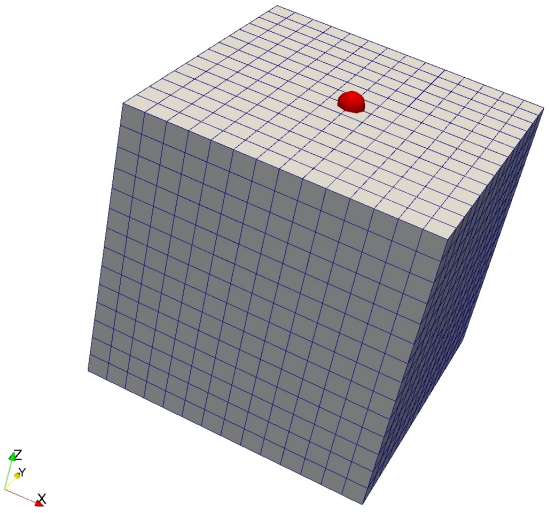

Figure 5.8: physical domain finite-volume mesh; the red sphere indicates the injector position.

This coarse mesh is progressively refined using the 'Adaptive Local Mesh Refinement' algorithm developed by Lucchini et al. in Lib-ICE and described in [31].

In order to achieve high mesh resolution where fuel-air mixing takes place ensuring reasonable computational costs, only the cells which satisfy the refinement criterion are split. According to [31], the total fuel mass fraction

in each cell is the computational field chosen as a threshold value for the refinement. The total fuel mass fraction accounts for both liquid and gas fuel and is calculated as:

$$Y_{l+g} = \frac{m_{f,l} + \rho Y_f V_{cell}}{\rho V_{cell}} \tag{5.19}$$

where $m_{f,l}$ is the liquid mass of the parcels present in the considered cell, Y_f is the fuel mass fraction in the gas phase, ρ is the gas phase density and V_{cell} is the computational cell volume.

When Y_{l+g} is greater than a threshold value, assumed to be 4 in this study, the cell is split into eight cells, introducing new Eulerian nodes at the cell centroid and at the face centres. This ALMR algorithm also allows to decrease the number of computational cells: in fact, when Y_{l+g} is smaller than a certain limit (here supposed to be 10^{-4}), the cells already refined are merged again.

In order to keep the computational costs reasonable, the maximum number of cells allowed in the computation is 100000 and each cell can be refined at the most three times. The mesh evolution during the simulation is shown in figure (5.9): at the beginning of the simulation there are 2744 cells, while at 1 ms there are 38241 cells and at 1.5 ms there are 57057 cells.

All the parameters on which the ALMR algorithm depends are defined according to the simulations described in [31].

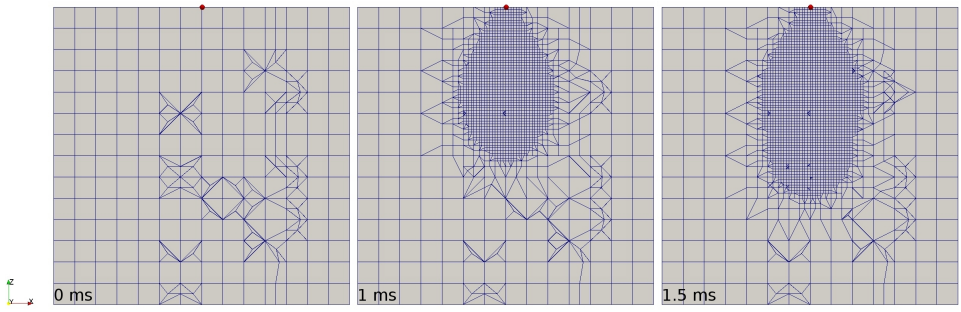

Figure 5.9: influence of the Adaptive Local Mesh Refinement algorithm on the CFD mesh; the oblique lines are due to the post-processing environment.

Despite the flamelet domains (one per each flamelet present in the computation) are one-dimensional, they are treated as particular finite volume domains. This fact allows to use the same numerical schemes and the same libraries implemented in OpenFOAM for solving both the flow and the flamelet equations.

The flamelet mesh is depicted in figure (5.10) and consists of 270 cells which remain unchanged during the simulation. Each cell has the same

square shape in the $Y-Z$ plane and is characterized by its own length along the X axis, corresponding to the mixture fraction Z dimension in the flamelet domain.

The cell dimension varies along the computational X axis in order to obtain a local refinement near the oxidizer side ($Z=0$) and near the fuel side ($Z=1$). This device is necessary because of the shape of the β-PDF typical of young flamelets. In fact, as shown in region I of figure (4.5), the PDF of young flamelets decreases very quickly at the oxidizer side and increases very quickly at the fuel side, therefore a strong local refinement is compulsory to accurately discretise the β-PDF and overcome numerical drawbacks.

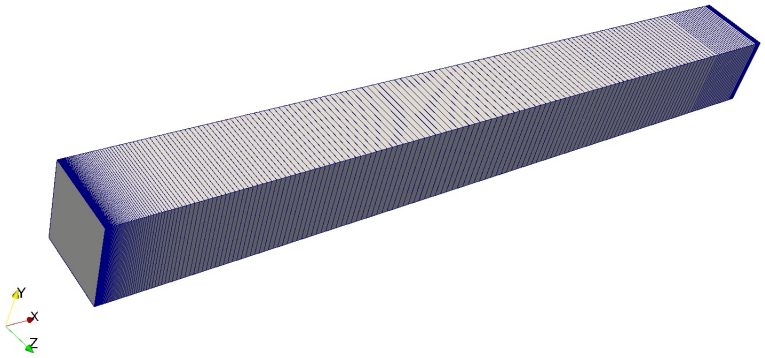

Figure 5.10: flamelet domain finite-volume mesh.

5.2.4 Chemistry solver set-up

The chemical mechanism used in the following simulations is a reduced mechanism for n-heptane, derived by Lu et al. in [29] through dimension reduction, which consists of 68 species and 283 reactions.

Using a reduced mechanism instead of a comprehensive and detailed one is necessary to achieve simulation results in a reasonable amount of time.

The reduced mechanism by Lu et al. derives from the detailed mechanism for n-heptane developed by Curran et al. in [7], which consists of 561 species and 2539 reactions.

The mechanism reduction has been performed in [28] over different parameter ranges: equivalence ratio from 0.5 to 1.5, pressure from 1 MPa to 5 MPa and initial temperature from 700 K to 1600 K.

The chemistry solver used in the simulations is based on the coupling of the Dynamic Adaptive Chemistry (DAC) reduction scheme with the *in situ* Adaptive Tabulation (ISAT) algorithm. This solver, briefly identified as

TDAC (Tabulation of Dynamic Adaptive Chemistry), has been implemented in Lib-ICE by Contino et al. and is described in [5].

The Dynamic Adaptive Chemistry method [26] reduces the number of species involved in the mechanism and, consequently, also the number of reactions which have to be simulated. This device is achieved computing a matrix that represents the error on the production and consumption of a species when another is removed from the mechanism. The error is computed between all the species and an initial set of user-defined species. In the present simulations these initial species are n-heptane, CO, CO_2, CH_2O, O_2, N_2, H_2O, OH and HO_2. The reduction scheme disables the species with an error, which also represents the strength of the direct link between two species, smaller than a threshold value, assumed to be 10^{-4} according to [5]. The reactions involving at least one of the disabled species are not taken into account by the ODE solver.

The *in situ* Adaptive Tabulation algorithm [40] stores the results of the integration of large and stiff ODE systems in order to reuse them and save computational time. The thermochemical states (completely defined by chemical composition, temperature and pressure) $\psi_0 = \psi(t_0)$ at the beginning of the time step and $\psi(t_0 + \Delta t)$ at the end of the time step, are mapped through the reaction mapping function $\mathbf{R}(\psi_0)$, which is stored to be used again. Before eventually solving the reaction equations for a requested thermochemical state ψ_q, a linear approximation of the reaction mapping is calculated as

$$\mathbf{R_l}(\psi_q) = \mathbf{R}(\psi_0) + \delta\mathbf{R_l}(\psi_0, \psi_l) \tag{5.20}$$

where $\delta\mathbf{R_l} = \mathbf{A}(\psi_0)(\psi_l - \psi_0)$. $\mathbf{A}(\psi_0)$ is the mapping gradient matrix computed according to the Jacobian of the chemical source terms. If the linear approximation of the requested reaction mapping $\mathbf{R_l}(\psi_q)$ belongs to the so called EOA region ('Ellipsoid of Accuracy', see [40] and [5] for further details), the reaction equations are not solved, allowing to save computational time. The EOA region depends on a user-defined tolerance ε_{ISAT}, assumed to be 10^{-4} in this study. The tabulation consists of a binary tree made up of nodes and leaves. The nodes store the hyperplanes in the composition space and the leaves store ψ, $\mathbf{R}(\psi)$, $\mathbf{A}(\psi)$ and the EOA. During the simulation new leaves can be added storing new $\mathbf{R}(\psi_q)$ and the EOA can grow if the local error $|\mathbf{R}(\psi_q) - \mathbf{R}(\psi_0)|$ is smaller than ε_{ISAT}.

According to [5], in internal combustion engine simulations the use of either the DAC method or the ISAT algorithm cannot reduce the computational time satisfactory. This is due to presence of mixture inhomogeneities, which reduces the number of retrieves that can be used by the ISAT algorithm, and rapid changing in the thermodynamic conditions during the

simulation, which limits the number of chemical species that can be disabled by DAC.

Therefore, Contino et al. developed a merged ISAT and DAC method, called TDAC, which combines the advantages of both the algorithms. The TDAC structure is depicted in figure (5.11).

The coupling between ISAT and DAC is achieved, when growth or addition operations are needed, by running the DAC algorithm on ψ_q and passing to the ODE solver a reduced set of species ψ_q^a, which includes only the active ones. In this way the reaction mapping $\mathbf{R}(\psi_q^a)$ is computed on a reduced mechanism and, after that, expanded by ISAT to the full composition space, leading to $\mathbf{R}(\psi_q)$.

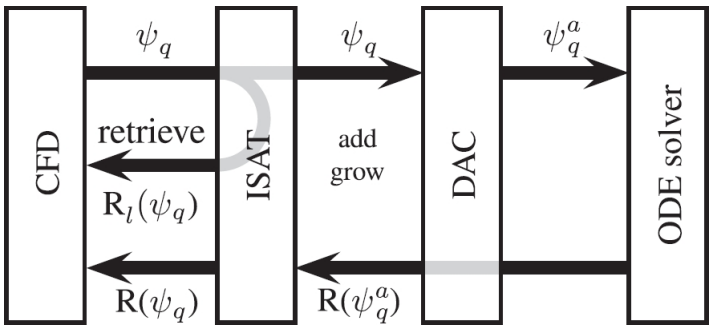

Figure 5.11: structure of the TDAC algorithm, reproduced from [5].

The solver used to integrate the system of ordinary differential equations and calculate the reaction mapping $\mathbf{R}(\psi_q^a)$ is based on the semi-implicit midpoint rule studied by Bader and Deuflhard in [1].

Chapter 6

Results and discussion

In this chapter the RIF model and its different variants, previously discussed in chapters (2) and (3) respectively, are validated by comparing the simulations results, calculated by the OpenFOAM application `RIFdieselFoam`, with the experimental data from the SNL vessel.

The validation will be achieved focusing on the pressure rise, its derivative versus time, the lift-off length and the flame shape.

Firstly, the different versions of the RIF model will be compared to experimental results for a typical Diesel combustion case. Then, the potentials of the models in the simulation of soot formation phenomena will be investigated, comparing the calculated formaldehyde and acetylene distributions with measured ones. Finally, the influence of ambient conditions on simulations will be studied, testing the reliability of the models over a wide range of operating conditions.

6.1 Validation of RIF and its evolutions

In this work the RIF model and its variations have been studied. In order to discover both the pros and cons of each model in workable time, only a careful selection of simulations is carried out.

The most efficient combination of comparisons seems to be as follows: firstly, the influence of the Single Droplet Model discussed in section (3.1) on a standard RIF simulation is investigated. Then the effect of the subdivision criterion and the flamelet interaction model are discussed. Finally a comparison among simulations with the same combination of models but different number of flamelets involved is carried out.

The ambient conditions are kept constant for all the simulations, with a set-up that aims at reproducing the operating conditions typical of a Diesel

engine at full load conditions and maximum speed. The ambient conditions for this base case are summarized in table (6.1) and the chemiluminescence imaging provided by [33] is depicted in figure (6.1). The flame is surrounded by a dashed white line, that justifies the measured value of the lift-off length, for the latter case equal to 17 mm. Going downstream from the nozzle, two different kinds of combustion can be seen: firstly, there is an area of low luminosity, from the lift-off length to 35 mm, that represents a cold rich premixed flame, followed by a steep increase of chemiluminescence, due to the presence of a diffusive flame which covers the entire head vortex.

O_2 mole fraction	Ambient temp.	Ambient density	Ambient pressure	Injected mass	Lift-off length	Ignition delay
[%]	[K]	[kg/m^3]	[MPa]	[mg]	[mm]	[ms]
21	1000	14.8	4.21	17.8	17.0	0.63

Table 6.1: base case set-up for the comparison of the RIF model with its evolutions.

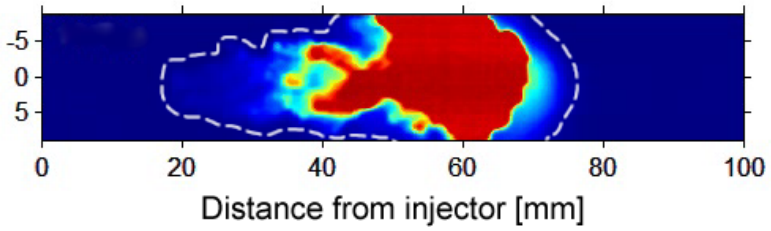

Figure 6.1: chemiluminescence imaging of the base case at 1.5 ms ASI, reproduced from [33].

At the beginning of the simulations, all the physical properties of the CFD domain are assumed uniform with zero gradient boundary conditions at the walls. In order to simulate the cooling process of the mixture prior to the injection (already described in section (5.1.2)), the wall temperature is fixed at 950 K through a fixed value boundary condition for the temperature field.

The species mass fractions fields are initialised as linear in the flamelet domain, with the mass fraction values typical of the standard air mixture at the oxidizer side ($Z = 0$) and a zero value at the fuel side ($Z = 1$). Only n-heptane is set to zero at the oxidizer side and equal to unity at the fuel side.

Also the sensible enthalpy field is assumed linear at the beginning of the simulation, with the boundary values resulting from the enthalpy of the mixture at the oxidizer side at 1000 K, according to table (6.1), and the enthalpy of n-heptane at 373 K, according to table (5.1). The initial temperature field in the flamelet domain is computed according to equation (2.36).

According to [10], a comprehensive validation of the models can be achieved by critically observing the computed heat release rate, the flame lift-off location and the flame structure. All the results provided by the simulations are compared with the experimental data reported in [33].

The computed ignition delay is measured according to [33] and corresponds both to the first time at which Y_{OH} reaches 2% of the maximum in the domain after a stable flame is established and the time of maximum rate of rise of maximum temperature. Since the two definitions approximately lead to the same results, only the mean between the latter two values is reported.

The computed lift-off length is measured both according to [33], where is defined as the first axial location of Y_{OH} reaching the 2% of its maximum in the domain, and according to [44], where it is assumed to be the distance between the injector and the iso-contour of 2200 K temperature.

6.1.1 Influence of the Single Droplet Model

In section (3.1), a Single Droplet model for the source terms of variance of the mixture fraction due to liquid spray evaporation was discussed.

In figure (6.2) the computed pressure rise is compared with the experimental one. As it can be seen, the ignition delays computed without source terms due to evaporation in the variance equation and with the Single Droplet model are both overestimated, resulting 0.68 ms and 0.70 ms respectively, against a measured value of 0.63 ms. In both cases the computed pressure rise is lower than the experimental one. This is probably due to the differences between the modelled combustion vessel, which is a cube of size 108 mm, and the real one, which is not a cube and has slightly smaller dimensions, leading to a smaller volume and a consequently higher pressure rise.

The pressure rise derivative versus time depicted in figure (6.3) represents a qualitative measure of the heat release rate. The two red and green peaks represent the computed premixed combustion, while the constant parts of the curves are the mixing controlled phase. The heat release rate during the premixed combustion is overestimated for both the simulations, but the one computed with the SDM model results higher. This is due to the longer ignition delay, which allows more liquid fuel to evaporate, causing a more

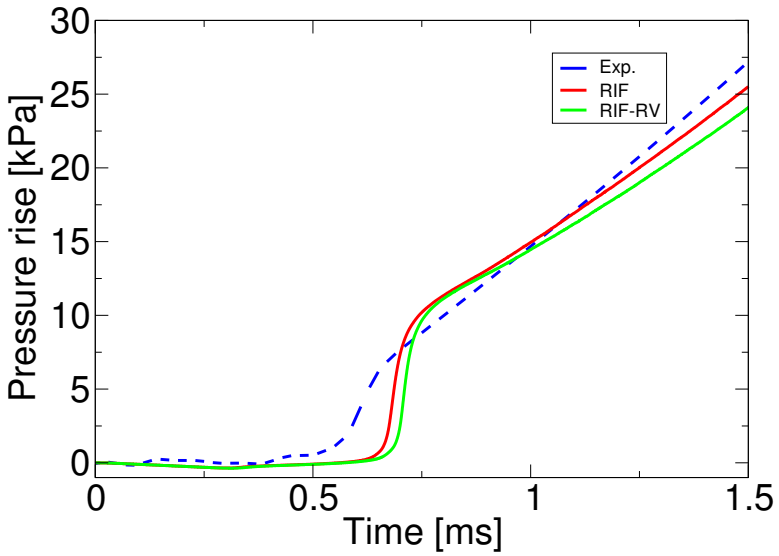

Figure 6.2: comparison between experimental and computed pressure rise with standard RIF and RIF with the Single Droplet model source terms.

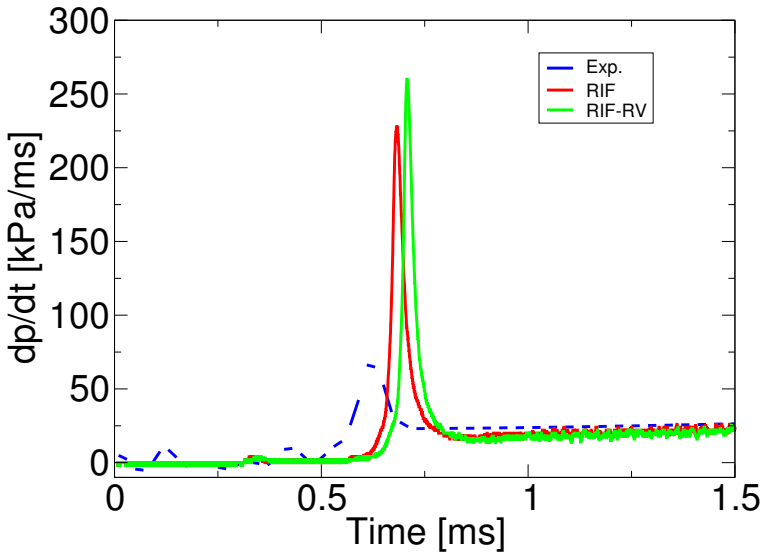

Figure 6.3: comparison between experimental and computed pressure rise derivative versus time with standard RIF and RIF with the Single Droplet model source terms.

intense autoignition. The heat release rate during mixing controlled burn is reproduced quite well and can be considered acceptable.

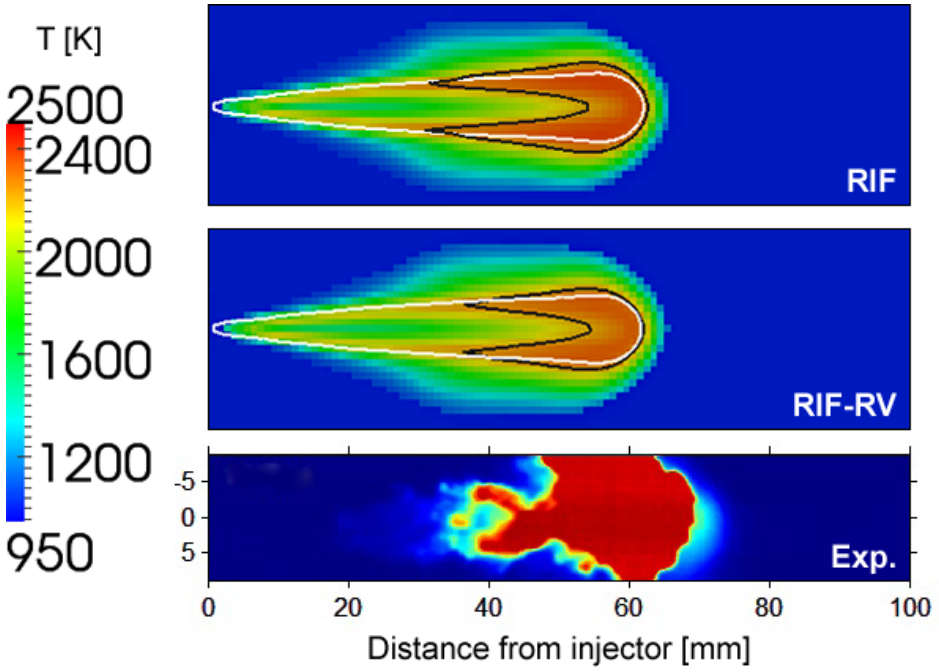

Figure 6.4: comparison among the computed temperature fields at 1.5 ms ASI: the white line represents points at stoichiometric mixture fraction and the black line consists of an iso-contour of 2200 K temperature. Chemiluminescence imaging reproduced from [33].

The computed temperature field is reproduced in figure (6.4). For both the simulations the computed flame results attached to the nozzle. This fact is not encouraging because the RIF model cannot reproduce lifted flames, due to a single one-dimensional flame structure which has to represent the entire physical domain and must ignite at once. In fact the only transported variable related to the flame is the mixture fraction, that accounts for the vapour of fuel present only. The lift-off length measured through the Y_{OH} field results 2 mm for both the simulations, demonstrating the latter consideration. Even if this method is not consistent with the computed flame structure, the lift-off length can be estimated through the temperature field, resulting 31 mm without source terms in the mixture fraction variance equation and 36 mm considering the SDM model, against a measured value of 17 mm.

According to figure (6.4), the computed flames are both dominated by a single diffusive flame, which ranges from the nozzle to the head of the jet. In fact the stoichiometric mixture fraction iso-contour envelopes the entire

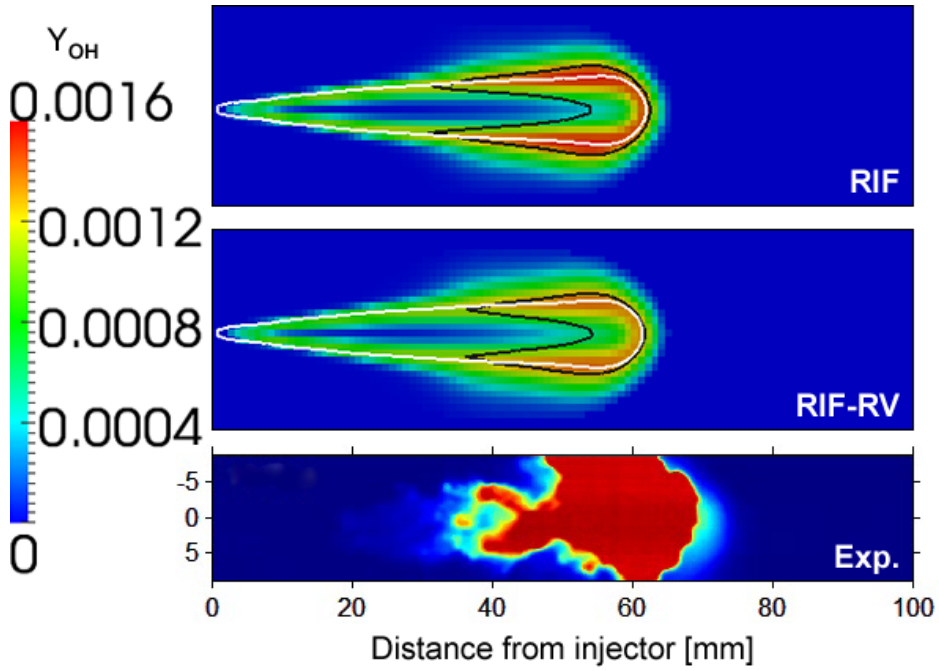

Figure 6.5: comparison among the computed Y_{OH} fields at 1.5 ms ASI: the white line represents points at stoichiometric mixture fraction and the black line consists of an iso-contour of 2200 K temperature. Chemiluminescence imaging reproduced from [33].

jet centreline, showing that all the combustion takes place at stoichiometric conditions. The diffusive flame becomes hotter at the top of the flame, where there are the highest OH concentrations, as can be seen in figure (6.5).

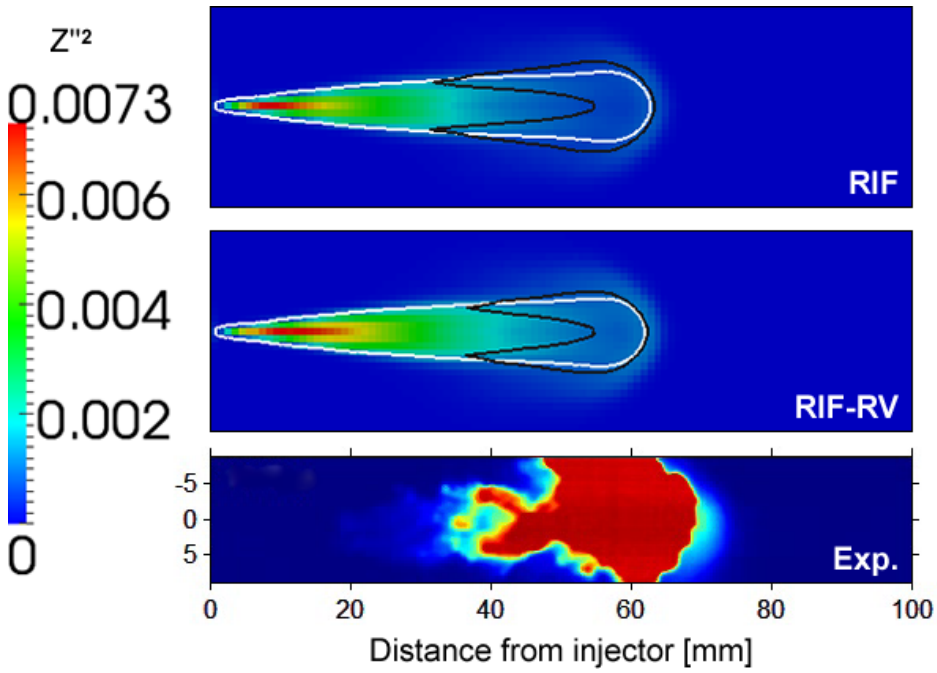

Figure 6.6: comparison among the computed $\widetilde{Z''^2}$ fields at 1.5 ms ASI: the white line represents points at stoichiometric mixture fraction and the black line consists of an iso-contour of 2200 K temperature. Chemiluminescence imaging reproduced from [33].

As shown in figure (6.6), the mixture fraction variance $\widetilde{Z''^2}$ distribution is increased by the SDM model both in the rich premixed flame zone and in the diffusive flame zone, leading to less fuel vapour available for combustion. This fact causes a colder diffusive flame, with a lower pressure rise. Even the longer ignition delay computed with the SDM influence is probably due to an higher mixture fraction variance near the nozzle, resulting in a lack of fuel vapour which makes mixture more difficult to autoignite.

The Single Droplet model derived by Réveillon and Vervisch [43] seems to work by poor agreement with experimental results, since it increases variance near the diffusive flame and causes a longer ignition delay and lift-off length.

The computed flame could be pushed away from the nozzle with a severe increasing of $\widetilde{Z''^2}$ very close to the injector, provided by a closure for the source terms of mixture fraction variance which cannot be neglected, as

discussed in [43]. Hence, the following simulations are carried out using the Single Droplet model.

6.1.2 Influence of the subdivision criterion

In this section the flamelet subdivision criteria presented in (3.2.1) are tested. The simulations involve ten flamelets each, according to the results presented in [2]. Further discussions about the influence of the number of flamelets allowed in the computations will be provided in section (6.1.4).

In order to study only the influence of the subdivision criteria, the interaction among flamelets is neglected. Therefore, flamelets require to be properly initialised, by cloning the new flamelet from the former one, which is:

- the number 1, in case of variance of the scalar dissipation rate subdivision criterion;
- the youngest one, in case of the injected mass subdivision criterion.

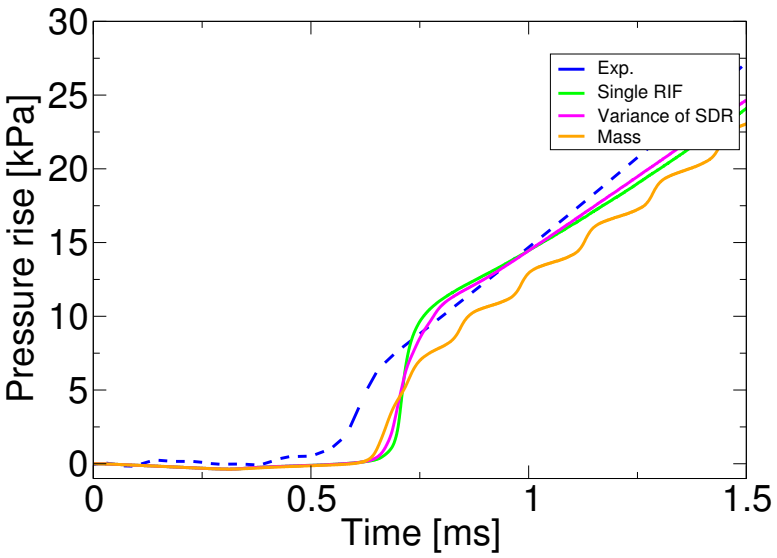

Figure 6.7: comparison between experimental and computed pressure rise with domain subdivision based on the variance of the scalar dissipation rate and on the injected mass.

In figure (6.7) the comparison among the computed pressure rises is shown. Like in the simulations involving only one flamelet, the ignition delay is overestimated again, resulting 0.68 ms in case of the variance of the scalar

dissipation rate subdivision criterion and 0.66 ms in case of the injected mass one. This similarity can be traced back to the simplified chemistry mechanism, which seems to be not very reliable in predicting low temperature combustion.

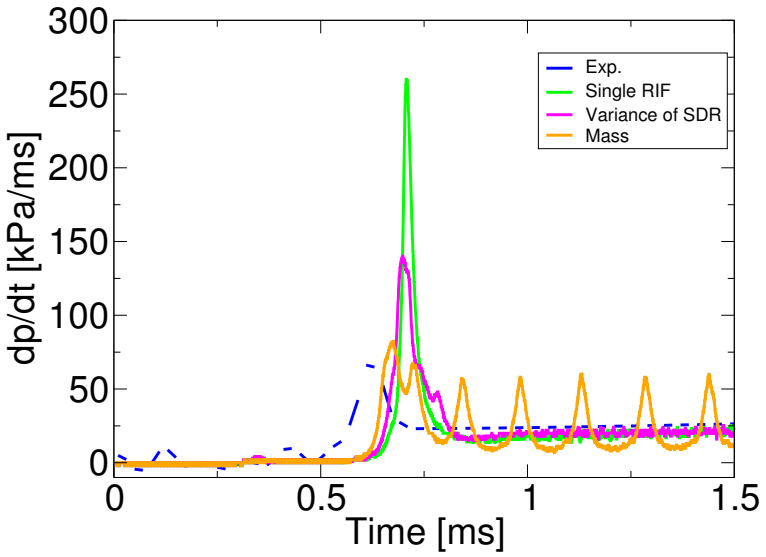

Figure 6.8: comparison between experimental and computed pressure rise derivative versus time with domain subdivision based on the variance of the scalar dissipation rate and on the injected mass.

It is worth noting that the injected mass criterion pressure rise presents several local and smooth oscillations probably due to the ignition of a new flamelet. This observation is confirmed by its derivative versus time, which is depicted in figure (6.8) and presents several periodical peaks.

Involving multiple flamelets provides better results respect to simulations with only one flamelet in terms of heat release rate, which can be qualitatively described by the pressure rise derivative versus time. In fact the two computed peaks present in figure (6.8) are lower than the ones shown in figure (6.3). This is due to the fact that flamelets ignite consecutively [2], which leads to a moderate heat release rate since autoignition does not happen at once. Despite the pressure rise derivative computed with the injected mass subdivision criterion is not physical during the mixing controlled burn, the heat release rate during the premixed burn is very similar to the experimental one, while the one calculated with the variance of the scalar dissipation rate subdivision criterion is heavily overestimated. A possible explanation can be found by comparing figures (6.9) and (6.10).

The mean stoichiometric scalar dissipation rate represents the diffusive

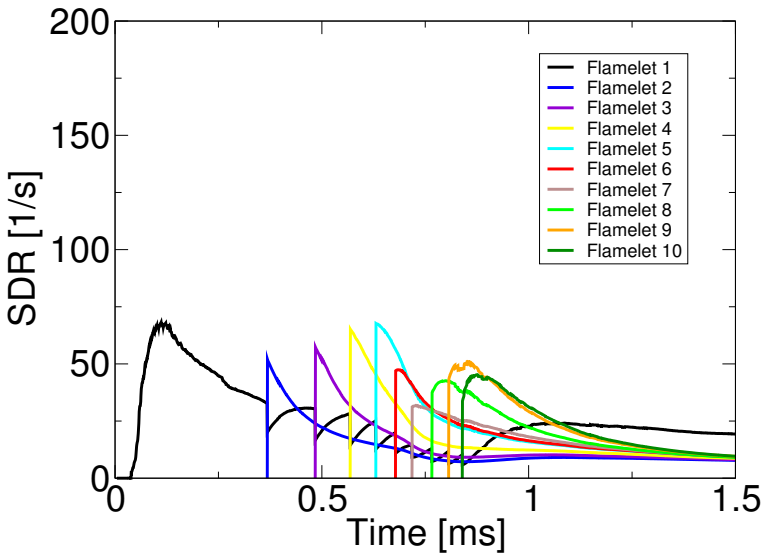

Figure 6.9: mean stoichiometric scalar dissipation rate, variance of scalar dissipation rate subdivision criterion.

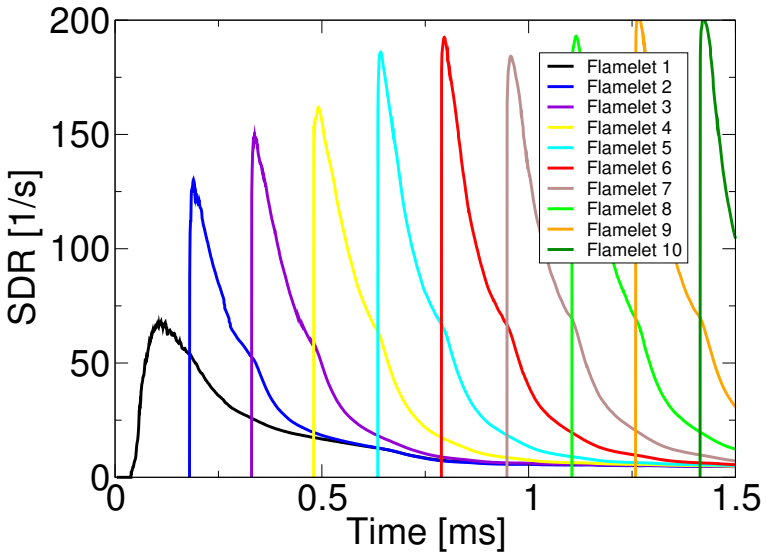

Figure 6.10: mean stoichiometric scalar dissipation rate, injected mass subdivision criterion.

coefficient in the flamelet equations (see equations (2.19) and (2.20)), therefore it controls diffusion of mass and energy in the Z-space. The injected mass subdivision criterion shows a higher mean scalar dissipation rate than the variance of SDR one, leading to an enhanced diffusion of mass and energy resulting in a smoothed autoignition. In the variance of SDR computation, new flamelets have a lower mean stoichiometric scalar dissipation rate, hence more mass and energy can be stored for autoignition.

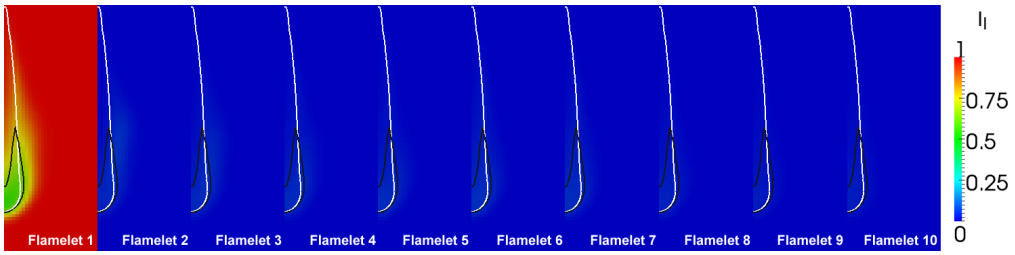

Figure 6.11: flamelet marker particles distributions at 1.5 ms ASI, variance of scalar dissipation rate subdivision criterion.

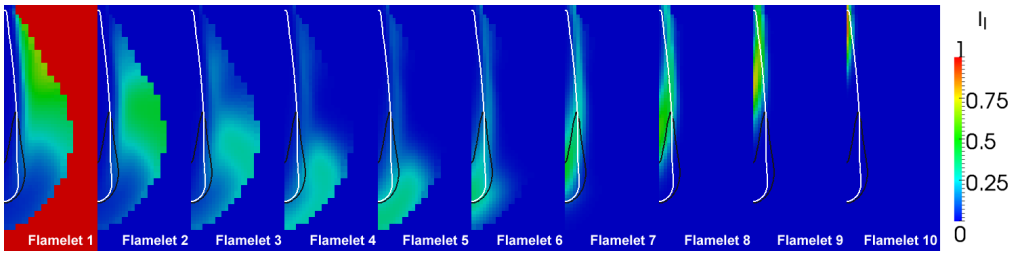

Figure 6.12: flamelet marker particles distributions at 1.5 ms ASI, injected mass subdivision criterion.

The reason of that can be traced back to the marker particle distributions, represented at 1.5 ms ASI in figures (6.11) and (6.12). Figure (6.11) shows that with the variance of the scalar dissipation rate subdivision criterion, new flamelets are almost negligible in the computation, therefore their mass weighted scalar dissipation rate (calculated through equation (3.14)) results reduced. This flamelets distribution makes the simulation carried out with the latter subdivision criterion very similar to the one with only a single flamelet, as proved in figures (6.13) and (6.14), where its computed temperature field and Y_{OH} distribution presents the same features already discussed for the single flamelet computation. Increasing the number of flamelets in such a simulation is therefore retained useless.

The temperature field calculated using the injected mass subdivision criterion, represented in figure (6.13), is encouraging because the flame is no more attached to the nozzle. This is due to the flamelet distribution shown in figure (6.12), where the youngest flamelets, related to the latest injected mass, are located very close to the injector. These flamelets present a high mean stoichiometric scalar dissipation rate (see figure (6.10)) and need quite a lot of time to ignite, preventing the flame to come close to the nozzle.

While the temperature field provides a lift-off length equal to 32 mm, the one calculated through to the Y_{OH} distribution results 7 mm, showing how increasing the number of flamlets in the computation according to the injected mass criterion could allow to achieve a lifted flame. Also the flame structure can be carried out from the Y_{OH} field depicted in figure (6.14). Going downstream from the injector, a rich premixed combustion takes place in the first part of the flame alongside the liquid spray, where the 'child' flamelets 8, 9 and 10 are not yet ignited and the 'senior' flamelets 1 and 2 govern the process. Diffusive combustion characterizes the leading part of the flame, involving only 'adult' flamelets (3, 4, 5, 6 and 7) and enveloping the so called 'head vortex'.

6.1.3 Influence of flamelet interaction

In this section the influence of interaction among flamelets on the simulations is investigated, comparing results carried out without interaction and with the two interaction models previously discussed in section (3.2.2). The simulations involve ten flamelets each and, in order to emphasize the interaction between young flamelets and old flamelets, the new flamelets are initialised according to the conditions present at the beginning of the simulation. In this way, the ignition of 'child' flamelets is caused by 'adult' flamelets, which provide them energy and mass.

The flamelet interaction effect is studied distinguishing the subdivision criterion adopted.

Injected mass subdivision criterion

The two interaction models previously discussed do not provide encouraging results, mainly in terms of flame structure: in fact, the interaction among flamelets leads again the flame to be attached to the nozzle and to be dominated by diffusive combustion, which takes place from the injector tip to the head of the jet. As can be seen in figure (6.15), the better one in terms of pressure rise seems to be the Attack interaction model, which removes the

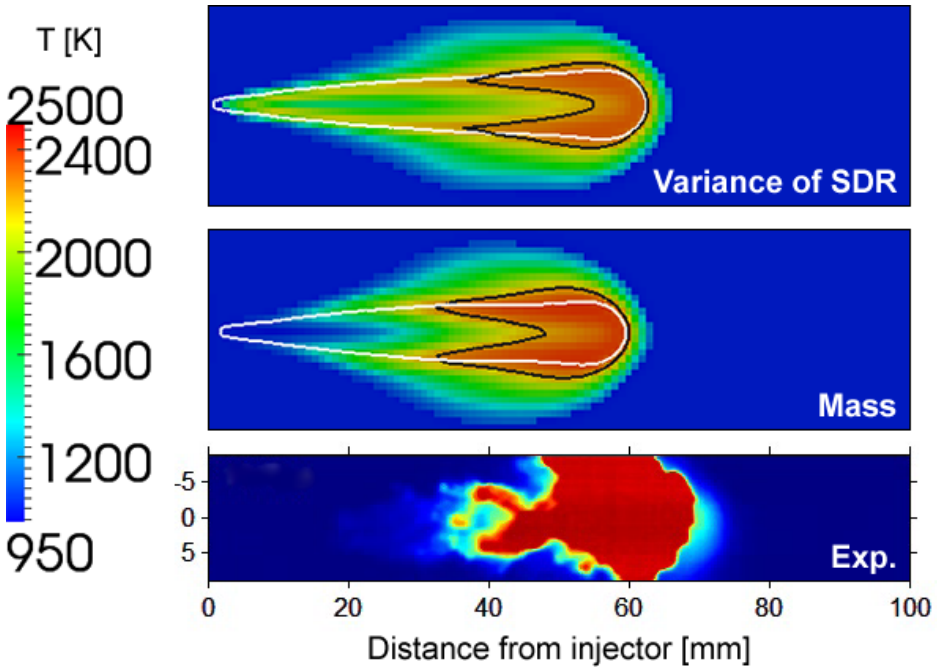

Figure 6.13: comparison among the computed temperature fields at 1.5 ms ASI: the white line represents points at stoichiometric mixture fraction and the black line consists of an iso-contour of 2200 K temperature. Chemiluminescence imaging reproduced from [33].

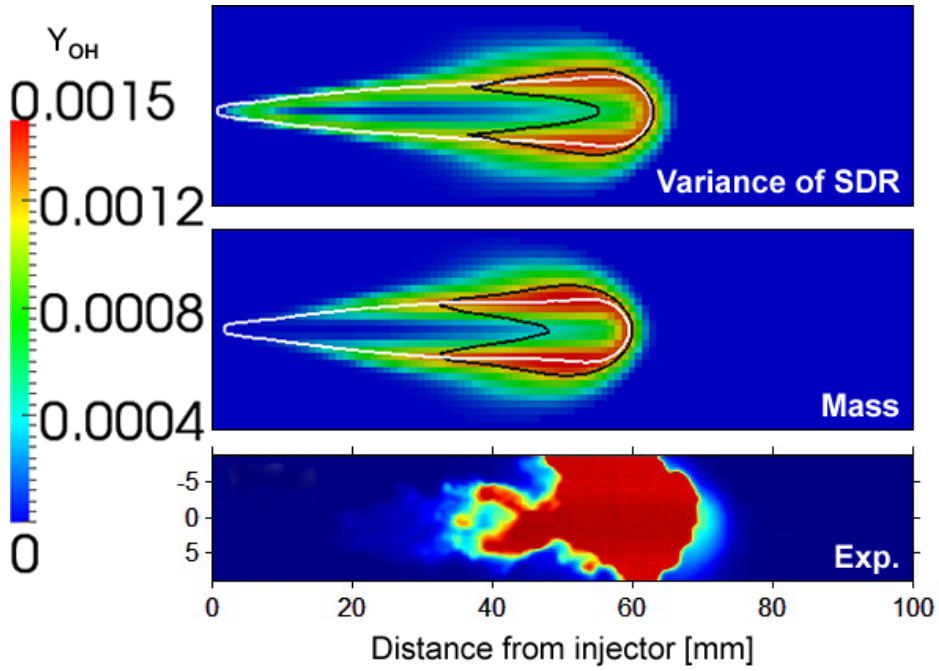

Figure 6.14: comparison among the computed Y_{OH} fields at 1.5 ms ASI: the white line represents points at stoichiometric mixture fraction and the black line consists of an iso-contour of 2200 K temperature. Chemiluminescence imaging reproduced from [33].

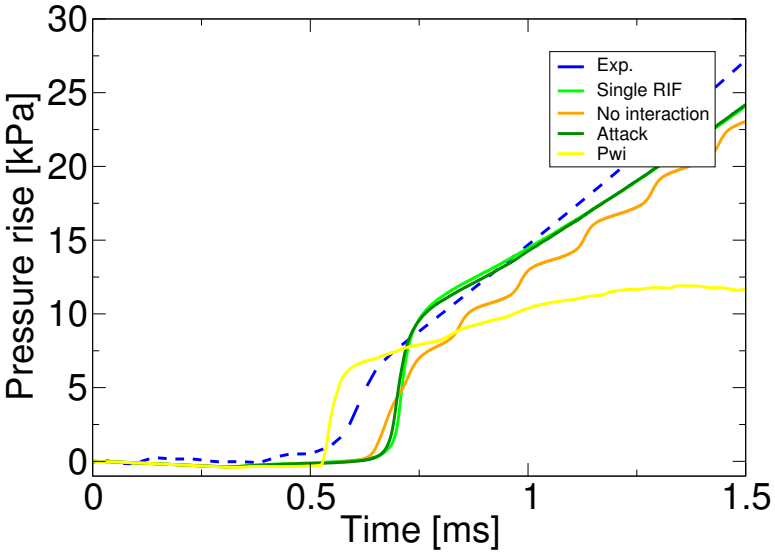

Figure 6.15: comparison between experimental and computed pressure rise neglecting flamelet interaction, with the Attack flamelet interaction model and with the Pwi flamelet interaction model. The domain is subdivided according to the injected mass criterion.

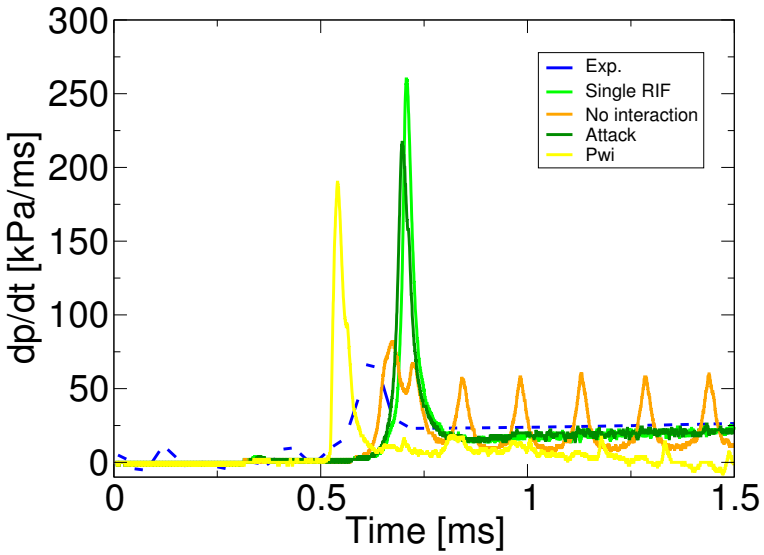

Figure 6.16: comparison between experimental and computed pressure rise derivative versus time neglecting flamelet interaction, with the Attack flamelet interaction model and with the Pwi flamelet interaction model. The domain is subdivided according to the injected mass criterion.

periodical oscillations due to the suddenly ignition of new injected flamelets, already noted in the previous section.

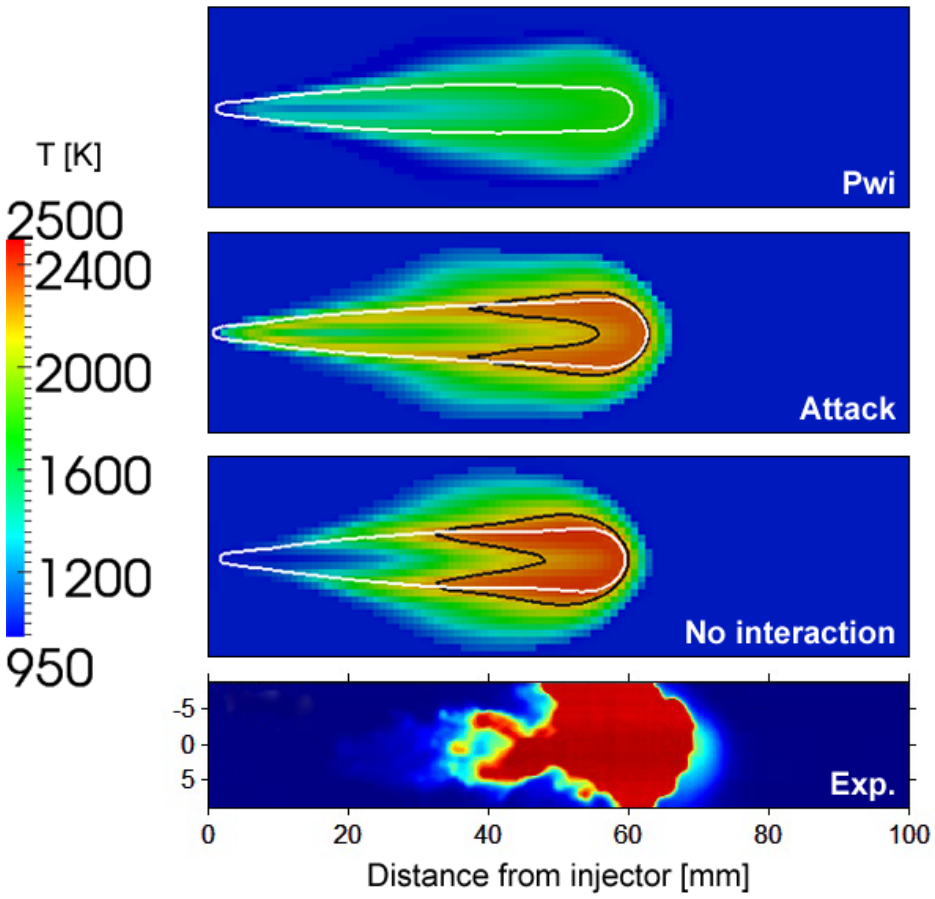

Figure 6.17: comparison among the computed temperature fields at 1.5 ms ASI: the white line represents points at stoichiometric mixture fraction and the black line consists of an iso-contour of 2200 K temperature. The domain is subdivided according to the injected mass criterion. Chemiluminescence imaging reproduced from [33].

The computed temperature field at 1.5 ms ASI represented in figure (6.17) results very similar to the one calculated with only one flamelet, showing that the interaction computed by the Attack model privileges the flamelet number 1, which owns the entire computational domain at the beginning of the simulation. In fact as a new flamelet is introduced in the domain, it is immediately attacked by the leader flamelet 1 which makes the young flamelet identical, in terms of mass fraction and enthalpy, to itself. This makes all the

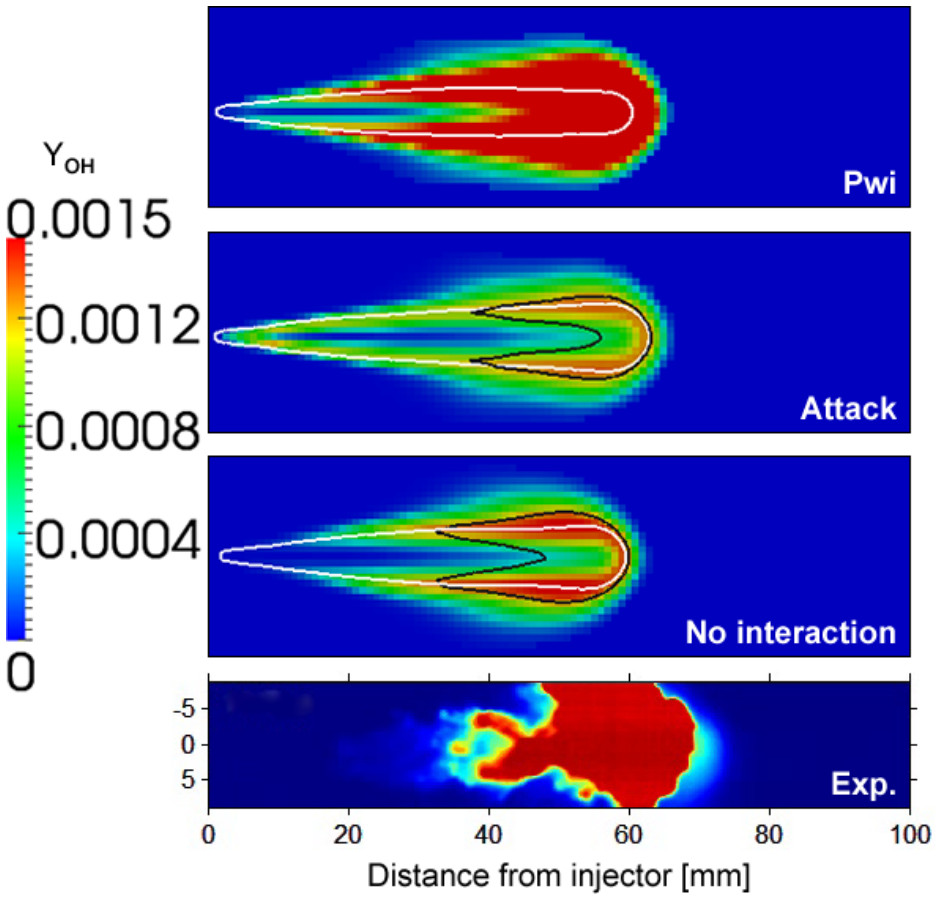

Figure 6.18: comparison among the computed Y_{OH} fields at 1.5 ms ASI: the white line represents points at stoichiometric mixture fraction and the black line consists of an iso-contour of 2200 K temperature. The domain is subdivided according to the injected mass criterion. Chemiluminescence imaging reproduced from [33].

four flamelets present in the domain at 0.69 ms (see figure (6.10)) to ignite at once, leading to the overestimated peak in the pressure rise derivative versus time depicted in figure (6.16) and already discussed for the single flamelet computation.

The PDF-weighted interaction model underestimates the ignition delay, which results 0.53 ms. This model does not provide encouraging results in these simulations, because, despite the auto-ignition of flamelets happens before than usual, the heat release rate is overestimated, like shown in figure (6.16). This is probably due to the leading flamelet 1, which provides mass and energy to the just introduced flamelets, making them ignite at once. The ignition happens earlier because these young flamelet grow faster due to their PDF which is made older by the one of the leading flamelet. Unfortunately, when the mixing controlled burn takes place, the heat release rate is decreased by the new not ignited flamelets, which make the already ignited flamelets younger by altering their PDF. This leads to an underestimated heat release which prevents pressure rise to increase.

The flame structure carried out from the latter simulation is depicted in the box marked with the 'Pwi' label in figure (6.17), in terms of temperature field, and in figure (6.18), in terms of OH species distribution. The estimated flame results colder than the other ones and the leading vortex is completely involved in a diffusive flame, according to the OH distribution. In this flame it is not possible to measure the lift-off length according to the temperature field, because the maximum temperature is severely underestimated and is lower than 2200 K. Anyway, the OH species distribution provides a value of 3 mm.

Variance of SDR subdivision criterion

Introducing flamelets interaction in the simulations where the domain is subdivided according to the variance of SDR criterion produces different effects depending on the model considered.

Like can be seen in figures (6.21) and (6.22), the Attack interaction model does not alter the flame structure, which is almost equal to the one computed neglecting interaction, with the flame attached to the nozzle again. The pressure rise, in figure (6.19), and the heat release rate, in figure (6.20), are slightly modified: the ignition delay is a bit longer than the one estimated without interaction, resulting 0.71 ms and leading to a higher heat release rate.

Despite new flamelets seems to be not much important in the simulation, the Pwi interaction model severely alters the results. In fact autoignition happens later than usual at about 0.81 ms, leading to a very large heat release

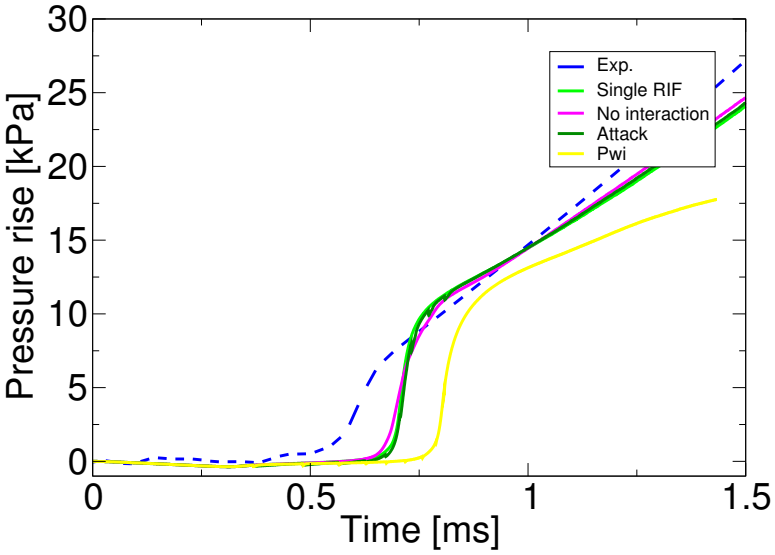

Figure 6.19: comparison between experimental and computed pressure rise neglecting flamelet interaction, with the Attack flamelet interaction model and with the Pwi flamelet interaction model. The domain is subdivided according to the variance of SDR criterion.

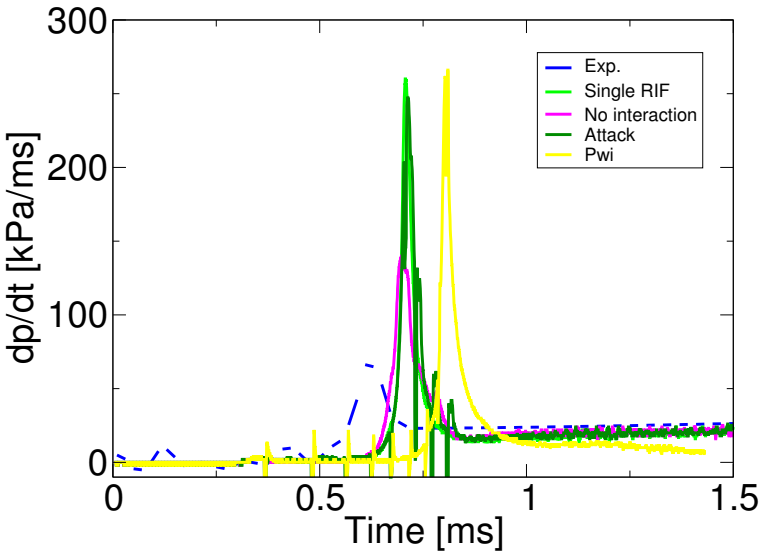

Figure 6.20: comparison between experimental and computed pressure rise derivative versus time neglecting flamelet interaction, with the Attack flamelet interaction model and with the Pwi flamelet interaction model. The domain is subdivided according to the variance of SDR criterion.

during premixed burn. During mixing controlled combustion the heat release is underestimated, maybe because the model alters the PDF of the ignited flamelets. This fact makes decrease the temperature of the diffusive flame and the OH species mass fraction distribution.

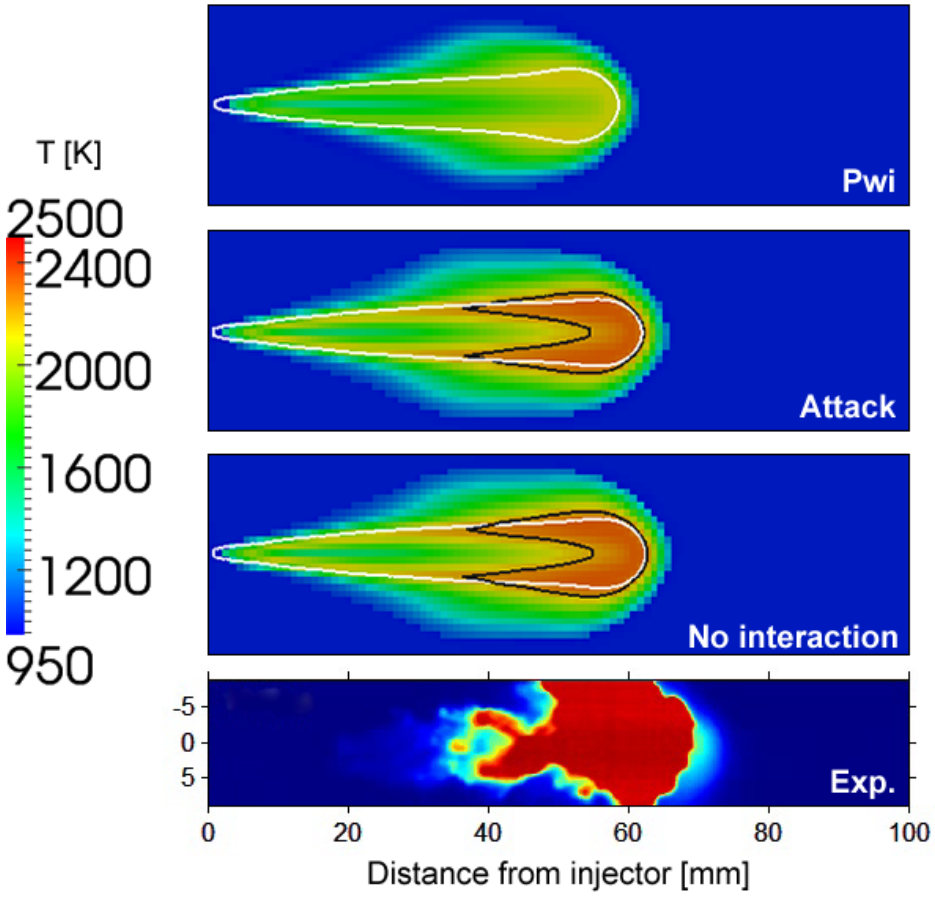

Figure 6.21: comparison among the computed temperature fields at 1.5 ms ASI: the white line represents points at stoichiometric mixture fraction and the black line consists of an iso-contour of 2200 K temperature. The domain is subdivided according to the variance of SDR criterion. Chemiluminescence imaging reproduced from [33].

6.1.4 Influence of the number of flamelets

In this section the influence of the number of flamelets on the computation is investigated. As can be seen in figure (6.11), increasing the number of

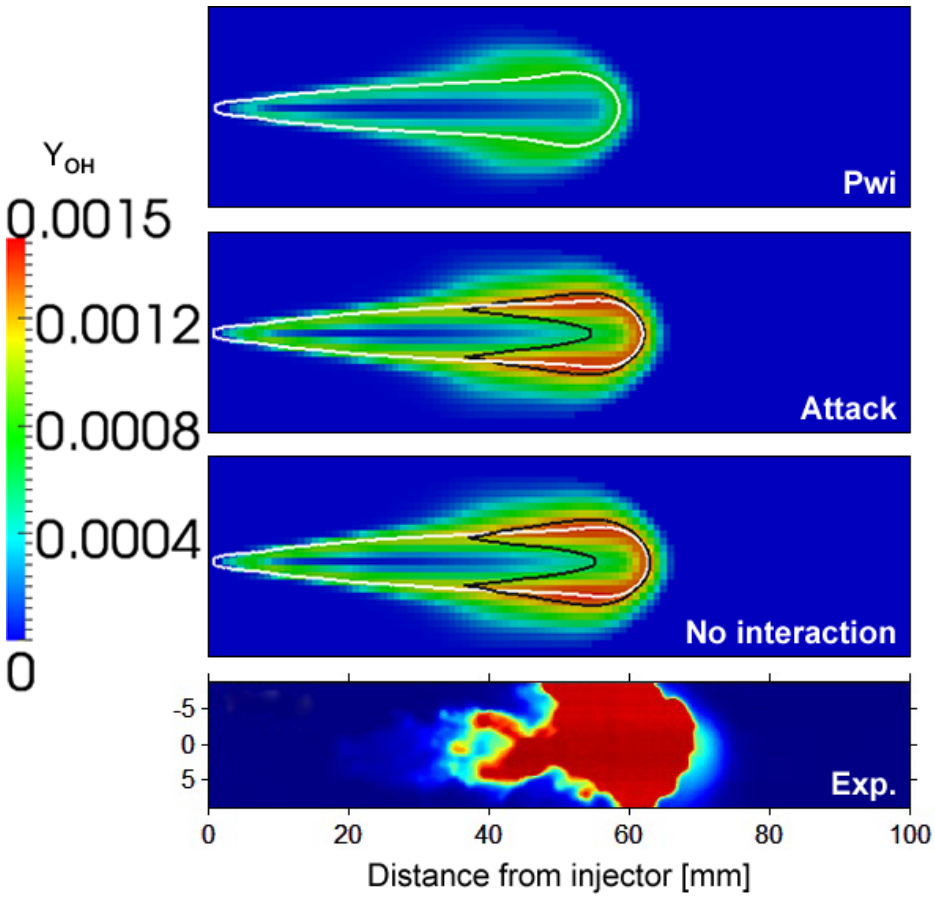

Figure 6.22: comparison among the computed Y_{OH} fields at 1.5 ms ASI: the white line represents points at stoichiometric mixture fraction and the black line consists of an iso-contour of 2200 K temperature. The domain is subdivided according to the variance of SDR criterion. Chemiluminescence imaging reproduced from [33].

flamelets allowed for the simulation is useless when the domain is subdivided according to the variance of the scalar dissipation rate. Therefore, the investigation is carried out only for the simulations that use the injected mass subdivision criterion. Interaction among flamelets is neglected, in order to avoid the already discussed dominance of the first flamelet.

Flamelets	Exp.	1	5	10	20	30
Lift-off [mm]	17	2	6	7	7	7
Ignition delay [ms]	0.63	0.70	0.65	0.66	0.66	0.66

Table 6.2: influence of the number of flamelets on the lift-off length and on the ignition delay. The lift-off length is measured according to the OH mass fraction distribution.

The computed pressure rise is shown in figure (6.23) varying the number of flamelets involved in the simulations. As can be noted, increasing the number of flamelets does not affect the ignition delay, which remains almost the same (see table (6.2)) for multiple flamelets simulations. The local oscillations in the pressure rise curves result smoothed with more flamelets, approximately disappearing using 30 flamelets. This is due to the smaller amount of mass enclosed in each flamelet, leading to a smaller energy release when it ignites.

The pressure rise dirivative versus time is depicted in figure (6.24). Increasing the number of flamelets allows to reduce the heat release during autoignition, showing rather good agreement with the measured one when using 30 flamelets. Despite local oscillations are no more visible in figure (6.23) for the latter simulation, the pressure rise derivative is again slightly perturbed by flamelet ignition during the mixing controlled burn, showing smaller but clear peaks of heat release.

Figures (6.25) and (6.26) show the temperature field and the Y_{OH} field respectively. Using multiple flamelets allows the flame to detach from the nozzle, increasing the lift-off length measured according to the OH mass fraction distribution. As reported in table (6.2), 5 flamelets are enough to reach an acceptable lift-off length, which does not increase very much with the number of flamelets, leading to a measured lift-off length which remains the same involving 10, 20 and 30 flamelets.

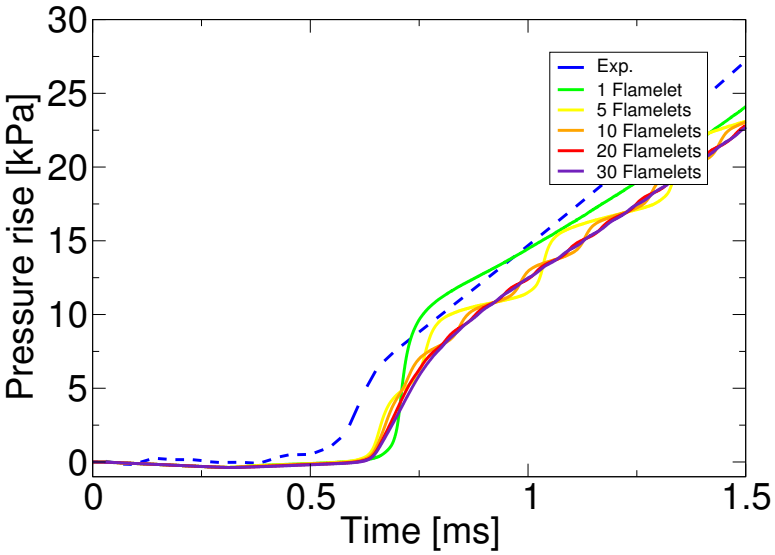

Figure 6.23: comparison between experimental and computed pressure rise varying the number of flamelets. The domain is subdivided according to the injected mass criterion and flamelet interaction is neglected.

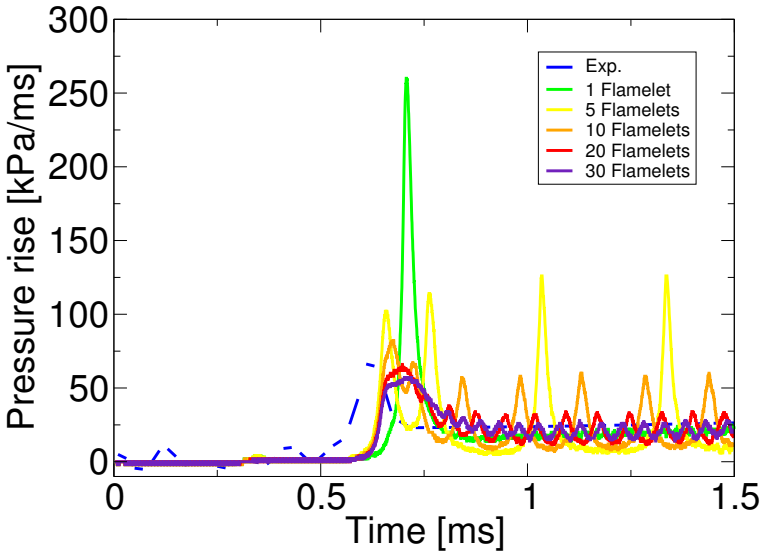

Figure 6.24: comparison between experimental and computed pressure rise derivative versus time varying the number of flamelets. The domain is subdivided according to the injected mass criterion and flamelet interaction is neglected.

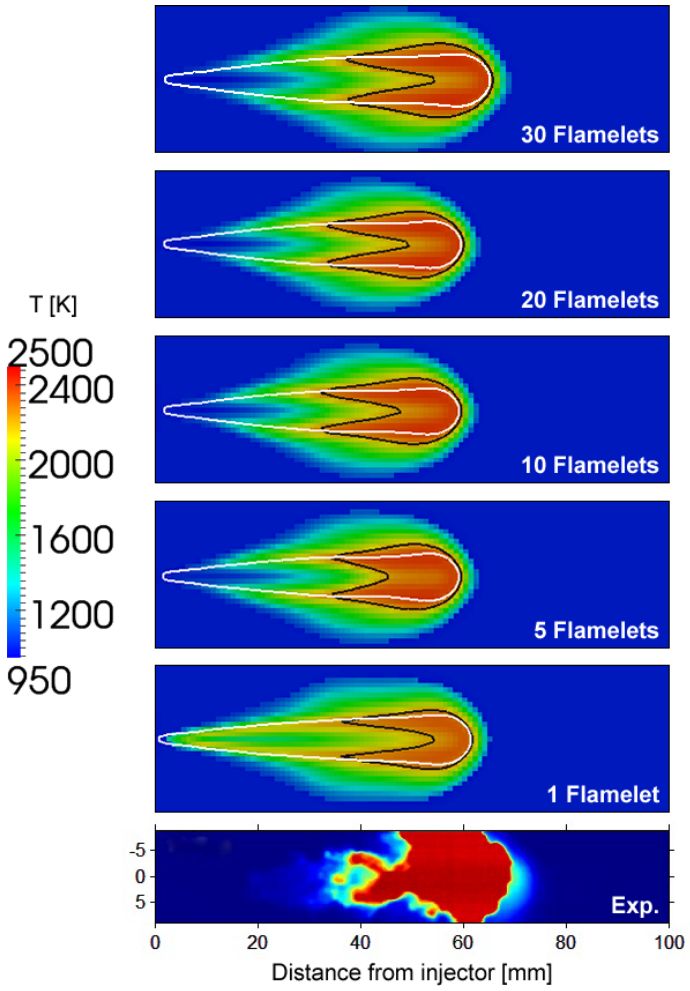

Figure 6.25: comparison among the computed temperature fields at 1.5 ms ASI varying the number of flamelets: the white line represents points at stoichiometric mixture fraction and the black line consists of an iso-contour of 2200 K temperature. The domain is subdivided according to the injected mass criterion and flamelet interaction is neglected. Chemiluminescence imaging reproduced from [33].

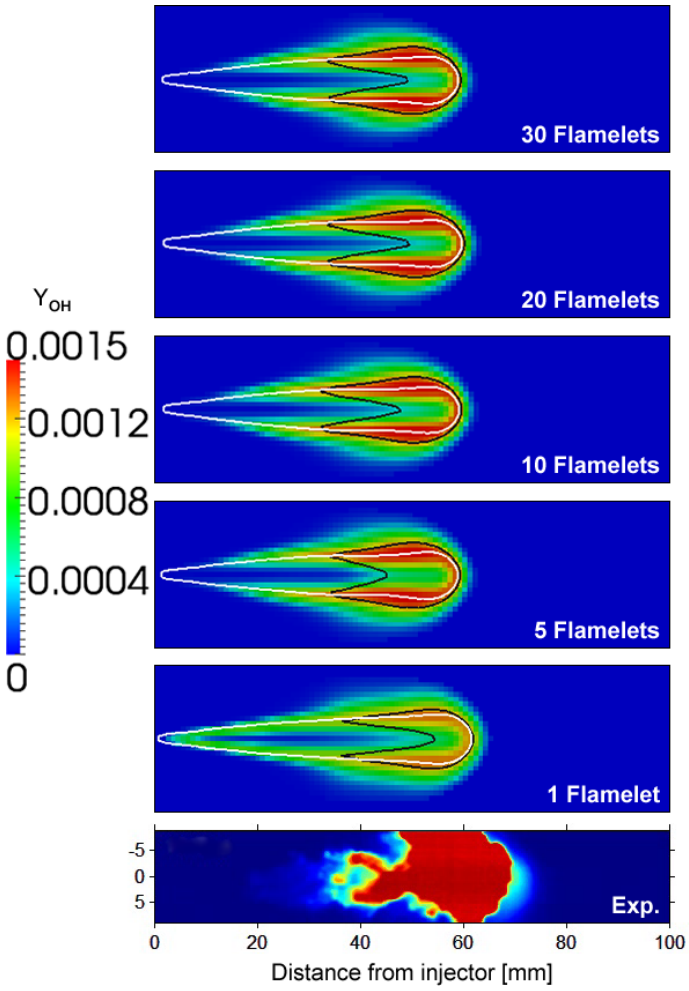

Figure 6.26: comparison among the computed Y_{OH} fields at 1.5 ms ASI varying the number of flamelets: the white line represents points at stoichiometric mixture fraction and the black line consists of an iso-contour of 2200 K temperature. The domain is subdivided according to the injected mass criterion and flamelet interaction is neglected. Chemiluminescence imaging reproduced from [33].

6.2 Simulation of soot precursors

Despite models for predicting the soot emissions were not implemented in the CFD solvers developed in this study, it is possible to discuss the computed distributions of formaldehyde (CH_2O) and acetylene (C_2H_2), which can be considered, according to [10], as soot inception species. The species distribution calculated during the previously described simulations are compared to the experimental data provided by Idicheria and Pickett in [17]. In their work, they investigated the cool flame near the lift-off length well after the time of ignition, by using Planar Laser Induced Fluorescence of formaldehyde[1], for different soot levels in a n-heptane fuel jet evolving in the SNL vessel. Since the formaldehyde PLIF is strongly modified by the Polycyclic Aromatic Hydrocarbons fluorescence, the two different sources are not distinguished in the provided experimental images.

In this study, the comparisons between computed and measured soot inception species are carried out for moderate-soot conditions, summarized in table (6.1).

According to [10], formaldehyde is formed in the cool flame region, and then is consumed in the high-temperature reaction zone, where PAHs and soot form. In order to allow formaldehyde to form, both high mixture temperature and sufficient time for the mixture to react are needed. The latter condition depends on the reaction rate, resulting from the ambient oxygen concetration. Once formed, formaldehyde moves towards the high-temperature reaction zone and is consumed in a region downstream the lift-off length. This fact confirms the fuel-rich high-temperature premixed reaction zone described in the conceptual model presented in section (1.1).

For moderate-soot conditions, the experimental images reproduced from [17] in figures (6.27) and (6.28) lead to some general considerations. Firstly, the axial distance of first formaldehyde formation is coincident with the lift-off length. Then, the region of formaldehyde consumption corresponds to the region of high-temperature combustion. Finally, formaldehyde and PAHs coexist in the fuel-rich premixed reaction zone, also indicated by a thinning of formaldehyde at the jet center.

The computed Y_{CH_2O} and $Y_{C_2H_2}$ are shown in figures (6.27) and (6.28) respectively, where the ranges of the species distributions are chosen according to [10]. As can be seen, the most encouraging results are provided by the simulation carried out with the injected mass subdivision criterion and neglecting flamelet interaction.

The normalized distributions of formaldehyde and acetylene along the

[1] See [17] for further details about the experimental set-up.

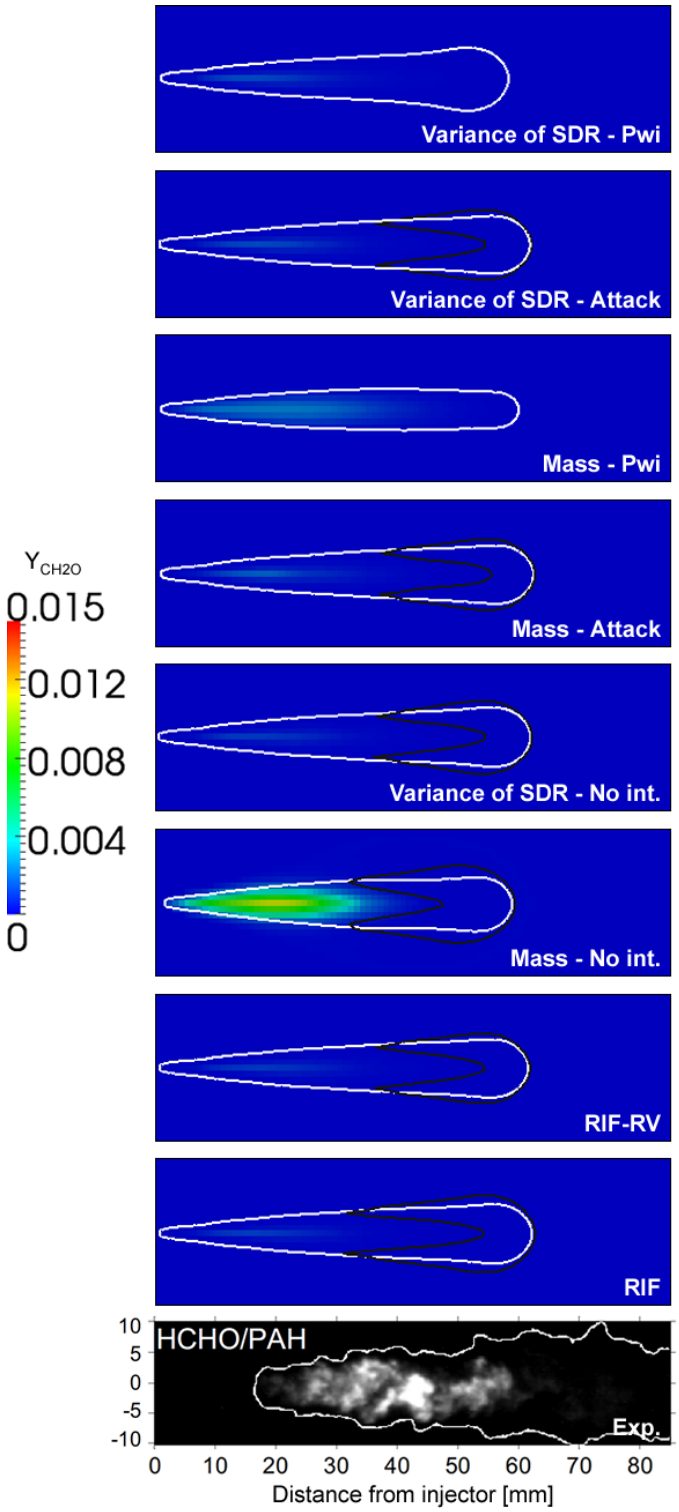

Figure 6.27: comparison among the computed Y_{CH_2O} fields at 1.5 ms ASI: the white line represents points at stoichiometric mixture fraction and the black line consists of an iso-contour of 2200 K temperature. PLIF imaging reproduced from [17].

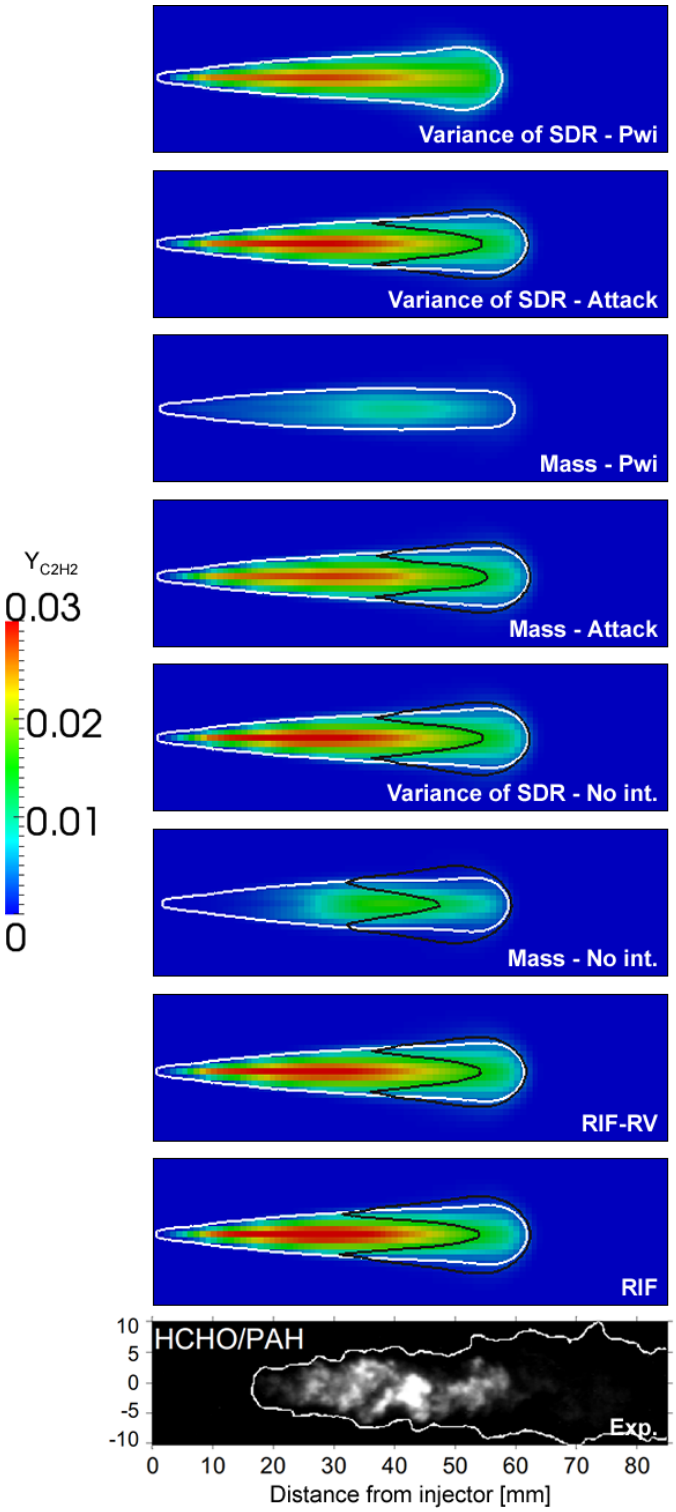

Figure 6.28: comparison among the computed $Y_{C_2H_2}$ fields at 1.5 ms ASI: the white line represents points at stoichiometric mixture fraction and the black line consists of an iso-contour of 2200 K temperature. PLIF imaging reproduced from [17].

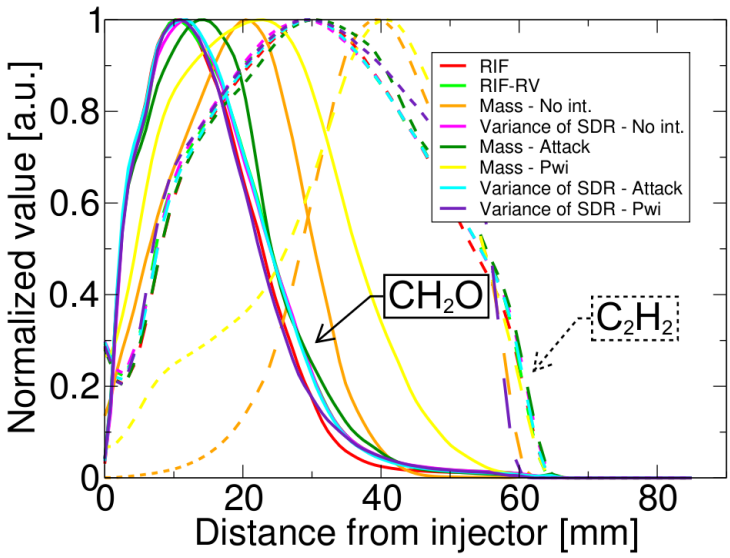

Figure 6.29: comparison between computed Y_{CH_2O} and $Y_{C_2H_2}$ distributions along the spray axis. Each species is normalized by its maximum value along the axis. Straight lines indicate the Y_{CH_2O} distributions and dashed lines indicate the $Y_{C_2H_2}$ distributions.

spray axis are depicted in figure (6.29), in order to discover both the regions of formation and consumption and an eventual overlap. Despite the severe underestimation of formaldehyde production, all the tested models correctly predict the axial location of formaldehyde production (at the lift-off length) and its fast consumption when proceeding towards the high-temperature combustion zone. Acetylene is present very close to the injector, probably due to the wrong flame structure, which is attached to the nozzle. Despite this mistake, the formaldehyde and acetylene distributions overlap, showing good agreement with the experimental images.

Despite the smaller overlap, the most reliable computed distributions seems to be the ones carried out with the injected mass subdivision criterion neglecting flamelet interaction, depicted in figure (6.29) with orange lines. In fact, the formaldehyde (straight line) production zone is shifted downstream due to the computed lifted flame and acetylene (dashed line) is present only in the high-temperature reaction zone, where PAHs and soot form and formaldehyde is completely consumed.

6.3 Influence of ambient conditions

In this section the influence of the ambient conditions is investigated in terms of initial vessel temperature, gas density and oxygen concentration. The simulations were carried out subdividing the domain according to the injected mass criterion and neglecting flamelet interaction: such a configuration is the only one providing an acceptable lift-off length and heat release rate, which are very important for the model validation. The considerations reported in section (6.1.4) allow to retain that ten flamelets are enough to provide reliable results.

6.3.1 Initial vessel temperature

The influence of the initial vessel temperature is studied for four different cases, which are summarized in table (6.3).

O_2 mole fraction [%]	Ambient temp. [K]	Ambient density [kg/m^3]	Ambient pressure [MPa]	Injected mass [mg]	Lift-off length [mm]	Ignition delay [ms]
21	850	14.8	3.58	17.6	30.1	1.12
21	900	14.8	3.79	17.5	25.5	0.88
21	1000	14.8	4.21	17.8	17.0	0.63
21	1300	14.8	5.48	17.4	7.7	0.36

Table 6.3: cases set-up: influence of the initial vessel temperature.

The pressure rise and its derivative versus time are depicted in figures (6.30) and (6.31) respectively, while the ignition delay and the lift-off length are shown in figure (6.32).

The model seems to overestimate the heat release rate during autoignition, especially in the case of 1300 K initial temperature. The very high temperature of the vessel causes the fuel to ignite immediately as soon as it gets into the combustion chamber. This makes multiple flamelets useless, because the simulation presents the same drawbacks found with only one flamelet. In fact the computed pressure rise does not illustrate the local growth usually present with multiple flamelets and the flame is attached to the nozzle, as can be deduced from the computed lift-off length, which is very small in the latter case. This fact explains how the model reproduces a lifted flame:

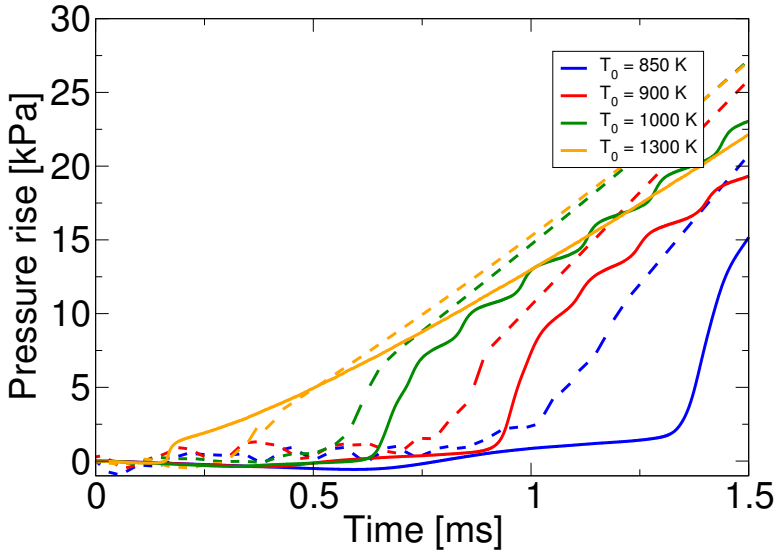

Figure 6.30: comparison between experimental (dashed lines) and computed (straight lines) pressure rise varying the initial vessel temperature. The domain is subdivided according to the injected mass criterion and flamelet interaction is neglected.

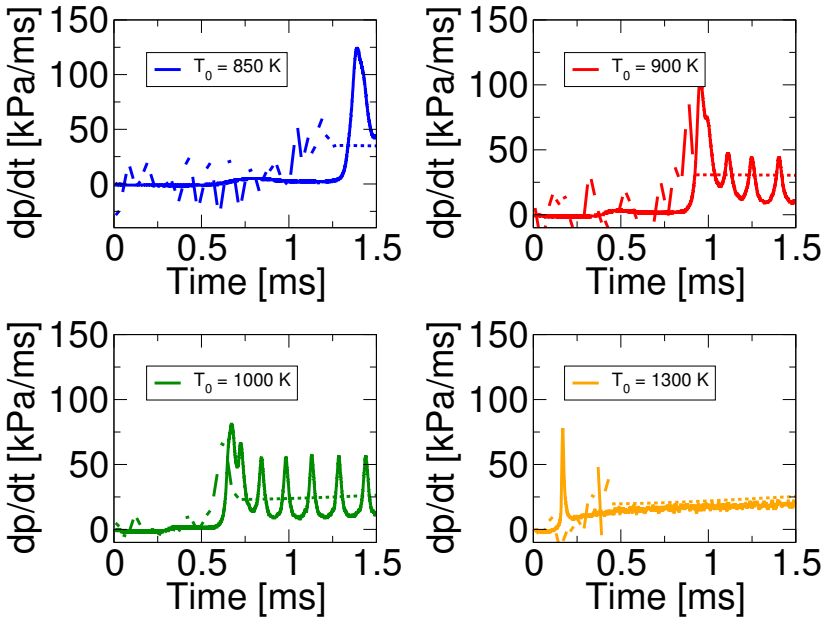

Figure 6.31: comparison between experimental (dashed lines) and computed (straight lines) pressure rise derivative versus time varying the initial vessel temperature. The domain is subdivided according to the injected mass criterion and flamelet interaction is neglected.

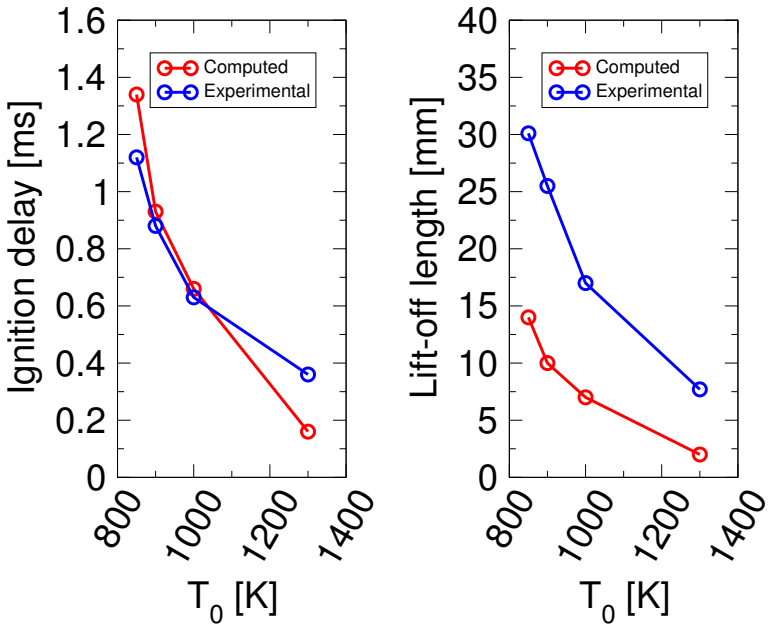

Figure 6.32: comparison between experimental and computed ignition delay and lift-off length varying the initial vessel temperature. The domain is subdivided according to the injected mass criterion and flamelet interaction is neglected.

the flamelet is kept away from the nozzle only by the youngest flamelets, which usually need some time for autoignition, happening downstream and leading to a lifted flame. In this case the high temperature speeds up the flamelets ignition, showing how the simulated mechanism does not reproduce the real physical process, even if the results are in acceptable agreement with experimental data.

The computed heat release rate during the mixing-controlled phase is underestimated when the initial temperature is 1300 K, while in the other cases the results are very similar to the measured values.

Despite the computed lift-off length is underestimated (as already discussed in the previous sections), the model is able to reproduce the trend shown during the experiments, where the lift-off length decreases as the initial vessel temperature increases. The same can be seen for the ignition delay: the model correctly predicts the trend of the time required for autoignition, showing encouraging results.

The computed ignition delay significantly differs from the measured one both in case of very high vessel temperature (1300 K), where it is underestimated, and in case of very low vessel temperature (850 K), where it is

overestimated. This fact is probably due to the simplified chemistry mechanism, which was validated only in a relatively narrow range of temperatures.

In figures (6.33), (6.34) and (6.35) a comparison between the computed formaldehyde and acetylene distributions and the measured ones provided by [17] is shown for no-soot conditions, low-soot conditions and moderate-soot conditions. According to [17], different soot conditions can be reached changing the initial vessel temperature and keeping constant the inital oxygen molar fraction.

As it can be seen the computed distributions are in rather good agreement with the PLIF images for all the three soot conditions.

In case of no-soot conditions, the formaldehyde is present upstream of the lift-off length, as a result of low-temperature reactions, which generate a first-stage cool-flame. Proceeding downstream towards the head of the jet and beyond the lift-off length, formaldehyde is consumed through high-temperature reactions happening between the high-temperature products coming from the diffusion flame and the fuel-rich reactants present at the jet centre. The presence of this fuel-rich, high-temperature premixed reaction zone is consistent with the conceptual model described in section (1.1).

In case of low-soot conditions, the experimental image shows two different

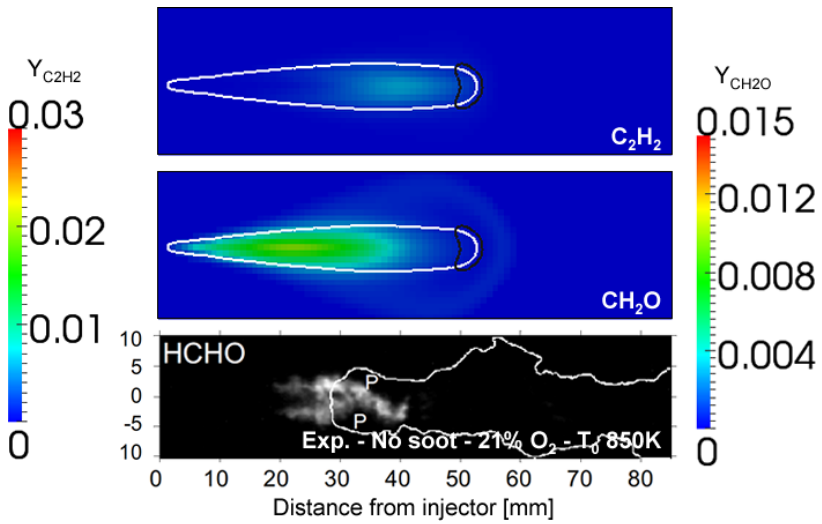

Figure 6.33: $Y_{C_2H_2}$ field and Y_{CH_2O} field at 1.5 ms ASI, comparison between experimental and computed distributions for no-soot conditions: the white line represents points at stoichiometric mixture fraction and the black line consists of an iso-contour of 2200 K temperature. PLIF imaging reproduced from [17].

signals: the one upstream of the lift-off length is generated by formaldehyde, indicating a cool-flame region. Shortly downstream of the lift-off length the signal disappears, since formaldehyde is consumed generating a high-temperature reaction zone. The LIF signal reappears slightly downstream, this time produced by the presence of PAHs. As can be seen the computed formaldehyde and acetylene distributions are again in good agreement with the experimental images.

For moderate-soot conditions, the formaldehyde distribution is completely enclosed in the high-temperature reaction zone. In the experimental images formaldehyde and PAHs are not very distinct, but, according to the previous considerations, the upstream signal can be reasonably attributed to formaldehyde, while the downstream one to acetylene. The computed distributions confirm the latter considerations, also considering that the lift-off length is severely underestimated and equal to 7 mm.

Figure (6.36) shows the computed distributions of Y_{CH_2O} and $Y_{C_2H_2}$ along the spray axis for the three different soot conditions previously discussed. The computed formaldehyde is present in the first part of the flame and is consumed in the high-temperature reaction zone. With the increasing of the initial vessel temperature the lift-off length decreases and the formaldehyde distribution moves upstream towards the nozzle. Acetylene is present only

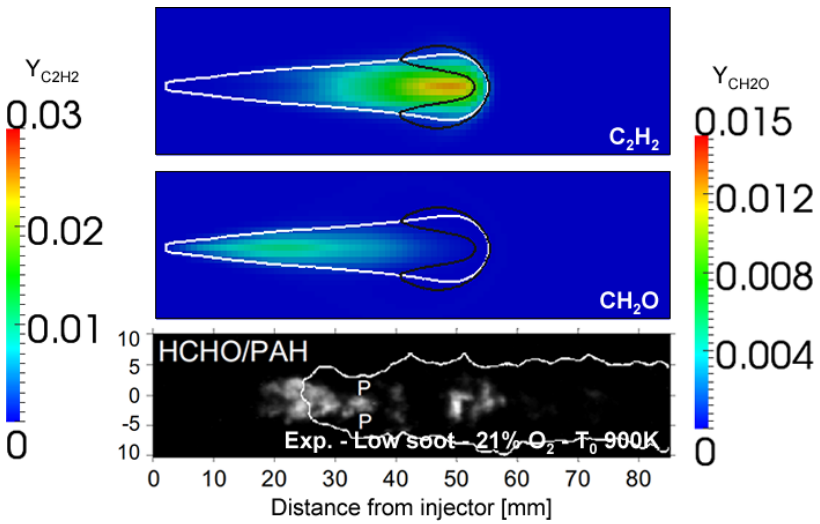

Figure 6.34: $Y_{C_2H_2}$ field and Y_{CH_2O} field at 1.5 ms ASI, comparison between experimental and computed distributions for low-soot conditions: the white line represents points at stoichiometric mixture fraction and the black line consists of an iso-contour of 2200 K temperature. PLIF imaging reproduced from [17].

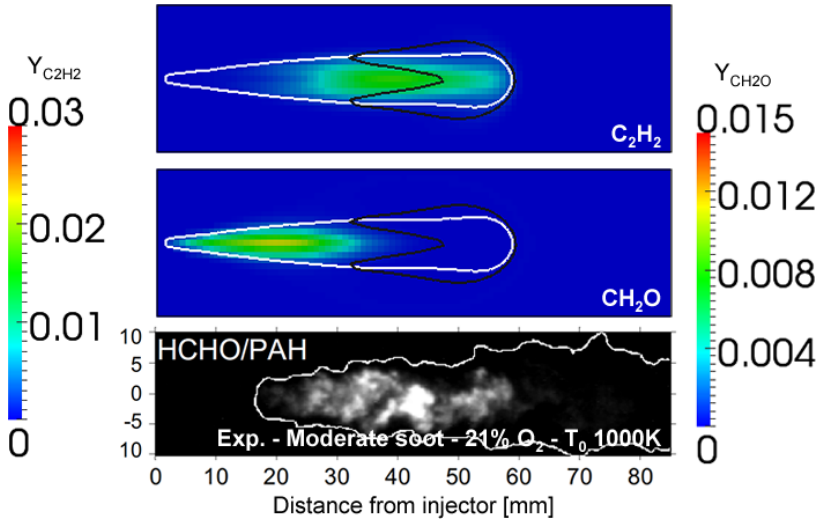

Figure 6.35: $Y_{C_2H_2}$ field and Y_{CH_2O} field at 1.5 ms ASI, comparison between experimental and computed distributions for moderate-soot conditions: the white line represents points at stoichiometric mixture fraction and the black line consists of an iso-contour of 2200 K temperature. PLIF imaging reproduced from [17].

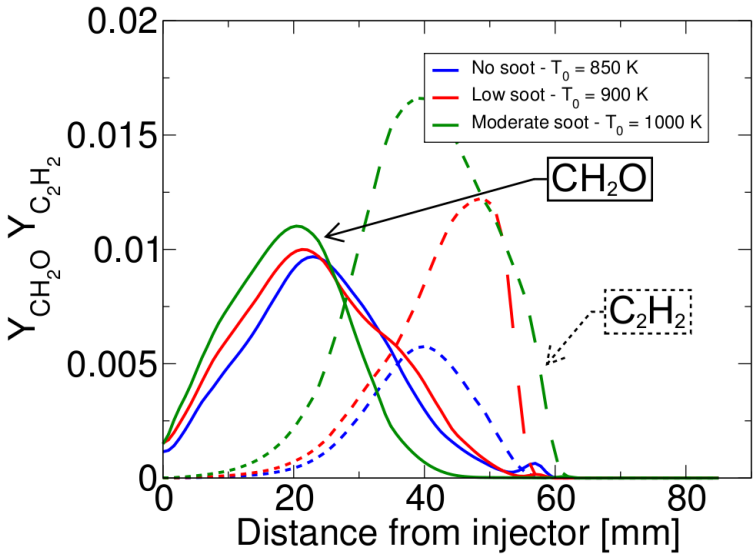

Figure 6.36: comparison among the computed Y_{CH_2O} (straight lines) and $Y_{C_2H_2}$ (dashed lines) distributions along the spray axis for different soot conditions.

in the high-temperature reaction zone and its concentration increases with increasing soot production, due to a higher initial vessel temperature.

6.3.2 Initial vessel density

The influence of the initial gas density is investigated for two different cases, summarized in table (6.4).

O_2 mole fraction	Ambient temp.	Ambient density	Ambient pressure	Injected mass	Lift-off length	Ignition delay
[%]	[K]	[kg/m^3]	[MPa]	[mg]	[mm]	[ms]
15	1000	14.8	4.25	17.8	23.4	0.82
15	1000	30.0	8.70	18.0	11.9	0.49

Table 6.4: cases set-up: influence of the initial vessel density.

The pressure rise and its derivative versus time are depicted in figures (6.37) and (6.38) respectively, while the ignition delay and the lift-off length are shown in figure (6.39).

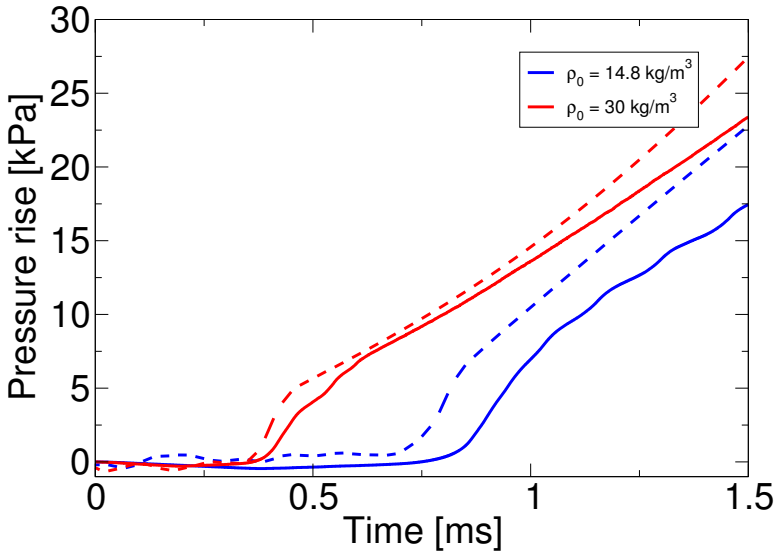

Figure 6.37: comparison between experimental (dashed lines) and computed (straight lines) pressure rise varying the initial vessel density. The domain is subdivided according to the injected mass criterion and flamelet interaction is neglected.

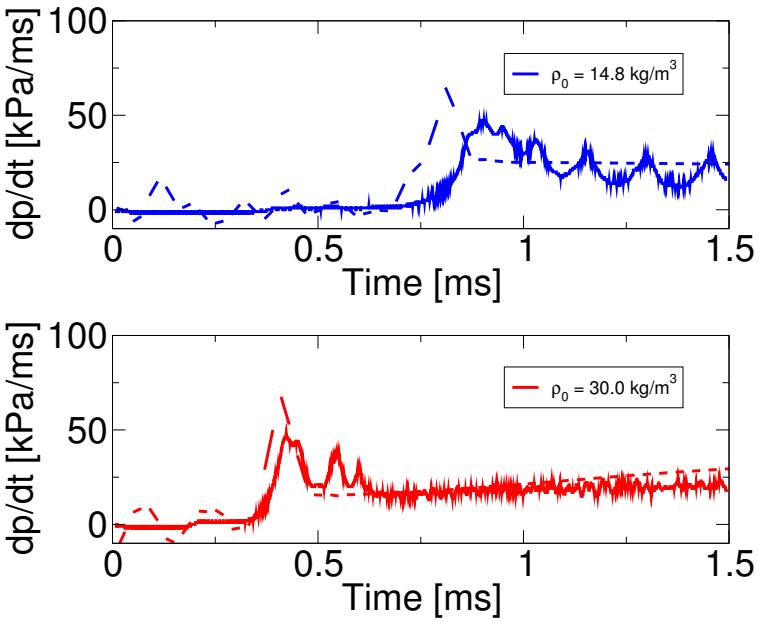

Figure 6.38: comparison between experimental (dashed lines) and computed (straight lines) pressure rise derivative versus time varying the initial vessel density. The domain is subdivided according to the injected mass criterion and flamelet interaction is neglected.

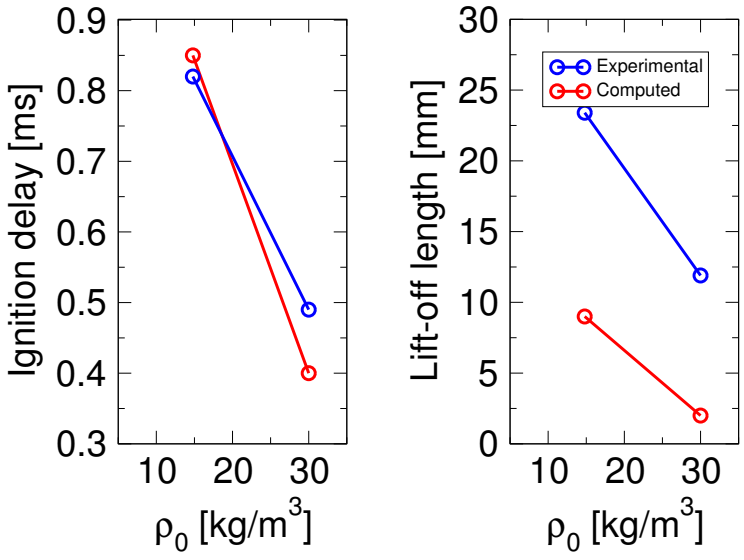

Figure 6.39: comparison between experimental and computed ignition delay and lift-off length varying the initial vessel density. The domain is subdivided according to the injected mass criterion and flamelet interaction is neglected.

The computed pressure rise and its derivative versus time can be considered encouraging: in fact the heat release during autoignition is in good agreement with the measured one for both the cases, while during mixing controlled combustion it is slightly underestimated.

For the computed high density case (depicted in figure (6.37) with red lines) the flame is attached to the nozzle again, as can be carried out from the very limited lift-off length. Along with the disappearing of the typical pressure oscillations due to flamelet ignition and to the underestimated ignition delay, this fact shows that this simulation, which involve multiple flamelets, presents the same drawbacks of using only one flamelet. In fact, due to the high ambient density, the time that a new injected flamelet needs to ignite is severely reduced, making the ignition to take place very close to the injector. This is another confirmation of how the lifted flame is reproduced in such a simulation: the flame is kept away from the nozzle by the new injected flamelets, which are not yet ignited.

As it can be seen in figure (6.39), the model correctly estimates both the decreasing of the lift-off length and the ignition delay with the increasing of the initial vessel density.

6.3.3 Initial oxygen concentation

In this section, the effect of varying the initial oxygen concentration is investigated for four different cases summarized in table (6.5).

The experimental data are provided by [33] in terms of pressure rise, lift-off length and ignition delay, and by Idicheria and Pickett from [16], in terms of equivalence ratio.

O_2 mole fraction [%]	Ambient temp. [K]	Ambient density [kg/m^3]	Ambient pressure [MPa]	Injected mass [mg]	Lift-off length [mm]	Ignition delay [ms]
10	1000	14.8	4.28	18.1	35.1	1.21
12	1000	14.8	4.27	17.8	29.2	1.04
15	1000	14.8	4.25	17.8	23.4	0.82
21	1000	14.8	4.21	17.8	17.0	0.63

Table 6.5: cases set-up: influence of the initial oxygen concentration.

Decreasing the oxygen molar fraction of the mixture allows to study the influence of exhaust-gas recirculation (EGR) on combustion. One of the

aims of EGR in low-temperature combustion engines, is to decrease the local fuel-to-air equivalence ratio[2], in order to reduce the soot formation.

In their work [16], Idicheria and Pickett performed a direct measurement of ϕ during several SNL experiments, showing that increasing EGR does not necessary lead to a reduced fuel-to-air equivalence ratio, especially if the injection duration is longer than the ignition delay. In fact, a higher EGR leads to a longer ignition delay and also to an increasing of the air-to-fuel stoichiometric ratio. Therefore, more ambient mass has to be mixed with fuel to achieve the same ϕ and, consequently, more time is required for mixing. A lower fuel-to-air equivalence ratio can be achieved only if the longer ignition delay, due to an increasing of EGR, is enough to reach the required mixing time.

The computed pressure rise and its derivative versus time are depicted in figures (6.40) and (6.41) respectively, the lift-off length and the ignition delay are shown in figure (6.42), the computed temperature fields are represented in figure (6.43) and the computed fuel-to-air equivalence ratio in figure (6.44).

As it can be seen in figure (6.41), the computed heat release rate during autoignition is overestimated only when the initial oxygen molar fraction is 21%, while it is slightly underestimated in the other three cases. Anyway, the model is able to reproduce the decreasing of the energy release during autoignition with increasing EGR.

During the mixing controlled combustion the computed heat release is always underestimated, leading to a lower and lower computed pressure rise with increasing EGR. Also the local oscillations of pressure happening during flamelet ignition result smoothed with high EGR: this is due to the reduced energy release resulting from the lack of oxidizer.

Figure (6.42) shows the comparison between the computed and measured ignition delay and lift-off length for different EGR conditions. The ignition delay is always slightly overestimated while the lift-off length is severely underestimated, like it happens in the previously discussed simulations. Anyway the model can predict both the trend of the ignition delay and the lift-off length.

For what concerns the ignition delay, the differences between the computed and measured values increase with increasing EGR. This is probably due to the simplified chemistry mechanism, which was validated on a narrow range of ambient conditions.

[2]The fuel-to-air equivalence ratio is defined as

$$\phi = \frac{\alpha_{st}}{\alpha}$$

where α is the air-to-fuel ratio and the 'st' subscript means stoichiometric conditions.

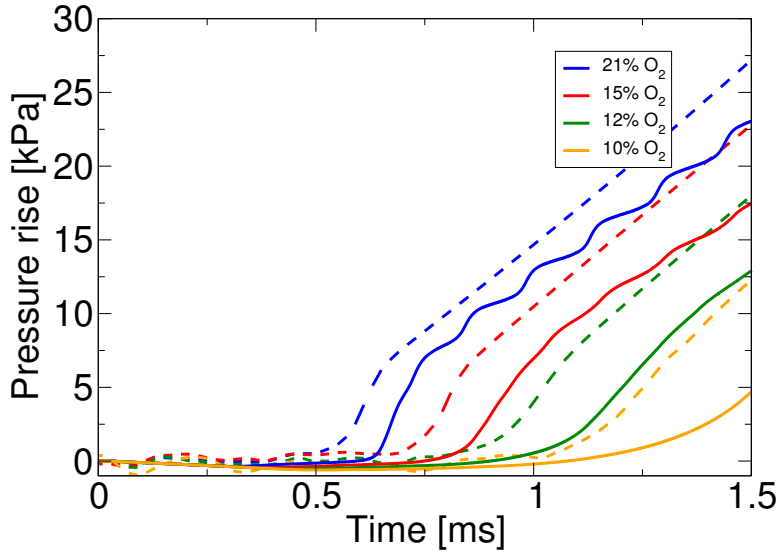

Figure 6.40: comparison between experimental (dashed lines) and computed (straight lines) pressure rise varying the initial oxygen concentration. The domain is subdivided according to the injected mass criterion and flamelet interaction is neglected.

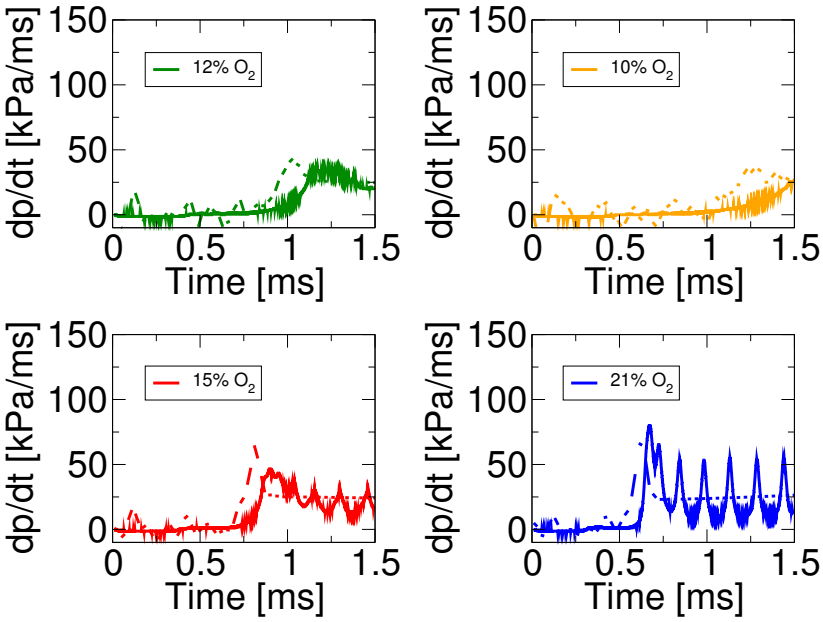

Figure 6.41: comparison between experimental (dashed lines) and computed (straight lines) pressure rise derivative versus time varying the initial oxygen concentration. The domain is subdivided according to the injected mass criterion and flamelet interaction is neglected.

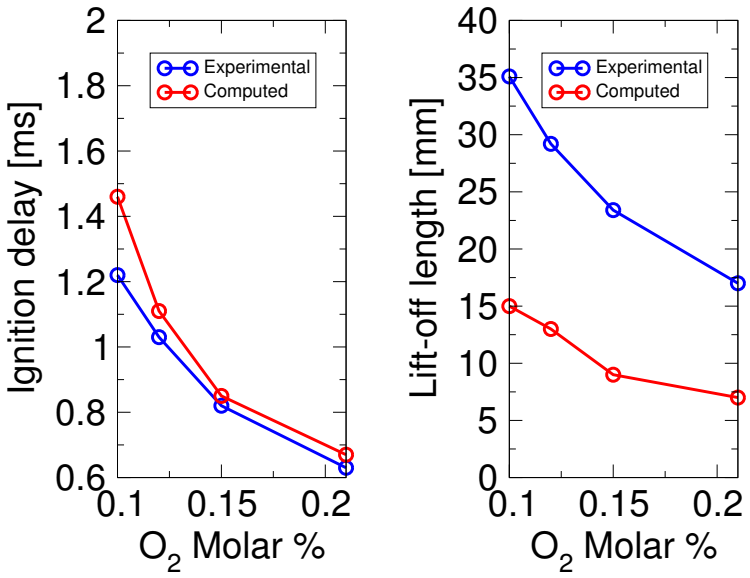

Figure 6.42: comparison between experimental and computed ignition delay and lift-off length varying the initial oxygen concentration. The domain is subdivided according to the injected mass criterion and flamelet interaction is neglected.

The computed lift-off length increases with increasing EGR: flamelets, in fact, need more time to ignite due to the lack of oxygen and, therefore, they can move the flame further downstream away from the injector.

Figure (6.43) compares the computed temperature fields at 1.5 ms ASI with the images coming from chemiluminescence and provided by [33]. The predicted temperature fields seems to be in agreement with the experimental images, especially for what concerns the flame structure variations with increasing EGR. When the initial oxygen molar fraction is 15%, chemiluminescence shows a very hot diffusive flame in the so called 'head vortex', which is not present yet in the computed temperature field, probably due to the already discussed overestimated ignition delay. The model is also capable of reproducing the reduced flame penetration with increasing EGR.

The comparison between the measured fuel-to-air equivalence ratio, coming from [16], and the computed one, is depicted in figure (6.44) at the time of ignition. The computed fuel-to-air equivalence ratio field is underestimated and also the vapour penetration is smaller than the measured one. These features are probably due to the mesh which is coarser than necessary and is not able to capture local vapour fluctuations. In these simulations, three level of mesh refinement were employed, leading the characteristic size of the cells to be at least equal to 0.96 mm. These settings are typical in internal combus-

tion engines simulations since they allow to reduce computational costs and achieve results in workable time. Despite the latter drawbacks, the model reproduces quite well the fuel-to-air equivalence ratio distribution: in fact ϕ is high near the injector tip and decreases with increasing distance along the jet centreline, it is equal to unity (which means stoichiometric mixture) only at the jet periphery and remains relatively unchanged with increasing EGR.

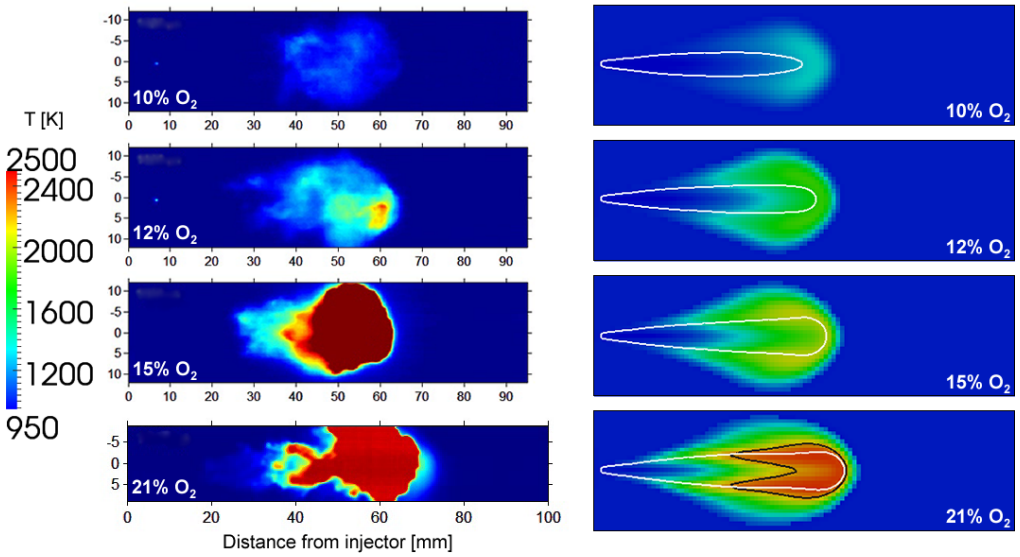

Figure 6.43: comparison between the computed and measured temperature fields at 1.5 ms ASI varying the initial oxygen concentration: the white line represents points at stoichiometric mixture fraction and the black line consists of an iso-contour of 2200 K temperature. The domain is subdivided according to the injected mass criterion and flamelet interaction is neglected. Chemiluminescence imaging (on the left) reproduced from [33].

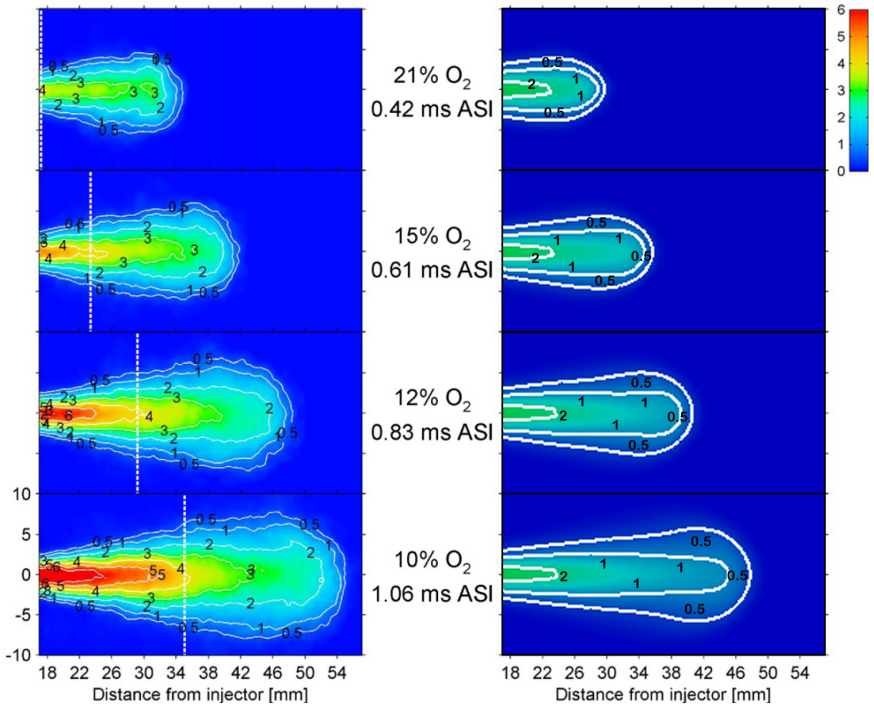

Figure 6.44: comparison between the computed (on the right) and measured (on the left) equivalence ratio at the time of ignition varying the initial oxygen concentration. The domain is subdivided according to the injected mass criterion and flamelet interaction is neglected. Measured equivalence ratio fields reproduced from [16].

Conclusions

This work presented the Representative Interactive Flamelet model, which has been implemented in an open source CFD solver based on OpenFOAM and Lib-ICE, the set of applications and libraries developed by the ICE Group of Politecnico di Milano.

The solver, `RIFdieselFoam`, also includes several features studied by different authors, to improve the original RIF model and account for important physical phenomena, namely the increasing of mixture fraction variance due to liquid spray evaporation (Single Droplet model), the fluctuations of scalar dissipation rate induced by the non-homogeneous turbulent flow field and mixture fraction distribution (Eulerian Particle Flamelet model) and interaction among flamelets (Attack interaction model and Pdf-weighted interaction model).

The RIF model and its variants have been validated over a wide range of operating conditions, by simulating the Diesel combustion at constant volume conditions taking place in the Sandia vessel and comparing the simulation results with the experimental data retrievable in [33]. First of all, a base case reproducing the operating conditions typical of a Diesel engine at full load and maximum speed has been identified. Then, a careful selection of simulations has been performed, in order to discover the influence of the Single Droplet model, the domain subdivision criterion, the interaction among flamelets and the number of flamelets allowed for the computation. After that, the reliability of the different models in reproducing soot precursors, like formaldehyde and acetylene, has been tested and, finally, the influence of ambient conditions on the results in terms of initial vessel temperature, density and oxygen concentration has been investigated.

The results achieved in chapter (6) allow to conclude that:

- the classic RIF model cannot reproduce lifted flames since the single flamelet, which has to represent the entire domain, is one-dimensional and defined by the alone mixture fraction, which only accounts for mixing and does not contain any information about the combustion process. Therefore, when using one flamelet, the flame is always at-

tached to the nozzle since stoichiometric mixture is also present very close to the injector tip;

- the Single Droplet model increases the variance of the mixture fraction both in the rich premixed flame zone and in the diffusive flame zone, leading to a lack of fuel vapour which causes a colder diffusive flame, a lower pressure rise and a longer ignition delay;

- in the RIF model, the flamelet solution is parametrized by the scalar dissipation rate. Different marker particles experience different histories for the scalar dissipation rate, especially when it varies significantly within the combustion chamber, leading to different flamelet solutions. The Eulerian Particle Flamelet model accounts for these variations, involving several flamelets tracked through Lagrangian particles. While creating new flamelets according to the variance of the scalar dissipation rate does not show remarkable differences from the standard RIF simulation, attributing the same amount of injected mass to each flamelet provides encouraging results.

The flame structure predicted subdividing the domain according to the injection time and neglecting flamelet interaction is the only one able to represent flame propagation, showing an acceptable lift-off length. When ambient conditions are particularly favourable to autoignition, namely high ambient density or high ambient temperature, the computed flame moves towards the nozzle. In these cases the flame is attached to the injector tip, showing that in this model the lift-off length is generated by young flamelets that usually need some time to reach the autoignition conditions, happening relatively far from the nozzle.

The most satisfactory results were achieved by using the Eulerian Particle Flamelet model, with a subdivision criterion based on the injected fuel mass. Such approach correctly accounts for effects of spatial variations of the scalar dissipation rate on the combustion process. However, it is still not able to predict a proper lift-off length, which is always underestimated for any tested condition. Nevertheless, the EPFM model properly reproduces distributions of acetylene and formaldehyde within the flame, that are mainly responsible for soot formation in Diesel spray flame. For this reason, it is expected that the EPFM approach would provide satisfactory results when applied to internal combustion engine simulations, not only in terms of cylinder pressure and heat release rate, but also for what concerns pollutant emissions.

Possible future developments of the model can be focused on improving the prediction of the lift-off length, by introducing a progress variable to

properly account for the premixed flame propagation that takes place after ignition.

Bibliography

[1] G. Bader and P. Deuflhard, *A semi-implicit mid-point rule for stiff systems of ordinary differential equations*, Numerische Mathematik **41** (1983), 373–398.

[2] H. Barths, C. Antoni, and N. Peters, *Three-dimensional simulation of pollutant formation in a di diesel engine using multiple interactive flamelets*, SAE Technical Paper 982459 (1998).

[3] H. Barths, C. Hasse, G. Bikas, and N. Peters, *Simulation of combustion in direct injection diesel engines using an eulerian particle flamelet model*, Proceedings of the Combustion Institute **28** (2000), 1161–1168.

[4] H. Barths, C. Hasse, and N. Peters, *Computational fluid dynamics modelling of non-premixed combustion in direct injection diesel engines*, International Journal of Engine Research **1** (2000), 249–267.

[5] F. Contino, H. Jeanmart, T. Lucchini, and G. D'Errico, *Coupling of in-situ adaptive tabulation and dynamic adaptive chemistry: an effective method for solving combustion in engine simulations*, Proceedings of the Combustion Institute **33** (2011), 3057–3064.

[6] C. Crowe, M. Sommerfield, and Y. Tsuji, *Multiphase flows with droplets and particles* (CRC Press, ed.), CRC Press, 1998.

[7] H. J. Curran, P. Gaffuri, W. J. Pitz, and C. K. Westbrook, *A comprehensive modeling study of n-heptane oxidation*, Combustion and Flame **114** (1998), 149–177.

[8] P. J. Davis, *Gamma functions and related functions*, Handbook of mathematical functions (1970), 255–258.

[9] J. E. Dec, *A conceptual model of di diesel combustion based on laser-sheet imaging*, SAE Technical Paper 970873 (1997).

[10] G. D'Errico, D. Ettorre, and T. Lucchini, *Simplified and detailed chemistry modelling of constant-volume diesel combustion experiments*, SAE Technical Paper 2008-01-0954 (2008).

[11] J. H. Ferziger and M. Peric, *Computational methods for fluid dynamics* (Springer, ed.), Springer, 1996.

[12] M. P. Halstead, L.J. Kirsch, and C. P. Quinn, *The autoignition of hydrocarbon fuels at high temperatures and pressures — fitting of a mathematical model*, Combustion and flame **30** (1977), 45–60.

[13] C. Hasse, *A two-dimensional flamelet model for multiple injections in diesel engines*, Ph.D. Thesis, 2004.

[14] M. R. Hestenes and E. Stiefel, *Methods of conjugate gradient for solving linear systems*, Journal of Research of the National Bureau of Standards **49** (1952), 409–436.

[15] K. Y. Huh and A. D. Gosman, *A phenomenological model of diesel spray atomization*, Proceedings of the international conference on multiphase flows, 1991.

[16] A. Idicheria and L. M. Pickett, *Effect of egr on diesel premixed-burn equivalence ratio*, Proceedings of the Combustion Institute **31** (2007), 2931–2938.

[17] C. A. Idicheria and L. M. Pickett, *Formaldehyde visualization near lift-off location in a diesel jet*, SAE Technical Paper 2006-01-3434 (2006).

[18] R. I. Issa, *Solution of the implicitly discretised fluid flow equations by operator-splitting*, Journal of Computational Physics **62** (1986), 40–65.

[19] H. Jasak, *Error analysis and estimation for the finite volume method with applications to fluid flows*, Ph.D. Thesis, 1996.

[20] W. P. Jones and B. E. Launder, *The prediction of laminarization with a 2-equation model of turbulence*, International Journal of Heat and Mass Transfer **15** (1972), 301–314.

[21] W. P. Jones and J. H. Whitelaw, *Calculation methods for turbulent reacting flows: a review*, Combustion and flame **48** (1982), 1–26.

[22] S. Kong, Z. Han, and R. Reitz, *The development and application of a diesel ignition and combustion model for multidimensional engine simulation*, SAE Technical Paper 950278 (1995).

[23] C. Kralj, *Numerical simulation of diesel spray processes*, Ph.D. Thesis, 1995.

[24] H. Lehtiniemi, Y. Zhang, R. Rawat, and F. Mauss, *Efficient 3-d cfd combustion modeling with transient flamelet models*, SAE Technical Paper 2008-01-0957 (2008).

[25] D. Lentini, *Assessment of the stretched laminar flamelet approach for non-premixed turbulent combustion*, Combustion Science and Technology **100** (1994), 95–122.

[26] L. Liang, J. G. Stevens, and J. T. Farrell, *A dynamic adaptive chemistry scheme for reactive flow computations*, Proceedings of the Combustion Institute **32** (2009), 527–534.

[27] F. Liu, H. Guo, G. J. Smallwood, Ö. L. Gülder, and M. D. Matovic, *A robust and accurate algorithm of the β-pdf integration and its application to turbulent methane-air diffusion combustion in a gas turbine combustor simulator*, International Journal of Thermal Sciences **41** (2002), 763–772.

[28] T. Lu and C. K. Law, *Strategies for mechanism reduction for large hydrocarbons: n-heptane*, Combustion and Flame **154** (2008), 153–163.

[29] T. Lu, C. K. Law, C. S. Yoo, and J. H. Chen, *Dynamic stiffness removal for direct numerical simulations*, Combustion and Flame **156** (2009), 1542–1551.

[30] T. Lucchini, *Lib-ice: code structure and capabilities*, Politecnico di Milano.

[31] T. Lucchini, G. D'Errico, and D. Ettorre, *Numerical investigation of the spray-mesh-turbulence interactions for high-pressure, evaporating sprays at engine conditions*, Internatonal Journal of Heat and Fluid Flow **32** (2011), 285–297.

[32] D. Mayer, *A multiple flamelet interaction model applied to multiple injection diesel combustion*, Master's Thesis, 2010.

[33] Engine Combustion Network, *Constant volume diesel combustion*, 2012. Online; accessed 16 October 2012.

[34] *Openfoam programmers guide*, 2.1.0, OpenFOAM Foundation, 2011.

[35] *Openfoam user guide*, 2.1.0, OpenFOAM Foundation, 2011.

[36] S. V. Patankar and D. B. Spalding, *A calculation procedure for heat, mass and momentum transfer in three-dimensional parabolic flows*, International Journal of Heat and Mass Transfer **15** (1972), 1787–1806.

[37] N. Peters, *Laminar diffusion flamelet models in non-premixed turbulent combustion*, Progress in Energy and Combustion Science **10** (1984), 319–339.

[38] H. Pitsch, M. Chen, and N. Peters, *Unsteady flamelet modeling of turbulent hydrogen-air diffusion flames*, Symposium (International) on Combustion **27** (1998), 1057–1064.

[39] T. Poinsot and D. Veynante, *Theoretical and numerical combustion* (Inc. R.T. Edwards, ed.), R.T. Edwards, Inc., 2005.

[40] S. B. Pope, *Computationally efficient implementation of combustion chemistry using in situ adaptive tabulation*, Combustion Theory and Modelling **1** (1997), 41–63.

[41] W. E. Ranz and W. R. Marshall, *Evaporation from drops*, Chemical Engineering Progress **48** (1952), 141–146.

[42] R. D. Reitz, *Modelling atomization process in high-pressure vaporizing sprays*, Atomization and Spray Technology **3** (1987), 309–337.

[43] J. Réveillon and L. Vervisch, *Spray vaporization in non-premixed turbulent combustion modeling: a single droplet model*, Combustion and flame **121** (2000), 75–90.

[44] P. K. Senecal, E. Pomraning, and K. J. Richards, *Multi-dimensional modeling of direct-injection diesel spray liquid length and flame lift-off length using cfd and parallel detailed chemistry*, SAE Technical Paper 2003-01-1043 (2003).

[45] S. Singh, R. D. Reitz, and M. P. B. Musculus, *Comparison of the characteristic time (ctc), representative interactive flamelet (rif), and direct integration with detailed chemistry combustion models against optical diagnostic data for multi-mode combustion in a heavy-duty di diesel engine*, SAE Technical Paper 2006-01-0055 (2006).

[46] S. Vogel, *Coupling of a level-set model for premixed combustion with a diffusion flamelet model*, Ph.D. Thesis, 2008.

[47] Wikipedia, *Openfoam — wikipedia, the free encyclopedia*, 2012. Online; accessed 8 October 2012.